Adsorption of molecular layers on hydrophilic SiOxNy probed by DPI technique

BRUNO JEAN SORIA

How to cite:

SORIA, BRUNO JEAN (2010) Adsorption of molecular layers on hydrophilic SiOxNy probed by DPI technique. Masters thesis, Durham University.

Adsorption of molecular layers on hydrophilic SiO_xN_y probed by DPI technique

A thesis submitted for the degree of
Master of Science
at the University of Durham
Department of Physics

Bruno J Soria

2010

Supervisor: Dr. Graham H. Cross

Abstract

The AnaLight Quantum with a new vapour deposition setup and improved protocol has been used to study the self-organization of 5CB molecules deposited from their vapour phase onto a hydrophilic silicon oxynitride surface. Although slightly less accurate, the results are in good agreement with the previous study in terms of average orientation angle and thickness of the monolayer deposited (56.5° and 1.44 nm respectively). We also studied adsorbed water layers on the hydrophilic surface, and found that our setup allows to desorb only about 10% of the layers since those are strongly held by the hydrophilic surface with an ice-like structure. Therefore the importance of performing more advanced studies on the topic has been raised, as these layers may have an influence on the deposition of liquid crystal molecules. Finally we got some performance data about the AnaLight Quantum whose temperature control appeared not to be fast enough to compensate external thermal perturbations. That raised the importance of thermo-optic effects in such a configuration since they get mixed with adsorption effects within the results. Also an asymmetrical beam expander has been designed in order to improve the optical setup of the instrument.

Acknowledgements

Hereby I like to express my gratitude to everyone who made this work possible. I am really grateful to my supervisor Dr. Graham Cross, as well as to Dr. Marcus Swann, Chief Scientific Officer of the Farfield Group in Crewe, for their guidance and support throughout my project.

I would also like to thank all the members of the PSM group. A big thanks to Duncan Mccallum, Safety Coordinator of the Department of Physics, who always kindly took time to provide me technical assistance. Thanks also to Adam Berlie, PhD student, and Marek Szablewski, Associate Fellow in the Department of Physics, who provided useful advices and tips during this year. Finally, thanks to Laura Wright and Nia Brooks, final year students, for the pleasant working atmosphere I had with them.

Many thanks to One North East which offered me a North East Studentship without which I would not have had the chance to perform this MSc project.

Declaration and Copyright Notice

The material contained within this thesis has not previously been submitted for a degree in this or any other university. The research within this thesis has been conducted by the author unless indicated otherwise.

Table of Contents

List of Figures and Tables

Chapter 1. Introduction

1.1. Context

This MSc project was based in the Photonics, Sensors and Materials research group (PSM) of the Department of Physics at the University of Durham, but was also related to the Farfield Group company whose offices are in Crewe (United-Kingdom) and Pittsburgh (Pennsylvania, USA). The reason of such a partnership comes from about 13 years ago when Dr. Graham Cross co-patented the so-called Dual Polarization Interferometry technique (DPI) [1] which gave birth to Farfield in 1997. The company provided to the research group one of their instrument, the AnaLight Quantum, that is why this project has been possible.

The PSM research group is an interdisciplinary group with research in areas as diverse as molecular chemistry, non-linear optics, liquid crystal displays, telecommunication photonic devices and electrical and optical sensors. Particularly, an area of research uses DPI technique to explore the structure and non-linear optical properties of ultra-thin layers of liquid crystal molecules deposited from their vapour phase.

The Farfield Group developed its first commercial product based on DPI technique in 2001. Since then, the company has grown and now provides a range of quantitative analytical technologies and instruments for biophysics, surface science and nanotechnology communities. The expanded product range and increased sales and marketing capability lead to several distribution agreements: the company has now a worldwide sales and distribution network covering 17 countries. The Farfield Group strength relies on the fact they improve and adapt their instruments according to the emerging and evolving measurement demands of scientific communities.

1.2. Problem statement and aim of the work

The self-organization of liquid crystal molecules vapour deposited on hydrophilic SiO_xN_y surface has been previously investigated with another instrument based on the same technique in the PSM group. Therefore this MSc project was firstly aimed at getting new results with the AnaLight Quantum and comparing them to previous investigations, and secondly it was required to explore the field a bit further.

It has been decided to investigate the effect that could have adsorbed water layers on the deposition of liquid crystals. Even though adsorbed water layers have been studied for decades, they are still of great importance in many fields, from biology and environmental chemistry to engineering applications and development of new materials and technologies [2].

Moreover adsorption on silicon oxynitride surfaces is not well-documented compared to adsorption on normal silica surfaces, whereas this kind of materials are becoming more and more important in the industry (promising candidate for replacing pure silica in micro-electronics [3]). Therefore studying the anchoring effect of liquid crystals as well as adsorbed water layers on this kind of surface appears to be useful.

Apart of that, this MSc project was the occasion for the company to get performance data of the AnaLight Quantum (a prototype which had not been used so much so far), as well as about a new ultra-flat chip prototype. Also, the company is at the moment improving some parts of the optical setup of its range of instrument, and was therefore interested about being helped on that task according to the time available. Finally, a feedback about the vapour deposition setup was also required since the evolution of Farfield's instruments might lead in the future to investigate molecules from vapour samples instead of liquid samples.

Chapter 2. Background and theory

2.1. Dual Polarization Interferometry technique

2.1.1. Basic principles [4, 5, 6, 7]

The Dual Polarization Interferometry (DPI) technique is based on an integrated Young's interferometer (**Figure 2.1**). Coherent light is trapped into two stacked slab waveguides, from which light escapes diffracting into free space to form quasi-Young fringes in the far field. The lower waveguide acts as the reference, and the upper one as the sensor since the evanescent field of its guided mode extends out of the chip. Surface phenomena relevant to the variation of refractive index (RI) or thickness induce changes in the upper mode effective index (i.e. changes in the phase difference between the two waveguides since the lower mode effective index keeps constant), that causes the fringes to move in the far field. **Figure 2.1** shows the so-called AnaChip which comprises 5 dielectric layers (silicon oxynitride, SiO_xN_y) coated onto a silicon substrate. Two channels are etched in the top cladding layer to expose the upper waveguide mode evanescent field to the environment.

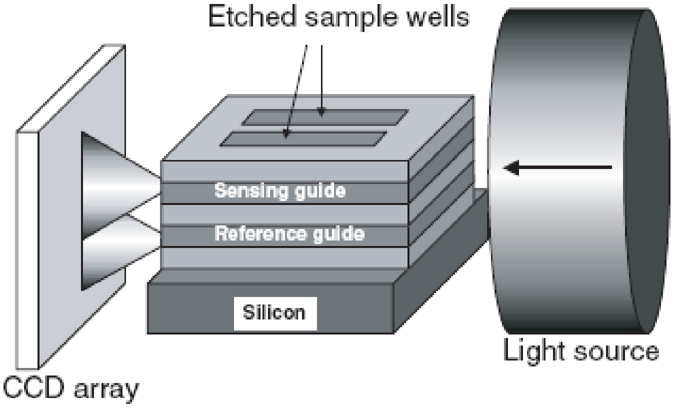

Figure 2.1 – Integrated Young's interferometer on which the DPI technique is based [9, 10].

This basic description of the technique is however incomplete as it would imply an ambiguity on the measurement: an adsorbed layer (adlayer) with given thickness and RI on the waveguide surface could induce the same phase change as a higher RI and lower thickness adlayer for example. To solve this problem, the DPI technique works with two orthogonal polarizations: TE mode, in which the electric field lies in the slab, and TM mode, in which it is mainly perpendicular to the slab. Since TE and TM evanescent field profiles are slightly different, then two different interferograms are available at each instant and two different phase shifts happen when something occurs on the surface. Those phase changes are used as input data to solve Maxwell's equations for the structure with an isotropic adlayer on it in order to get only one pair of RI and thickness values at a given time (**Figure 2.2**).

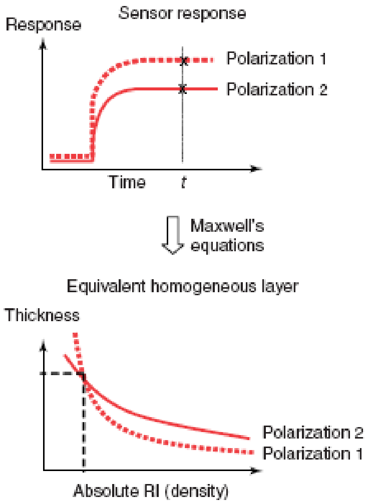

Figure 2.2 – Resolving the 2 measurements from orthogonal polarizations can converge on a unique solution for thickness and RI of an isotropic adlayer [11].

In the case of anisotropic films, 3 parameters (the thickness with two RIs, or with one isotropic RI and a birefringence parameter) must be calculated from only two input data (TE and TM phase changes). The anisotropic modeling developed by Farfield therefore requires complementary data to fix a parameter, either the RI or thickness, in order to get a unique solution, either a unique pair of RI and birefringence values or a unique pair of thickness and birefringence values (**Figure 2.3**) [8].

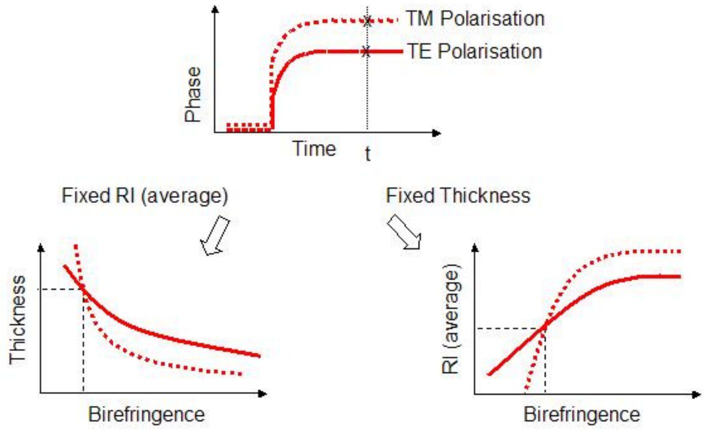

Figure 2.3 – For anisotropic adlayers, it is required to fix one parameter to get the 2 others from the 2 experimental measurements.

So far, the DPI technique has found its fruitful application in the sensing of active biological and other physico-chemical thin films deposited on the guiding layer surface. Those materials are normally captured from water-based flowing buffers. In fact, additional methods based on the same basic concept are used to detect in real time some biological processes such as protein adsorption, protein folding, lipid membrane formation, and so on. Farfield instruments now enable investigation of a large range of biological phenomena at a sub-angstrom resolution in so far as they can be adapted for specific investigations (making specific AnaChips for example).

2.1.2. Optical theory

2.1.2.1. Waveguide coupling and propagation

The DPI technique uses a linearly polarized He-Ne laser which emits a TEM_{00} fundamental mode at 632.8 nm. The shape of the intensity can be simulated as a Gaussian function which is oversized compared to the thickness of the chip layers (the laser waist is about 650 μm [12] whereas layers stack is 9 μm). Therefore light is trapped into the waveguides with a poor coupling efficiency but evenly distributed between upper and lower modes, and the measurement technique is not so sensitive to the vertical movements of the beam.

Figure 2.4 is a schematic of the ideal structure of the chip (without taking into account fabrication tolerances). The ideal optogeometrical parameters are written on the right side. The upper part of the picture shows some fundamental differences between TE and TM modes using ray optics. First of all, TM modes tend to travel faster than TE modes in the structure. This property is illustrated by the following equation:

$$N_{eff} = N_g \cdot \sin \alpha \tag{2.1}$$

where N_{eff}, is the effective index of the mode (which gives information about the effective velocity of a mode propagating over several media of different RI), N_g is the RI of the guiding layer, and α is the mode angle represented on the schematic for each polarization ($\alpha_{TM} < \alpha_{TE}$). Secondly, the black arrows show the directions of oscillation of both the electric and magnetic fields for each polarization. The TE modes are the solutions of Maxwell's equations corresponding to $H_z=E_y=E_x=0$, and the TM modes are the solutions corresponding to $E_z=H_y=H_x=0$ [13].

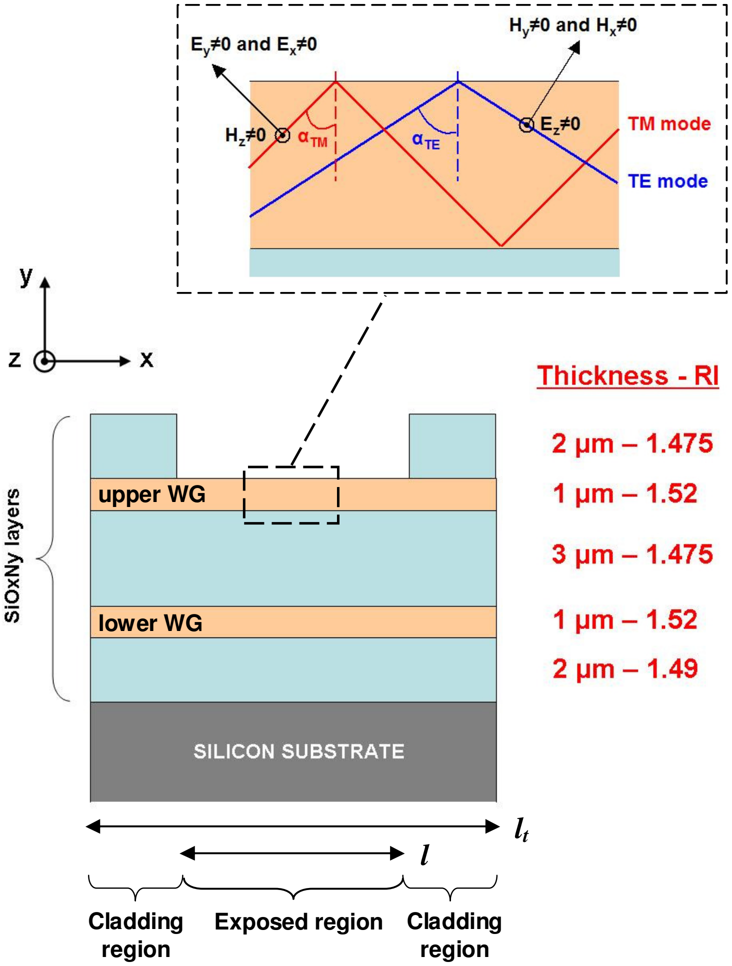

Figure 2.4 – Ideal chip structure with conventions (bottom), and fundamental differences between TE and TM modes (top).

The 1D mode solver Slab (BBV Software BV) has been used to calculate the modes for the ideal chip structure with air above it (using a Transfer Matrix Method and 512 points). Results on **Figure 2.5** show the non-zero electric and magnetic fields for each polarization. We can see that the field components in the propagation direction, H_x for TE mode and E_x for TM mode, can be neglected compared to H_y and E_y respectively, meaning that the TE and TM mode angles are quite close to $\pi/2$. Moreover, the results confirm that the chip structure is designed so that only fundamental modes in the guiding layers are excited for each polarization state, and so that no mode overlap takes place between upper and lower waveguides [13]. Finally, a comparison between TM and TE effective indexes, which are respectively 1.5011269973 and 1.5027269098, shows that the effective index is lower for TM, meaning again that TM modes are faster. It is also worth noting that upper modes travel faster than lower modes: TE modes for instance exhibit a greater lower waveguide effective index 1.5075470202, compared to the upper waveguide effective index 1.5011269973.

TE MODE

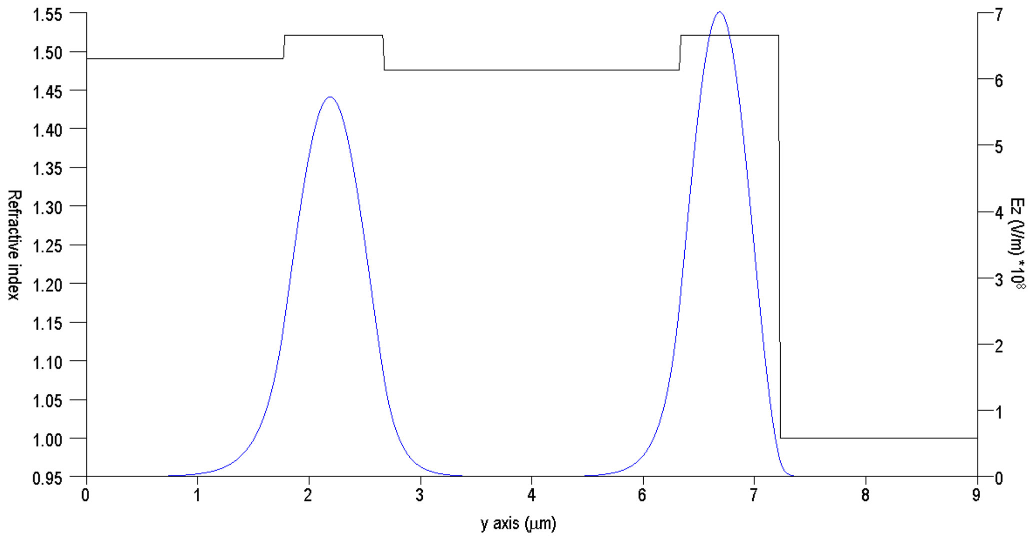

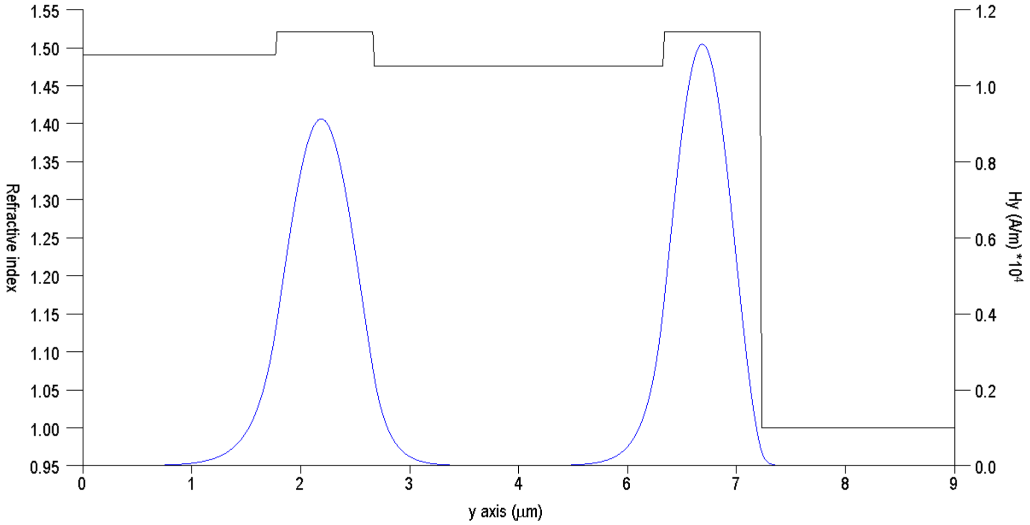
Refractive index
Hy (A/m) *10^4
y axis (μm)
1.55
1.50
1.45
1.40
1.35
1.30
1.25
1.20
1.15
1.10
1.05
1.00
0.95
1.2
1.0
0.8
0.6
0.4
0.2
0.0
0
1
2
3
4
6
7
8
9

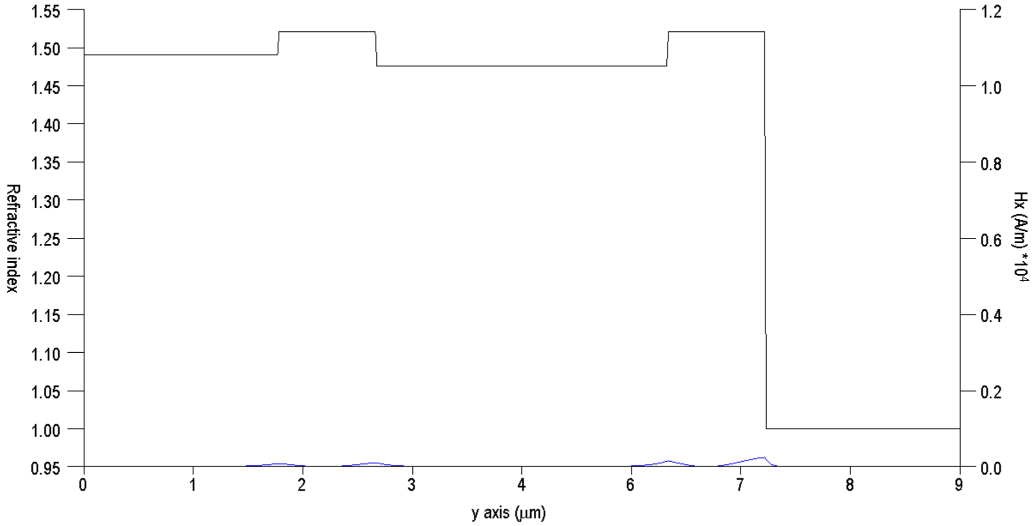
Refractive index
Hx (A/m) *10^4
y axis (μm)
1.55
1.50
1.45
1.40
1.35
1.30
1.25
1.20
1.15
1.10
1.05
1.00
0.95
1.2
1.0
0.8
0.6
0.4
0.2
0.0
0
1
2
3
4
6
7
8
9

TM MODE

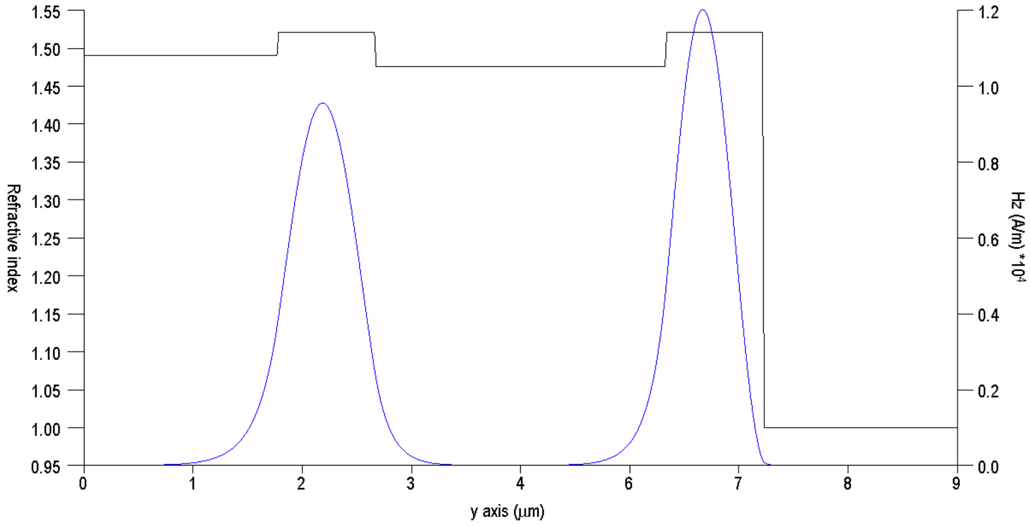
Refractive index
Hz (A/m) *10^4
y axis (μm)
1.55
1.50
1.45
1.40
1.35
1.30
1.25
1.20
1.15
1.10
1.05
1.00
0.95
1.2
1.0
0.8
0.6
0.4
0.2
0.0
0
1
2
3
4
6
7
8
9

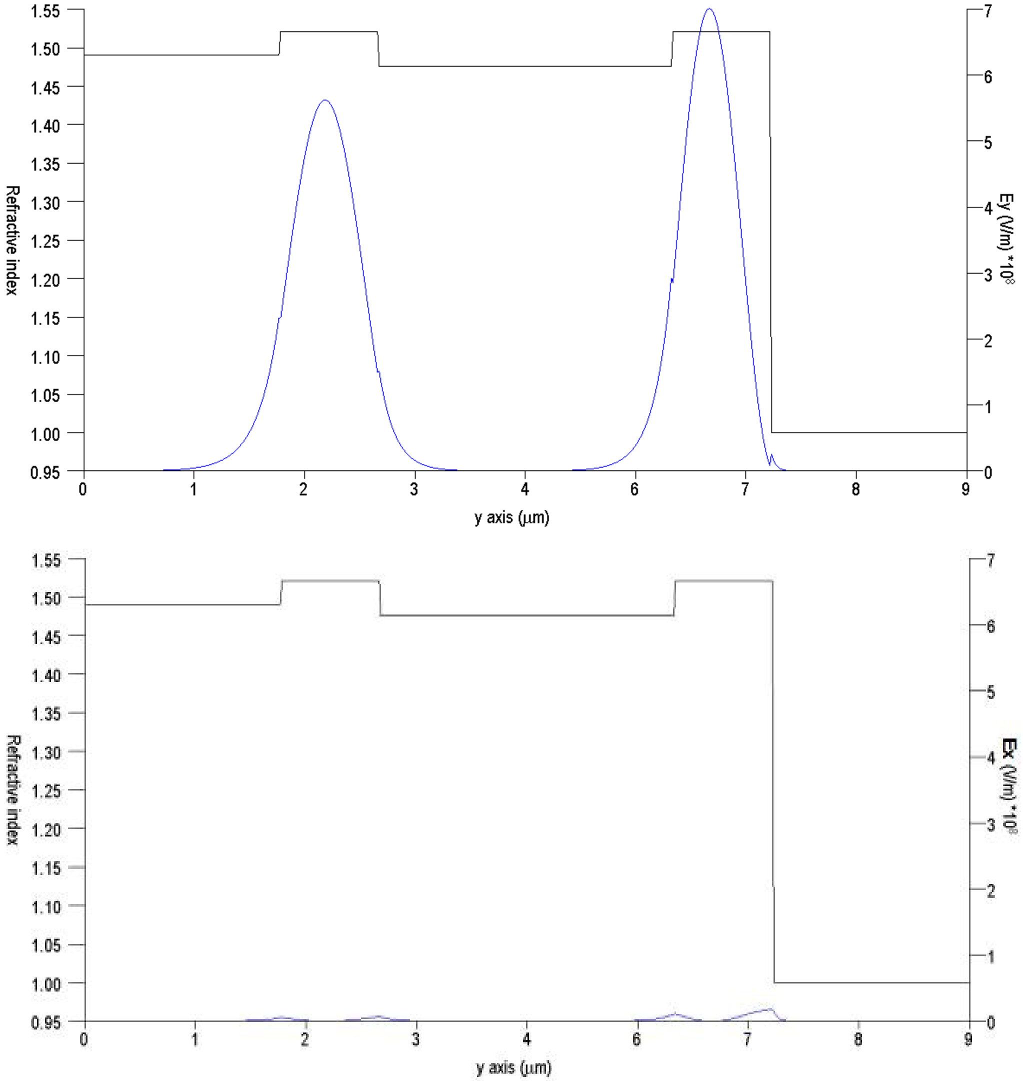

Figure 2.5 – Non-zero fields in each polarization (blue lines) for the chip structure surrounded by air in the exposed region. The black line on each chart shows the RI profile.

Figure 2.6 shows the electric field evanescent profile at the upper waveguide – air interface (the magnetic field doesn't matter too much in non-magnetic layers such as SiO_xN_y layers). Note that only the E_y component of TM electric field has been plotted since the E_x can be neglected. We can see that the evanescent field is able to sense surface phenomena mainly in the first 100 nm above the upper waveguide surface. Moreover TM mode is greater than TE mode electric field out of the upper waveguide, that causes the TM polarization to be usually more sensitive to surface phenomena whereas the TE polarization is more sensitive to the temperature of the chip as it will be observed in the experimental and analysis sections of this document.

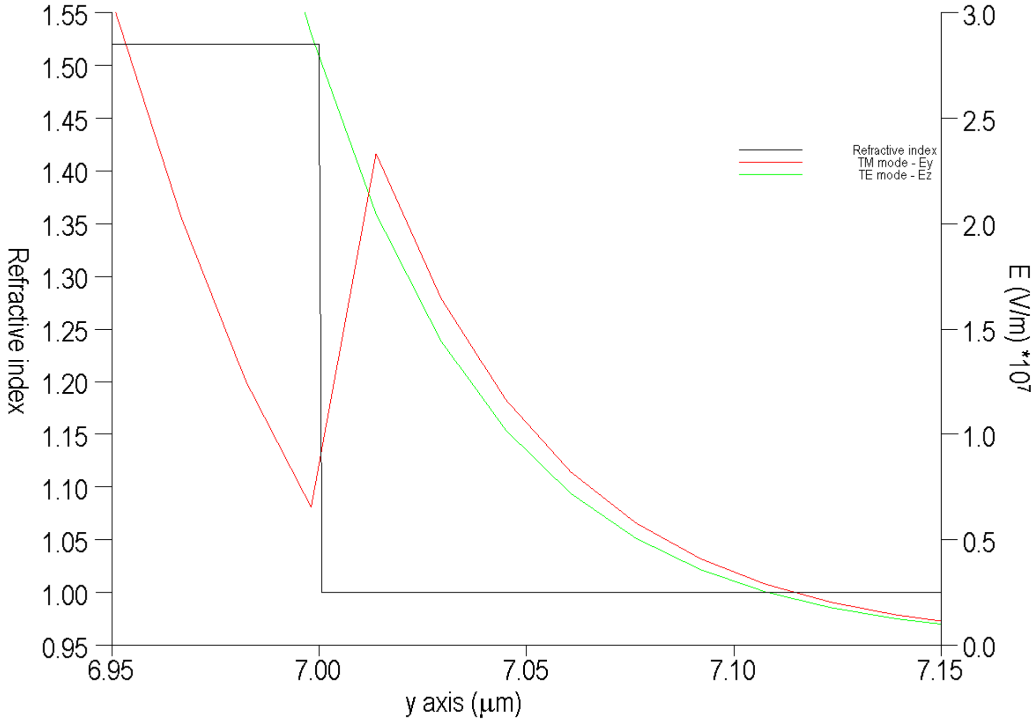

Figure 2.6 – TE and TM evanescent fields at the upper waveguide – air interface.

Note that the real chip structure would be more complicated to solve in so far as the silicon oxynitride layers are not so homogeneous and isotropic. There are also some variations in layers size and some geometrical irregularities due to the fabrication process. Finally, if we consider the whole chip the modes get attenuated because diffraction occurs in the plane of the waveguide ((x,z) plane, where the field is unconfined), and because there is always some material absorption.

2.1.2.2. Far field pattern and detection

At the chip end-face, guided modes start to diffract into free space. Then, they interfere to give in the far field quasi-Young fringes which are recorded on a CCD camera. From that a software gets typical fringe profiles like the one depicted in **Figure 2.7**.

To understand it, let's approximate the upper and lower modes at the end-face of the chip by two separated Gaussian-like beams (the shape of those modes is in reality more complex as shown on **Figure 2.5**). The Fourier transform of this optical signal, which describes quite well the optical signal we get in the far field (Fraunhofer diffraction), is a Gaussian-like envelope (upper envelope) modulated by a cosine function. This is quite similar to the pattern obtained in the case of Young's double slit experiment (a sinc envelope modulated by a cosine function), except that in that experiment the light emerging from the slits has a shape constrained by the rectangular function (instead of Gaussian-like function), that is why a sinc envelope is obtained when the Fourier transform is applied. To go further, let's assume that the upper mode carries less optical power because of scattering losses at the waveguide-adlayer interface. That causes a loss of contrast on the fringe pattern, that is responsible for the lower envelope in the real profile.

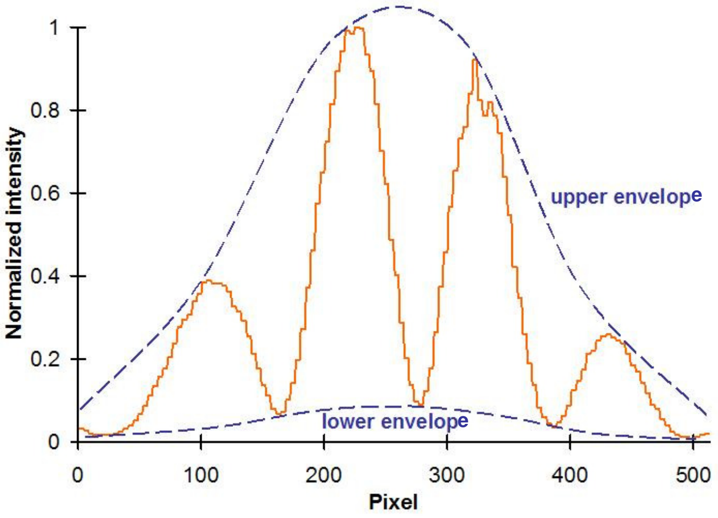

Figure 2.7 – Typical experimental fringe profile given by a software from the image recorded by the CCD camera in the far field (for the chip used in this study).

Basically, the fringe pattern (without considering the diffraction effect for simplicity), can be expressed as following [14]:

$$I = I_u + I_l + 2\sqrt{I_u I_l}\cos\left(k_0 a \frac{y_S}{r} + \phi\right) \tag{2. 2}$$

where $k_0 a \frac{y_S}{r}$ is the spatial phase difference, and ϕ is the initial phase difference at the waveguide end-face which results from the optical path length difference between the upper and lower guiding layers.

With conventions shown in **Figure 2.4** (*x*-axis, propagation direction), the initial phase difference can be expressed:

$$\phi = k_0 N_{eu}\left(l_t - l\right) + k_0 \int_0^l N_e\left(x\right) dx - k_0 N_{el} l_t \qquad (2.3)$$

where N_{eu} is the mode effective index of the upper guiding layer in the cladding region, $N_e\left(x\right)$ is the effective index of upper guiding layer in the exposed region as a function of position, and N_{el} is the lower waveguide effective index. Lengths of the whole chip and of the exposed region are assigned as l_t and l respectively. It is worth noting that an integration is used to obtain the optical path length of the upper waveguide in the exposed region since materials are normally not uniformly deposited on the upper guiding layer.

The above mentioned formulas basically show that a variation of the effective index in the exposed region (due to variation of optogeometrical parameters sensed by the evanescent field) causes straightforwardly a phase change of the fringes. This is the basis of the detection scheme in DPI technique. Then, from the recorded fringe intensities on the CCD camera, a temporal phase measurement algorithm is used to evaluate both the phase and the contrast of fringes (**Appendix A**).

2.1.3. Accuracy of the technique

As it can be noticed on **Figure 2.7**, there is some optical noise on the real fringe pattern we get from the CCD camera. It mainly comes from parasite reflections occurring between optical components within the setup, giving rise to unpolarized scattered light superimposed on the fringe pattern. Given that phases are calculated in reference to the position of the maximum intensity of the fringe pattern, **Figure 2.8** shows how the noise causes an error on the phase. This noise is static in so far as the set up does not move during an experiment.

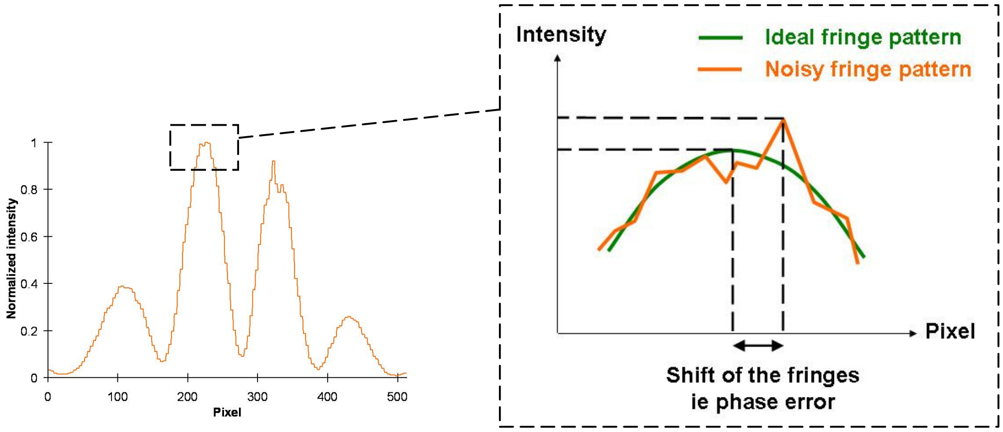

Figure 2.8 – Schematic showing how the optical noise causes an error during the phase calculation.

This static error has important consequences for the studies performed with DPI technique. It has been shown previously that this causes a 2π-periodic oscillation on the phase and contrast as a layer grows on the surface [14]. Tan simulated the phase error *Φerr* (phase difference between a noisy fringe pattern and an ideal one) and the contrast of the noisy fringe pattern *γc* against the phase of the noisy fringe pattern *Φc* (**Figure 2.9**). As the deposition occurs (increase of thickness and/or RI of the adlayer which causes an increase of the effective index and therefore an increase of the phase), fringes become superimposed to themselves each time a 2π change is achieved, it is therefore consistent to get this periodicity on the phase error since the same noise value applies for phase values separated by 2π. Since phase and contrast both depend on the same parameters (see **Appendix A**), the periodicity of the contrast can be understood from the periodicity of the phase. It is likely that the error becomes 0 periodically since the noise doesn't have the same effect on the extrema in comparison to the edges of the fringes (noise has much more impact on extrema).

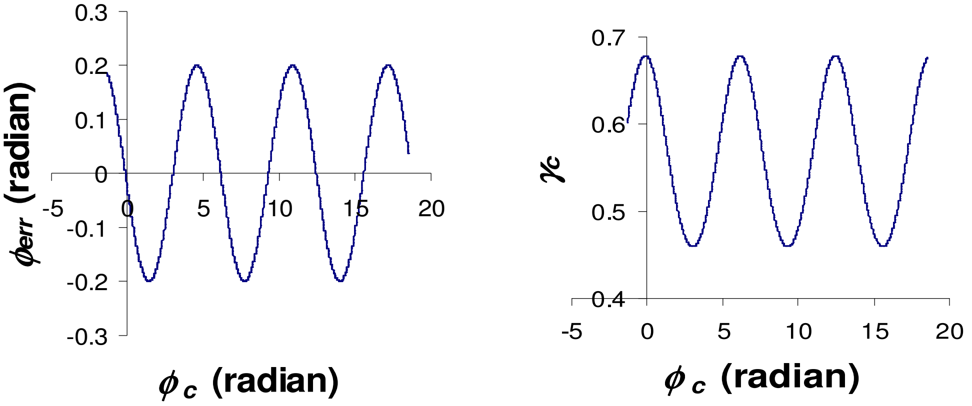

Figure 2.9 – Simulation showing the 2π-periodicity of the phase error (left) and contrast (right) plotted against phase for a noisy fringe pattern [14].

Tan also showed the importance of keeping a contrast as high as possible during an experiment for reliability of results. **Figure 2.10** shows the correlation between phase error and contrast plotted for different levels of scattering at the waveguide surface (the more scattering, the less optical power at the end of the upper waveguide, and the lower the contrast). It can be seen that a higher average contrast improves the accuracy on the phase. The left plot is a calculation using a basic algorithm (to process the data coming from the CCD camera), whereas the right plot corresponds to a more complicated one used in Farfield's software at the time when Tan's study was performed.

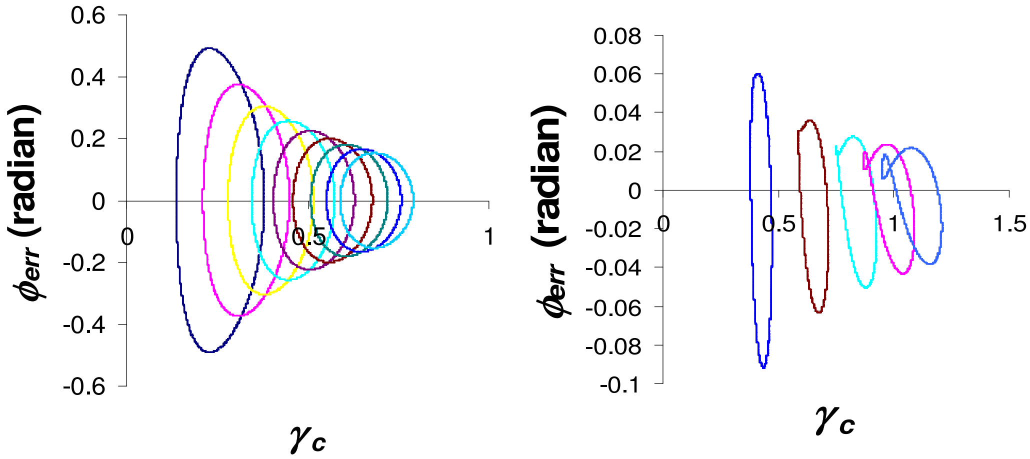

Figure 2.10 – Correlation between phase error and contrast of a noisy fringe pattern for a range of scattering loss coefficients (the higher the surface scattering loss, the lower the average contrast). (left) Correlation for a basic algorithm. (right) Correlation for an improved algorithm [14].

Farfield uses an improved algorithm as well as the so-called linearization procedure to remove the static error from the data as much as possible [15, 16]. This procedure consists of performing a calibration test using a set up which produces a linear phase change in theory (with thickness and RI both well- known for the initial and final states). As the practical calibration result shows an oscillation on this linear phase change due to static error, the software evaluates the error and removes it from experimental data. Note that this linearization procedure must be performed on the same experimental file (in which the experimental data is). That doesn't cause any problem when both use the same setup (original liquid setup used), however the present study uses another setup (vapour deposition setup). That forbids us to take advantage of the linearization procedure. Changing the setup during the experiment would not be sufficient as it would change the optical configuration making the linearization obsolete.

Finally the fabrication tolerances of the chip cause errors not on the phase this time, but on the resolved properties of adlayer (RI and thickness) [13]. This can be minimized by performing a calibration of the chip [17] which consists in determining the real optogeometrical parameters of the upper waveguide. Contrary to the situation in which the optogeometrical parameters of the chip are fixed, and those of the adlayer are unknown, the idea here is to use the setup with well-known optogeometrical parameters of the adlayer in order to find those of the upper waveguide. From the experimental TE and TM phase changes associated to the transition from a defined initial state to another defined final state, the software is able to calculate the real thickness and RI of the upper waveguide. Using all the previously described procedures which increase the accuracy of the technique, it has been reported that subatomic resolution (0.01nm) is possible for resolving the adlayer thicknesses [18].

2.2. Hydrophilic silicon oxynitride surfaces

2.2.1. Surface properties

As previously explained, the AnaChip is made of a stack of silicon oxynitride layers onto a silicon wafer. The proportion of oxygen and nitrogen varies along the silicon oxynitride layers in order to get layers of different RIs, that enables light to be guided within the structure. The RI can be tailored continuously over a wide range from between 1.45 (SiO_2) and 2.0 (Si_3N_4) depending on the *x* and *y* parameters of SiO_xN_y [19, 20]. The theoretical RI of the AnaChip upper waveguide is 1.52, therefore this surface must be pretty similar to silica surfaces (SiO_2) in terms of properties. Considering that hydrophilic silica layers have been extensively studied in the past decades, contrary to silicon oxynitride layers, references about silica layers has been used in this study to understand the properties of the silicon oxynitride surface involved in this work. This approximation has also been made in some papers about work using silicon oxynitride surfaces [8, 21], and [3] considered SiO_xN_y layers as “nitrogen-doped silicon dioxide layers”.

Surfaces can be either hydrophilic (water attracting) or hydrophobic (water repellent). The hydrophilicity of a surface can be measured by the contact angle of a water droplet onto the surface (**Figure 2.11**). Theoretically a purely hydrophilic surface should have a contact angle tending to 0°, meaning that water completely wets the surface. By contrast, a hydrophobic surface should have a contact angle tending to 180°. In fact, these extreme values are impossible to reach because of surface imperfections: roughness, chemical heterogeneity, etc [19]. Therefore, a surface is rather hydrophilic if the contact angle is less than 90°, whereas rather hydrophobic if it is greater than 90°.

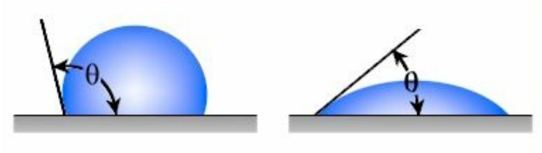

Figure 2.11 – Schematic representing the contact angle: it defines an hydrophobic surface when superior to 90° (left), and an hydrophilic surface when inferior to 90° (right) [24].

The hydrophilicity of a silica surface is due to hydroxyl groups OH bonded to the silicon atoms (that makes silanol groups, Si(OH)). That can be made via a hydroxylation reaction. There are different kinds of silanol groups (“isolated”, “vicinal”, “geminal”, etc) based on the number of hydroxyl groups bonded to each surface silicon atom [22]. They have more or less effect on the adsorption processes, but we will not go into further details about this topic. Past studies show that it is not easy to desorb them (decreasing the hydrophilicity of a surface). Thermal annealing processes (temperature at least 150 °C) must be performed in order for the de-hydroxylation reaction to occur, and complete de-hydroxylation is reported not to be obtained even at temperatures as high as 1100 °C [23].

2.2.2. Physisorbed water layers

Let’s consider a hydrophilic surface surrounded by air. Since the air always carries a certain amount of humidity, some water molecules readily adsorb onto the surface creating hydrogen bonding with hydroxyl groups (silanol groups) [25]. The interaction of a silanol group and a water molecule can be of two types depending on whether H_2O acts as a proton donor or a proton acceptor in the hydrogen bond (donor to the oxygen of the silanol group in the first case, and acceptor to the hydrogen in the second case) [22]. This is a physisorption process, driven by Van der Waals interaction (both water and hydroxyl groups carry electric charges) compared to the so-called chemisorption (creation of covalent bonds between adsorbate and adsorbent). The energy involved being far lower for physisorption processes (compared to chemisorption processes), it is possible to desorb water molecules by increasing the temperature of the surface or decreasing the water vapour pressure.

Adsorption of water may be complicated by complete or partial dissociation of water molecules on the surface, which results in the appearance of the surface hydroxyl groups (discussed quickly in the previous paragraph) [26]. In the case of a freshly cleaved fragment of quartz contacted with water in vacuum the following hydrolysis reaction (hydroxylation reaction) occurs: Si-O-Si + H2O -> 2SiOH (**Figure 2.12 I and II**). When silica is exposed to water for longer intervals, its surface tend to hydrolyze further to form Si(OH)2 and Si(OH)3 [22]. But these are chemical reactions of the surface (chemisorption), and should not be considered as the molecular adsorption of water. **Figure 2.12 II and III** shows water molecules adsorbing on the hydroxylated surface until a fully wetted silica surface is obtained.

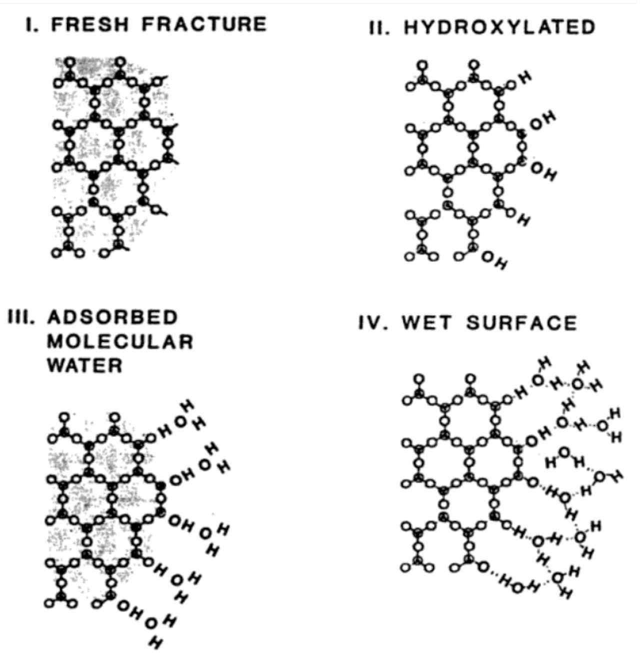

Figure 2.12 – Hydroxylation and adsorption of water on a freshly cleaved fragment of quartz in vacuum [22].

Humidity can be characterized by the relative humidity (RH). It is the ratio between partial water vapour pressure and saturated water vapour pressure (vapour pressure for which a maximum amount of water molecules would be carried by the gas for the system parameters into consideration). Therefore, depending on the RH above a hydrophilic surface, equilibrium builds up between water molecules in the gas phase, and water molecules adsorbed on the surface.

Figure 2.13 depicts a typical adsorption isotherm [27]: as the RH increases, the thickness of the water layer increases, showing a pretty rigid ice-like structure (lower entropy) within the first layers contrary to more flexible structures within the last layers (higher entropy). Additional studies on the topic confirmed these conclusions: the immobilized hydroxyl groups tend to hold the first water layers [28], whereas the additional ordering conferred by subsequent hydration layers quickly gives way due to the disruptive effects of thermal motion [29]. It is worth noting that the attraction coming from the already adsorbed water molecules represents a non negligible part of the driving force governing the adsorption of further water molecules [2, 22]. Moreover those processes strongly depend on the chemical composition and morphology of the surface [2].

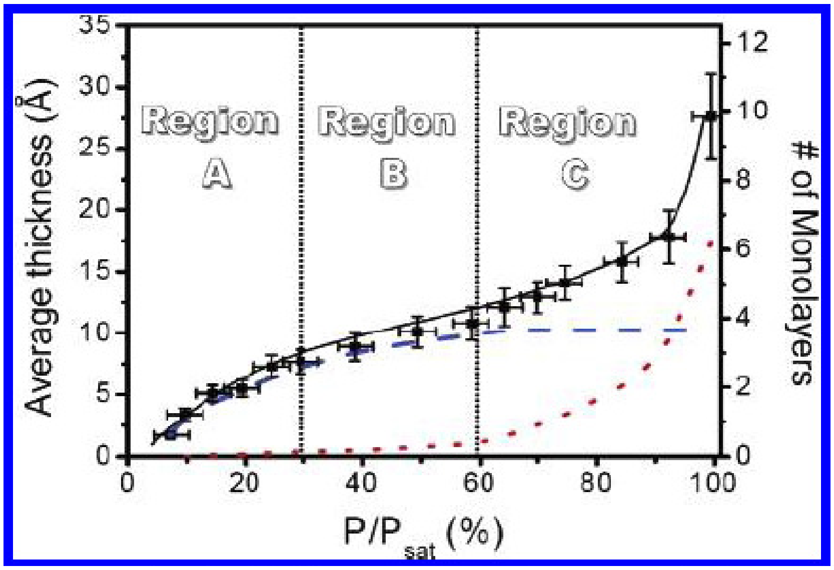

Figure 2.13 – Adsorption isotherm of adsorbed water on a silicon oxide surface. Square symbols are the total thickness of the adsorbed layer. The solid line is drawn to guide the eyes. The blue dashed and red dotted lines are the thickness of the ice-like water and liquid water layers respectively. Regions A, B, and C correspond to ice-like water growth, transitional growth, and liquid water growth respectively [27].

2.3. Self-organization of 5CB monolayers

2.3.1. 5CB anchoring on hydrophilic silica-like surfaces

Liquid crystals are materials which can exist in intermediate phases (mesophases) capable of flowing like a liquid, and having the anisotropy of a solid at the same time. The most common way to get such phases is to control the temperature of the material (for the so-called thermotropic liquid crystals). Basically, when the temperature increases, the melting process from solid state to liquid state consists in a stepwise breakdown of the molecules order: first, molecules gain a rotational freedom, then get the ability to translate, and eventually there is a collapse of the orientation which was maintained so far. Among the variety of liquid crystalline phases (depending on the arrangement of molecules), the most common one is the nematic phase. The minimal energy configuration of such a phase makes rod-like molecules pointing toward a single direction in average (indicated by the director) as shown in **Figure 2.14**.

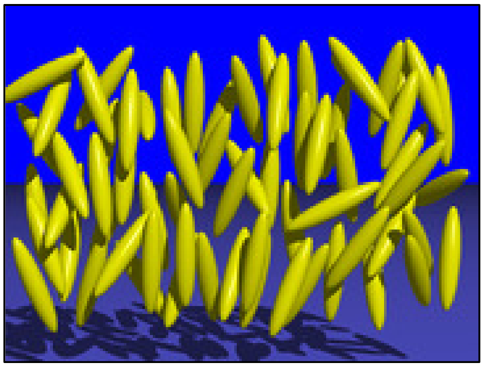

Figure 2.14 – 3D representation of bulk LC molecules in their nematic phase (director oriented upward bound) [33].

Cyanobiphenyls (nCB) are renowned chemical compounds subject to liquid crystalline phases over a quite accessible range of temperature. Their mesogen behaviour (i.e. the ability to exist in liquid crystalline phases) is mainly due to their molecular structure which comprises two parts with different chemical properties. **Figure 2.15** represents a 5CB molecule (rod-like molecule): it is comprised of a linear aliphatic chain (carbon and hydrogen atoms linked to form a flexible chain) associated with a polar group CN (where electrons are permanently asymmetrically distributed) via aromatic compounds (rings of atoms quite rigid compared to the flexible chains). Note that other nCB compounds differ from 5CB only by the number of carbons in the aliphatic chain (5CB has 5 carbons in its chain).

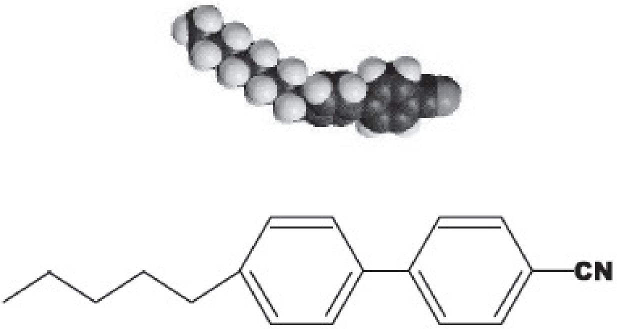

Figure 2.15 – 3D representation and semi-developed formula of 5CB [30].

A common phenomenon occurring for liquid crystals is called the anchoring effect, and is a kind of adsorption since it always occurs when compounds in their liquid crystalline phase are bound with a surface. The phenomenon has been studied for decades. In the case of a nematic phase, we could define surface anchoring by the process which leads to a particular orientation of the director due to interactions with surface [30]. It is worth noting that due to short range surface forces of the substrate the orientational and positional ordering of the molecules within the interfacial layer are generally significantly different from the bulk order [31].

Studies of surface anchoring have been often performed for nematic phases with nCB molecules since they are stable, widely available and well-characterized [31]. It is generally agreed that the anchoring configuration of nCB molecules on untreated clean solid surfaces can be described in terms of a metastable precursor film which is composed of a tilted contact monolayer covered with an interdigitated bilayer (**Figure 2.16**) [31]. Due to the large dipole moment of nCB molecules [31], the polar heads (CN group in orange) tend to attract each other, and are attracted by the hydrophilic surface. This typical anchoring configuration is therefore the result of a competition between the anisotropic polar interaction and the alkyl chain aligning strength. The structure of that monolayer has been studied by Tan using DPI technique [32].

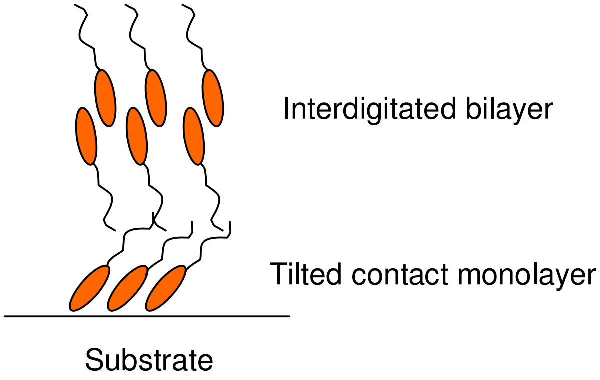

Figure 2.16 – Typical anchoring configuration of nCB on bare silica-like surfaces [14].

2.3.2. Monolayer modeling

The first step is to describe the monolayer in terms of parameters measurable with DPI technique. It must be assumed that the bulk RI values of the material can be applied to ultra-thin surface bound layers [32]. The dielectric tensor of the monolayer in an intrinsic frame (frame of the director) can therefore be expressed as following:

$$\begin{pmatrix} {n_o}^2 & & \\ & {n_o}^2 & \\ & & {n_e}^2 \end{pmatrix} \tag{2.4}$$

where n_o is the ordinary RI, and n_e, the extraordinary RI of bulk molecules. This corresponds to a uniaxial system case, where only one axis of the rod-like molecules exhibits an extraordinary RI (**Figure 2.17 a**).

Since DPI technique enables sensing of two RIs in the chip frame (with TE and TM modes), the intrinsic dielectric tensor must be expressed into the chip frame *(x,y,z)*. **Figure 2.17 b** gives a link between the intrinsic frame and the chip frame according to the average polar angle θ and average azimuthal angle φ of molecules in their nematic phase. That enables to find a relationship between intrinsic RIs and chip frame RIs:

$$\begin{aligned}
{n_x}^2 &= \frac{1}{2}\left[2{n_o}^2 + \left({n_e}^2 - {n_o}^2\right)\sin^2\theta\right] - \frac{1}{2}\left({n_e}^2 - {n_o}^2\right)\sin^2\theta\cos 2\varphi \\
{n_y}^2 &= {n_e}^2 - \left({n_e}^2 - {n_o}^2\right)\sin^2\theta \\
{n_z}^2 &= \frac{1}{2}\left[2{n_o}^2 + \left({n_e}^2 - {n_o}^2\right)\sin^2\theta\right] + \frac{1}{2}\left({n_e}^2 - {n_o}^2\right)\sin^2\theta\cos 2\varphi
\end{aligned} \tag{2.5}$$

where n_x, n_y, et n_z are the nematic phase RIs expressed in the chip frame.

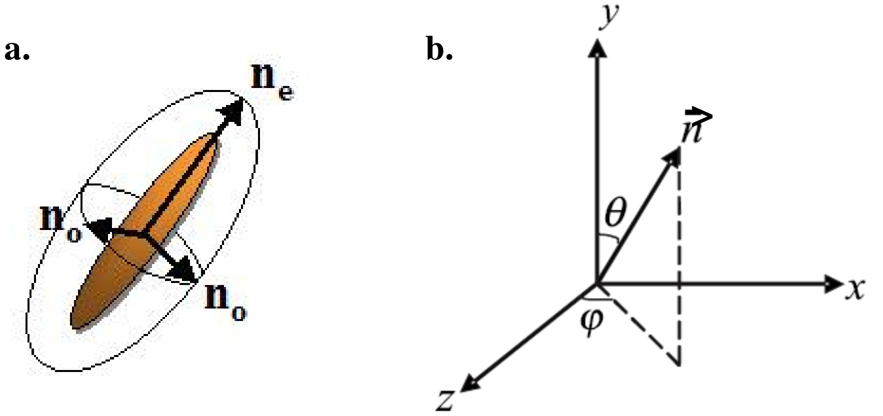

Figure 2.17 – (a) Intrinsic index ellipsoid of a liquid crystal molecule pointing toward the director of the nematic phase. (b) Description of the director in the chip frame.

Assuming that the upper waveguide is isotropic in layout *(x,z)* due to its amorphous bulk structure [32] (note that this assumption has also been noticed in [22]), those equations can be simplified averaging them on the azimuthal angle ($\langle \cos 2\varphi \rangle = 0$):

$$\langle n_z^2 \rangle = \langle n_x^2 \rangle = \frac{1}{2}\left[2n_o^2 + \left(n_e^2 - n_o^2\right)\sin^2\theta\right]$$
$$\langle n_y^2 \rangle = n_e^2 - \left(n_e^2 - n_o^2\right)\sin^2\theta \tag{2.6}$$

Remembering from **Figure 2.4** that the electric field of TE mode is along the z-axis, we have $n_{TE} = n_z$. Similarly, the electric field of TM mode being mainly along the y-axis (since mode angles are close to $\pi/2$ as explained in **Section 2.1.2.1**), we have $n_{TM} = n_y$. This is confirmed by the expression of n_{TM} found in [8] and adapted to a more general case:

$$n_{TM} = \sqrt{n_y^2 \cdot \sin^2 \alpha_{TM} + n_{x,z}^2 \cdot \cos^2 \alpha_{TM}} \tag{2.7}$$

where α_{TM} is the TM mode angle.

Therefore from Maxwell's equations applied to this structure (chip with an adlayer on it) as well as from interference and diffraction equations, we can see that it is possible to link the properties of the monolayer (polar angle θ, and thickness) with the phase changes obtained experimentally.

2.3.3. Previous main results [32]

From the theory described in the previous sections Tan implemented a numerical method (briefly described in **Appendix B**) to get the ratio of the experimental phase changes ($\Delta\Phi_E/\Delta\Phi_M$) plotted against the polar angle θ. He showed that the ratio is almost a monotonic function of the polar angle as shown on **Figure 2.18**. This allows the user to investigate the self-organization of vapour deposited LC molecules quite easily since the experimental phase changes at a given time lead to a ratio value, which is straightforwardly linked to a polar angle value. Additional methods allow the user to determine the evolution of the thickness of the layer depositing, but that will be described in **Section 3.4.**

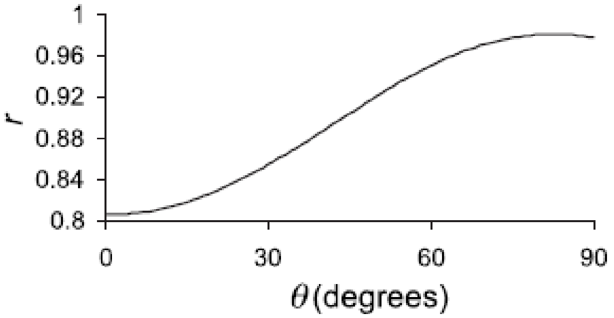

Figure 2.18 – Result from Tan's simulations showing that the phase change ratio r is almost a monotonic function of the average polar angle θ of the molecules in the monolayer [32].

Figure 2.19 shows a typical result of vapour deposited 5CB molecules onto a hydrophilic silicon oxynitride layer: the phase change ratio is plotted against the TE phase change which quantifies the amount of material deposited on the surface. The experimental evolution of the ratio and the simulation results have been used to build a qualitative scenario depicted on **Figure 2.20**. In region A the numerical model is supposed not to be applicable yet as the layer is diluted (RI can only be defined for dense layers), meaning that we can't use the correspondence between ratio and angle at this stage. However molecules are supposed to find surface anchoring sites at random and adopt a range of azimuthal and polar angles determined by the molecular scale surface roughness (molecules lying at some large average polar angle mainly). In region B, the ratio globally decreases meaning that θ decreases as well: molecules progressively displace resident molecules to access the remaining surface sites as the layer densifies.

Finally region C shows a constant ratio which is thought to mean that the monolayer has been achieved as it cannot densify more. At that point, the monolayer is found to be anchored with an average polar angle of 56±1°, with a thickness of 16.6±0.5 Å.

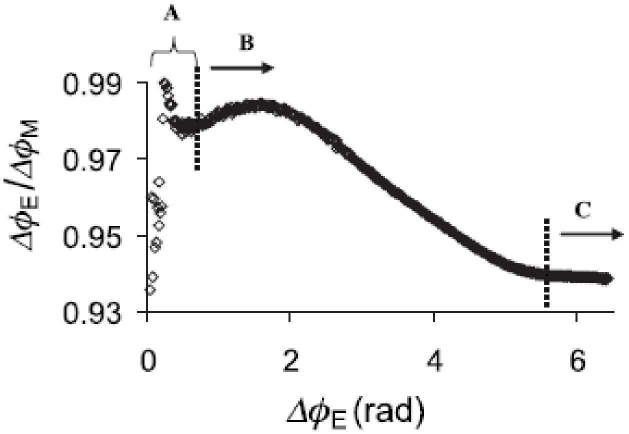

Figure 2.19 – Evolution of the phase change ratio as the amount of deposited material increases (i.e. increase of the phase change) [32].

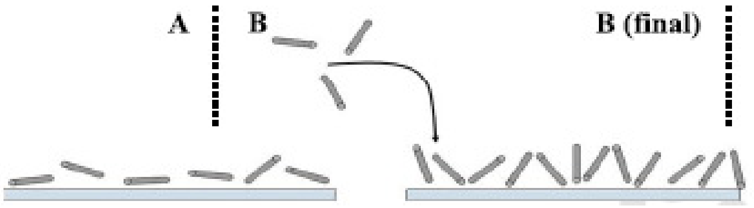

Figure 2.20 – Schematic diagram of molecular re-orientation driven by strong surface anchoring during layer densification (self-organization) [32].

It appears that this work provides a powerful way to extract data from anisotropic thin films provided optogeometrical data is known in advance (ordinary and extraordinary RIs of the 5CB monolayer, assumed to be those of the bulk, and dimensions of 5CB molecules).

Chapter 3. Methods and setup

3.1. Optical setup and procedures

The AnaLight Quantum used in this study is a low-cost prototype of AnaLight range of instruments [34]. In that way, performing a study with this instrument was useful for Farfield to get performance data, as well as to think about possible improvements to make on the instrument.

Some procedures need to be performed on the optical setup of the instrument in order to maximize the reliability of measurements. Some basic procedures will be explained in the following sections, knowing that more details can be found in the service manual of another AnaLight instrument [35].

Those procedures don't have to be performed before each experiment, however the optical setup must be checked before the first use or each time something is changed inside the instrument.

3.1.1. Getting fringes

An important part of the optical setup is the so-called Powell lens. Its role is to expand the laser beam in the horizontal direction (generating a laser line). Indeed, the beam waist is about 650 µm whereas the channels to enlighten are 3 mm wide in total (two 1 mm etched channels, separated by a 1 mm reference channel). With no chip in place, the image on the camera should therefore look like a "letterbox" since the Powell lens spreads the circular beam profile only in one direction.

First, the Powell lens mounted on the laser must be adjusted. It can be either rotated in order to make the letterbox image horizontal, or translated in order to equilibrate the optical power on the letterbox image and get a uniform symmetric image (**Figure 3.1 a**). This is achieved adjusting laterally the Powell lens with a 0.035 inch Allen key while pointing the laser toward a wall (**Figure 3.1 b**). The letterbox image should look like that depicted in **Figure 3.2 a** (1024*1024 pixels image coming from CCD camera).

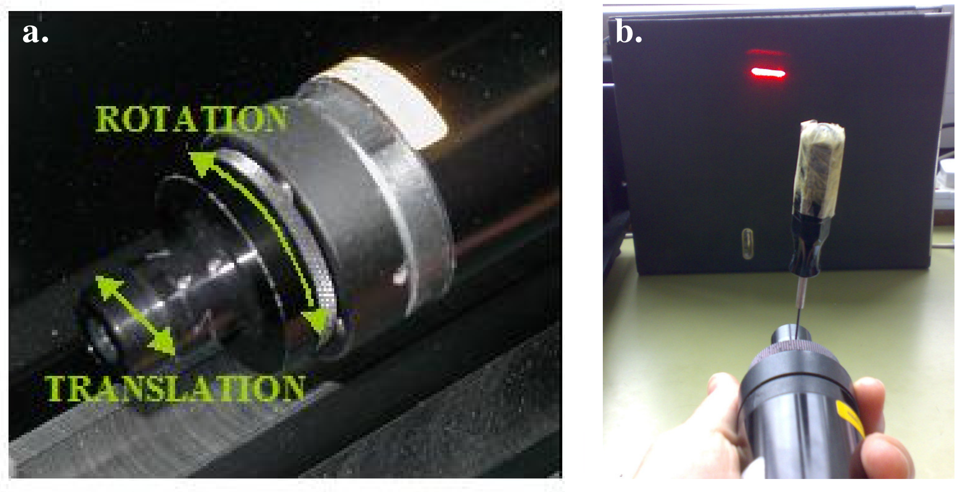

Figure 3.1 – (a) Degrees of freedom for Powell lens adjustment. (b) Optical power repartition on the laser line checked by pointing the laser toward a wall.

Finally, using the laser degrees of freedom the letterbox image must be placed so that the centre of the spread beam illuminates the entrance of the waveguides over the whole width of the chip in order to see the 5 sets of fringes of a chip in place (**Figure 3.2 b**). Note that it has been found that clamping the laser by the metal circle on its end gives rise to a better thermal stability during experiments.

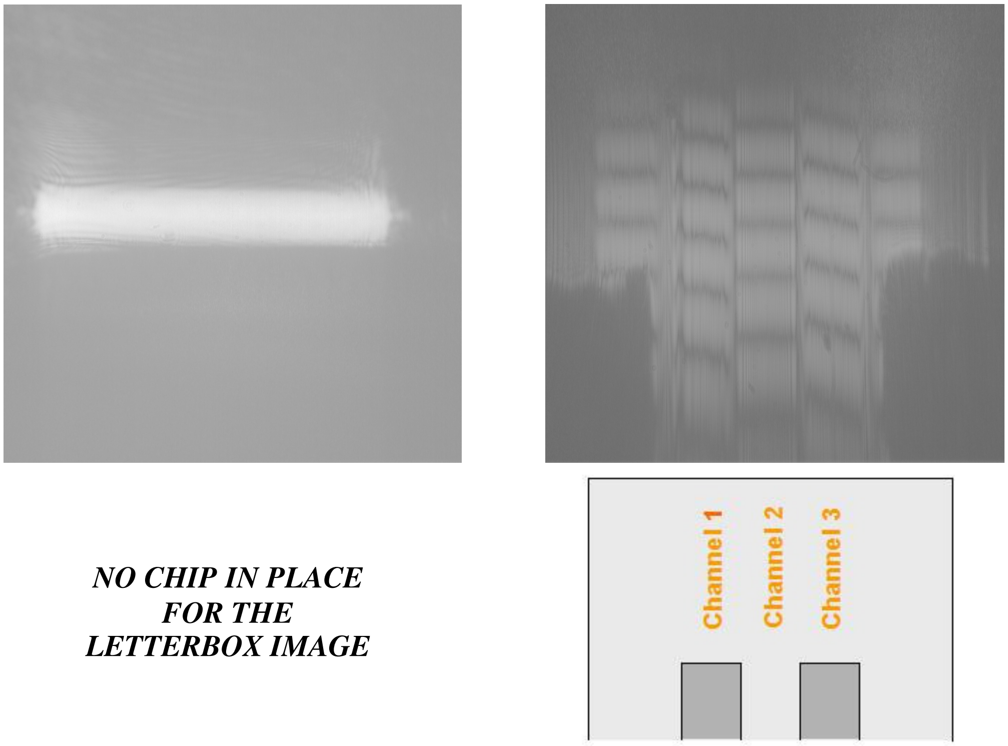

Figure 3.2 – (left) Letterbox image with no chip in place. (right) 5 sets of fringes from the chip in place corresponding to the 3 cladding regions intercalated with the 2 exposed regions.

It has been noticed that it is almost impossible to equilibrate the power on the letterbox image since it would require that the centre of the laser beam hits the Powell lens perfectly on its edge. Moreover it seems that the divergence of the expanded beam (about 4°) can cause reflections within the chip and defects on the fringe image. For those reasons a simple asymmetrical beam expander has been designed for the company: it uses cylindrical lenses to expand the beam in only one direction, and to get a collimated beam at the chip end-face (**Appendix C**).

3.1.2. Polarization adjustments

Due to the importance of polarization in DPI technique, this kind of adjustments must be performed with a lot of care. The optical component responsible for switching polarization between TE and TM is a Ferroelectric Liquid Crystal polarization rotator (FLC). It acts as a half-wave plate switchable only by applying a voltage. Therefore, a linear input polarization (pointing toward a direction fitting with FLC optical axis) can be controlled, being either rotated by 90° or kept in the same direction. Polarizations are switched alternately at 500 Hz, meaning that the software gets a data point every 2 ms (the FLC is synchronized with the camera). However, note that the data acquisition step during experiments can't be set below 100 ms as the software must average many data points in order to increase the reliability of measurement.

Since the FLC is clamped and cannot be adjusted (**Figure 3.3**), the laser must be rotated around its axis in order to be adjusted with regards to the FLC optical axis. The idea is to check the effect of rotating the laser following the evolution of the phase difference between TE and TM fringe patterns with the software. For that purpose the best way is to use a chip where TE and TM fringe patterns are separated as much as possible on the reference channel (channel 2 on **Figure 3.2**): a π-shift is the optimal case. Indeed, using a chip for which TE and TM fringes are almost superimposed (due to the chip structure, the cleaning protocol, etc) would hide the effect of changing the polarization orientation.

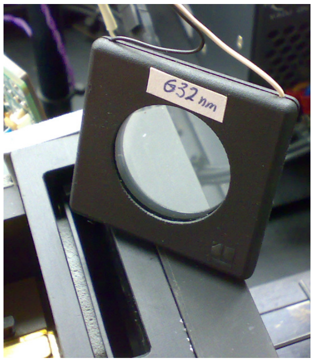

Figure 3.3 – FLC polarization rotator (Displaytech LV2525) removed from its holder.

Figure 3.4 describes 2 extreme cases when the laser is well-rotated (image on the left) and when it is not (image on the right). Those schematics show ellipses which describe the evolution of the polarization direction after passing through the FLC (the polarization purity of the laser beam is initially supposed to be > 500:1 [12], but it has been noticed that the FLC degrades this polarization purity).

In the first case (good laser orientation), the state OFF ellipse is 45° oriented from the FLC optical axis, that makes the ellipse to be rotated by 90° when state is ON. Then, the TE and TM modes coupled into the chip (shown by red arrows) are different for each switching state. In that case we can see on the software that TE and TM fringe patterns are not superimposed. By contrast in the other case (wrong laser orientation), the state OFF ellipse points toward the FLC optical axis, that implies no polarization rotation occur when switching from state OFF to state ON. Therefore, the TE and TM modes coupled into the chip are similar for each state, giving rise to superimposed TE and TM fringe patterns on the software. Note that the better the polarization purity, the less TE-TM mixing on the fringe image of each state.

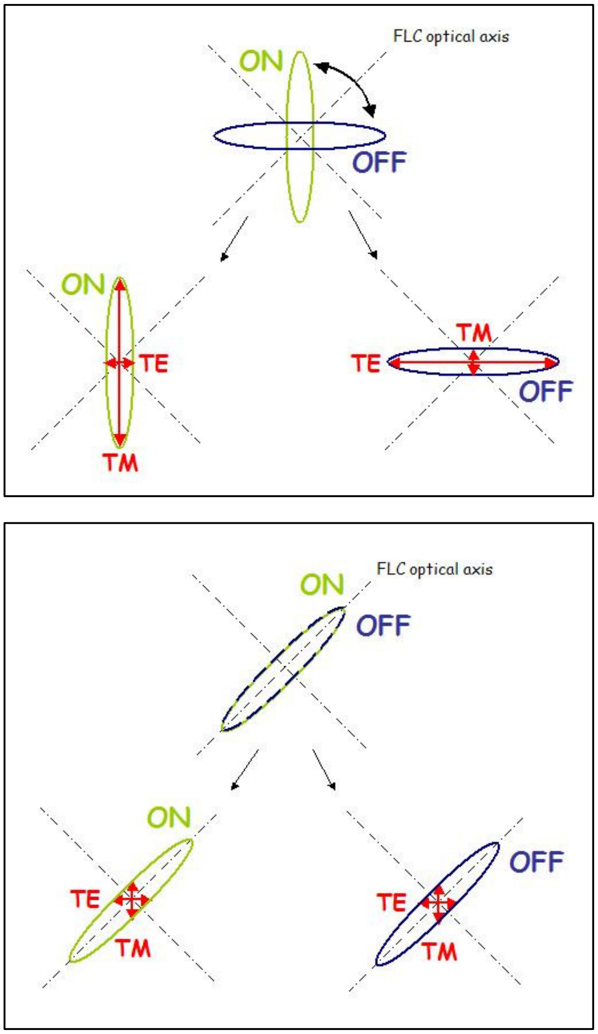

Figure 3.4 – Schematics representing the modes coupled into the chip (red arrows) according to the orientation of the laser with regards to the FLC axis: on the upper picture the laser is well-oriented, whereas it is not on the lower picture.

In order to find the right orientation of the laser, it was required to rotate it until TE and TM fringe patterns were superimposed on the software (worst orientation). Then, we just had to rotate back the laser by 45° in order to get the best orientation. Note that the good orientation of the laser can be confirmed by performing a test whose protocol is described in the manual [35].

3.2. The AnaChip

3.2.1. Description

Some basic aspects of the AnaChip have been already described in **Section 2.1**. The AnaChip is the key component of DPI technique as its quality and design have a strong impact on the quality of measurement. The Farfield Group often improves the AnaChip, several parameters changed during the last decade: dimensions of the wafer, number of etched channels (from 1 to 2), quality of end-faces (faces into which light is coupled at the entrance and from which light escapes at the exit), optogeometrical parameters of the silicon oxynitride layers, and surface treatments (according to the application).

A lot of care must be taken to choose a chip. Its inner structure which depends on the fabrication process must be as close to the ideal structure (see **Figure 2.4**) as possible. The most important are the end-faces which must be completely planar and orthogonal to the chip surface to ensure that a set of fringes observed on the CCD camera (channel 1 - TE polarization for instance) is not the result of the mixing of the channel 1 - TE polarization optical signal with an unexpected contribution of channel 2 - TM polarization optical signal for instance. The contrast also depends on the quality of end-faces, and we already mentioned that a higher contrast is better as it minimizes the static error. Therefore, the AnaChip must be always handled very carefully in order not to damage its end-faces.

At the moment, the chips used by the company are produced in INEX laboratories (Newcastle, UK). We don’t have much data about the fabrication process, except that a Plasma Enhanced Chemical Vapour Deposition (PECVD) method is used to deposit the silicon oxynitride layers onto a silicon wafer. It has been noticed that although this kind of chips exhibits high-quality end-faces (because of the cleaving process), their channel 2 fringe contrast is most of the time less good (about 0.5-0.6) than that of the chips which were made at the Tyndall National Institute (Cork, Ireland) before (whose contrast used to be about 0.6-0.7, but with less well-cleaved end-faces).

In this study we used an “unmodified” (with no surface treatment on it [36]) INEX chip FB80, with the unique property that it has been irradiated with Ar Cluster ions in the Quantum Science and Engineering Center (Kyoto University, Japan) in order to make its surface flatter. This chip which is shown on **Figure 3.5** in its carrier is therefore a prototype exhibiting a roughness accuracy (RA) <1 nm while non-irradiated chips have a RA of about 6-8 nm. Apparently the upper waveguide was initially made thicker than normal (about 1.1 µm) in order to get a thickness close to the usual ideal value (1 µm) after irradiation. In practice, we clearly observed much better channel 1 and 3 contrasts (channels surrounded by air) with this ultra-flat chip compared to usual INEX chips. This study was therefore the first occasion to use this new prototype.

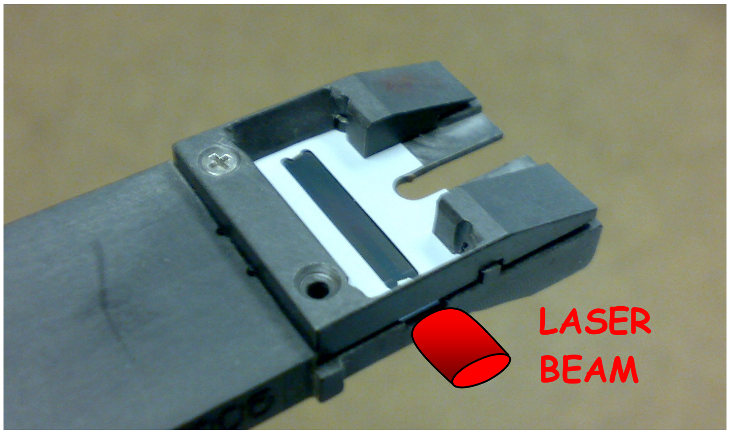

Figure 3.5 – Unmodified INEX FB80 chip in its carrier, with a gasket on it which leaves channels 1 to 3 opened to their environment.

Note that because of the lack of reliable data about this prototype (no fabrication tolerances data, different upper waveguide thickness apparently, etc), it has been decided not to perform any calibration of the upper waveguide (determination of real optogeometrical parameters of the upper waveguide, briefly mentioned in **Section 2.1.3**). Therefore we used the theoretical optogeometrical structure (**Figure 2.4**) in the whole analysis instead of using calibrated data which would have been certainly wrong.

3.2.2. Cleaning procedure

There are 2 reasons for cleaning the AnaChip before each experiment. The first one is to remove all organic contaminants from the surface (after deposition of liquid crystals on the surface for example), and the second one is to make a proper hydrophilic surface, although the AnaChip surface already tends to be hydrophilic because of its chemical composition (the expected contact angle for water at the solid interface for an unmodified AnaChip is 78.17 ± 0.13° [37]).

For that purpose the chip used to be cleaned in Piranha solution (Piranha etching), which is a mixture of sulphuric acid (H_2SO_4) and hydrogen peroxide (H_2O_2). This solution is a strong oxidizer which does exactly what we want (removing organics and hydroxylating the surface). The first chemical process, the fastest, is a dehydration of the surface (removing of hydrogen and oxygen as units of water) since hydration of the sulphuric acid is thermodynamically strongly favourable. The second chemical process, much slower, is an oxidation due to the sulfuric-acid boosted conversion of hydrogen peroxide from a relatively mild oxidizing agent into one sufficiently aggressive to dissolve elemental carbon [38]. The chip therefore ends up with silanol groups on its surface [14]:

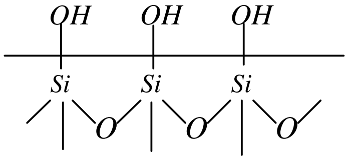

There are a variety of Piranha solution cleaning protocols depending on the proportions of the solution, on the time the sample is soaked into the solution, and on the temperature the solution is heated to mainly. In order to get strongly hydrophilic surfaces, we used in this work the highest proportion of hydrogen peroxide (the oxidizer) allowed for safety reasons, that is to say 1:1 (v/v) concentrated H_2SO_4 (95-97%) and H_2O_2 (35% in water). Note that more hydrogen peroxide than sulfuric acid in the mixture would cause a too exothermic reaction which might cause risks of explosions [39]. Because of these high proportions the solution was not heated, it was already hot enough and it would have required to wait that the solution cools down reasonably before heating it. Note that extreme caution must be taken when preparing, handling and disposing the Piranha solution. The preparation consists in putting very slowly the hydrogen peroxide into the sulfuric acid under a fume hood as smoke is released (note that some documents advise to do the opposite way [40]).

The chip was soaked in the solution directly after preparation during 5 minutes, then put in a bath of ultra-pure water (15 Mohm.cm) where it was gently wiped with a cotton bud (both channel 1 and 3, and both end-faces). After that, it was thoroughly rinsed with ultra-pure water, before being put back in the Piranha solution and left there during 40 minutes. As the chip is introduced in the freshly made solution, bubbles slowly grow on its surface (starting on the edges of the channels) (**Figure 3.6**). This is likely to be due to the oxidizing process which releases more and more oxygen molecules.

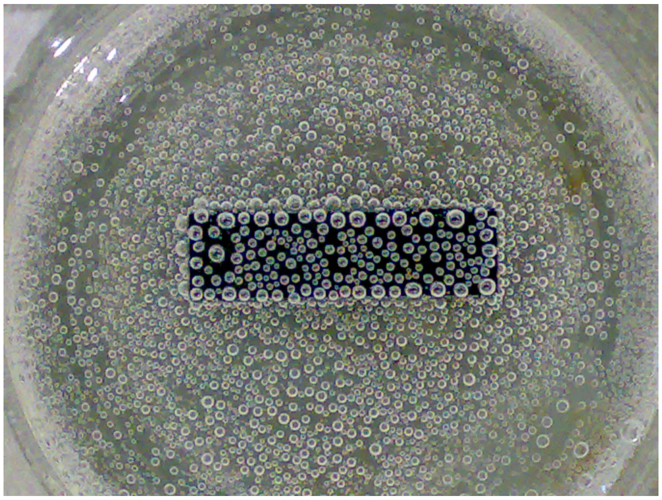

Figure 3.6 – AnaChip left in Piranha solution for a while.

Eventually, the chip was removed from the solution, and thoroughly rinsed with ultra-pure water twice (2 different baths of ultra-pure water), and both channels and end-faces were dried with nitrogen flow during 30 seconds from each end-face of the chip. After that, the chip usually stayed in contact with air (in a plastic box) during 10 minutes before starting the experiment (time required to end the preparation protocol, which will be described in **Section 3.3.2**). Note that the whole procedure was performed in a semi-clean room in order to minimize the amount of impurities which would adsorb once the chip was dried. Moreover, we suppose that the drying process always left some adsorbed water layers on the surface. The thickness of these layers depended on the RH of the environment in which the chip was during the 10 minutes after the cleaning process. Therefore, the initial phases at the beginning of each experiment were those of a chip with water layers on it.

The cleaning protocol described above was always strictly the same before each experiment, therefore it was expected that the surface would exhibit the same degree of hydrophilicity each time. That is of great importance as the degree of hydrophilicity of the surface changes the structure of the water layer [41]. Contact angles have not been measured in this work, however contact angle of 32.1° has been reported in [37] for an AnaChip left 10 minutes into a 7:3 (v/v) concentrated H_2SO_4 and H_2O_2. Given that the contact angle depends on the soaking time into the Piranha solution as well as on its composition [42], we concluded on the basis of results described in [42, 20] that our cleaning protocol (higher proportion of H_2O_2, and sample left much longer) should definitely lead to contact angles between 10° and 20°.

Finally, as explained in **Section 2.2.1**, we can assume that the degree of hydrophilicity of our surface doesn't evolve over the range of chip temperatures we used (from 25 °C to 35 °C) since much higher temperatures are required so that the de-hydroxylation reaction occurs. Moreover it seems reasonable to assume that the silicon oxynitride layer doesn't evolve on the timescale of our experiments which are 1 day maximum.

3.3. Vapour deposition setup

3.3.1. Setup

Experiments performed previously on this topic [14] used a vapour deposition setup different than that of the present study (with a different instrument as well). Basically a simple small aquarium pump and 2 valves used to produce a tiny airflow. This airflow used to pass through a small copper heated oven into which liquid crystals could be injected. In that way, the air-diluted liquid crystal vapour could gently flow through a Tufnol (a thermally insulating material) manifold over the sensor chip.

First tests performed with that configuration (adapted to the AnaLight Quantum) led to very unsteady results, as well as accumulations of adsorbed molecules on the part of the chip which was exposed to the airflow inlet. We suspected that the unsteadiness was due to the use of an airflow (which could contain impurities), associated with the fact that the old oven was too much opened to the environment. Therefore it has been decided to redesign the vapour deposition setup integrating new components. The flow of air roughly controlled has been replaced by a flow of dry nitrogen (inert gas) properly controlled by a flowmeter. The oven has been redesigned so that the system would be more isolated from outside. And the Tufnol manifold design has been changed to a design which would avoid aggregates formation on one part of the chip, allowing more uniform layers to be deposited.

Figure 3.7 shows the whole vapour deposition setup out of the instrument. We can see that the nitrogen flow coming from a nitrogen bottle and controlled with a Platon flowmeter (0-100 sccm, standard cubic centimeter per minute) goes inside the copper oven which is heated by a Eurotherm 808 heater associated with a wirewound resistor and a thermocouple sensor. **Figure 3.8 a** shows the path of the nitrogen flow (blue dotted arrow), guided to a big chamber over the chip via both the oven and the Tufnol manifold, before escaping by the manifold outlets. This configuration allows a more homogeneous deposition (compared to the old configuration for which the airflow used to enter over one extremity of the chip, and leave over the other). Substances to vapour deposit on the surface are put on a ledge inside the oven before closing and starting to heat it (**Figure 3.8 b**). The maximum content of this ledge is 0.1 ml. Finally **Figure 3.8 c** shows the whole system integrated into the AnaLight Quantum, that enables to investigate the vapour deposition of substances with DPI technique.

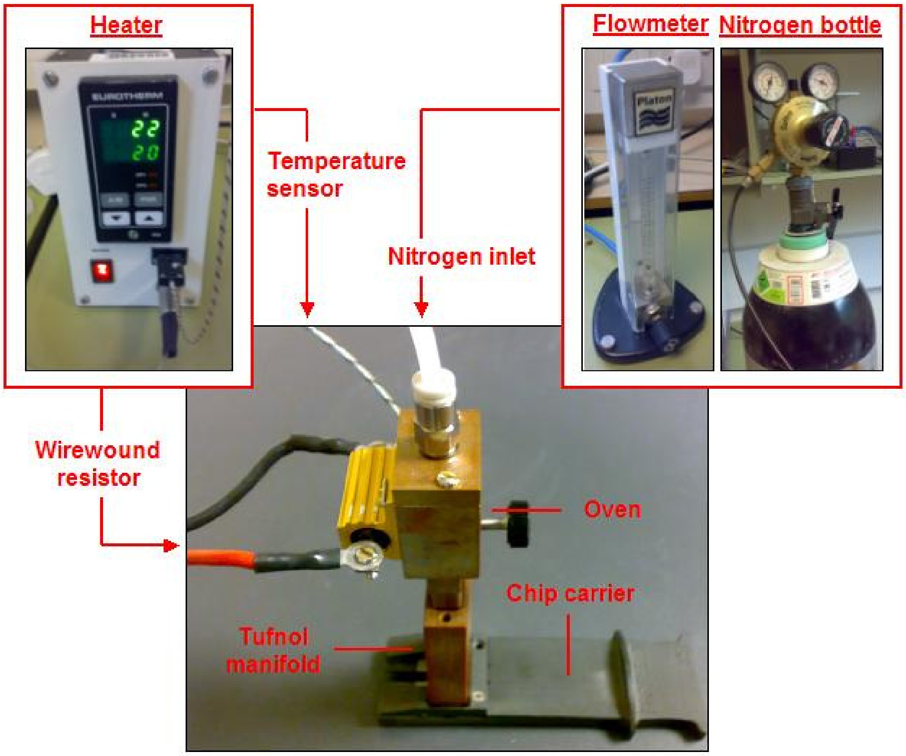

Figure 3.7 – Vapour deposition setup out of the AnaLight Quantum with its heating system and nitrogen flow.

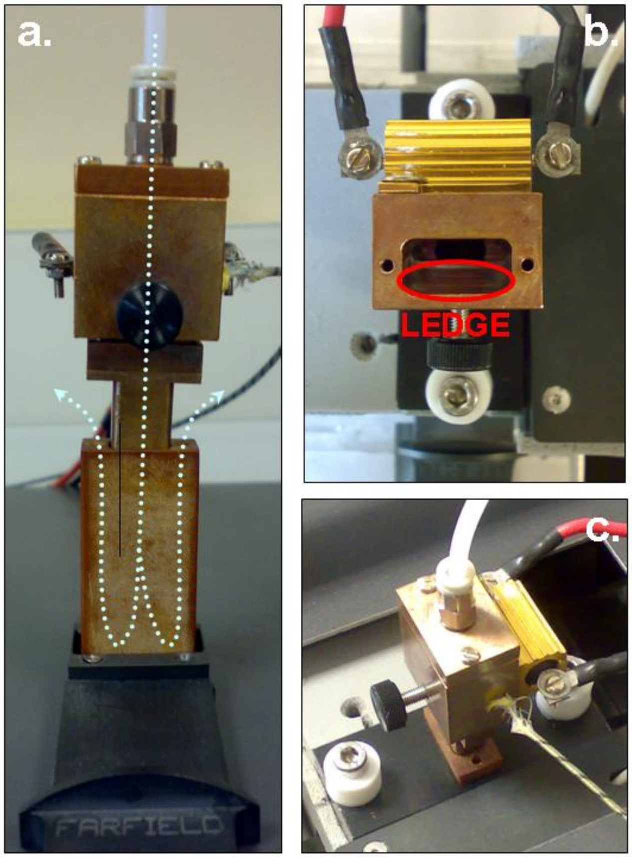

Figure 3.8 – (a) Path taken by the nitrogen flow inside the system. (b) Ledge inside the oven on which substances can be put. (c) Vapour deposition setup integrated into the AnaLight Quantum.

3.3.2. Preparation protocol

In parallel to the cleaning of the chip (detailed in **Section 3.2.2**), it was also required to clean the vapour deposition setup. As it could have some LC in it, we used first of all to wash and wipe each part of the setup (tube inlet, whole oven, manifold, and gasket) below tap water. Then those parts were put in a bath of methanol during approximately 5 minutes, and wiped with a cotton bud. Finally, everything was thoroughly rinsed with tap water, wiped again with tissue paper, and thoroughly dried with nitrogen flow (in order to remove adsorbed water layers on the inner walls of the system as much as possible). The last step consisted in building the vapour deposition setup out of the instrument, heat it to 110 °C, and flowing nitrogen at a flowrate of 100 sccm during 10 to 15 minutes. The idea behind that was to try to desorb more water from the inner walls of the system. Eventually, the oven was opened (cover removed) and the heater turned off, in order to cool down the oven to ambient temperature. According to the test the ledge was either left empty, or filled with 5CB molecules (Aldrich, 4′-pentyl-4-biphenylcarbonitrile, liquid crystal nematic 98%) before closing the oven with its cover. Note that a new syringe was used for each experiment.

An important step of the preparation protocol before each experiment was to define the area on the fringe image from which the parameters (phase and contrast mainly) would be calculated. **Figure 3.9** shows the 3 red windows which allow the user to get one measurement of the parameters on each channel. The size of these windows must be chosen as big as good fringe quality allows. Indeed, the calculated fringe pattern is an average over the pixels of the width of the window, since the fringes are most of the time not so horizontal, the window cannot be chosen as wide as wanted. Moreover, the windows must be placed so that contrasts be maximized (to minimize static error), so that fringes have a nice shape (avoiding optical defects on the image, due to dust on the glass in front of the CCD camera for instance), and so that the phase difference between TE and TM be minimized. The chip is always set in the same way in its carrier, therefore we always get approximately the same fringe image. Since the defects don’t move we can put the windows approximately in the same place each time as shown on **Figure 3.9**. We always used a length of 512 pixels, and a width of 7 pixels.

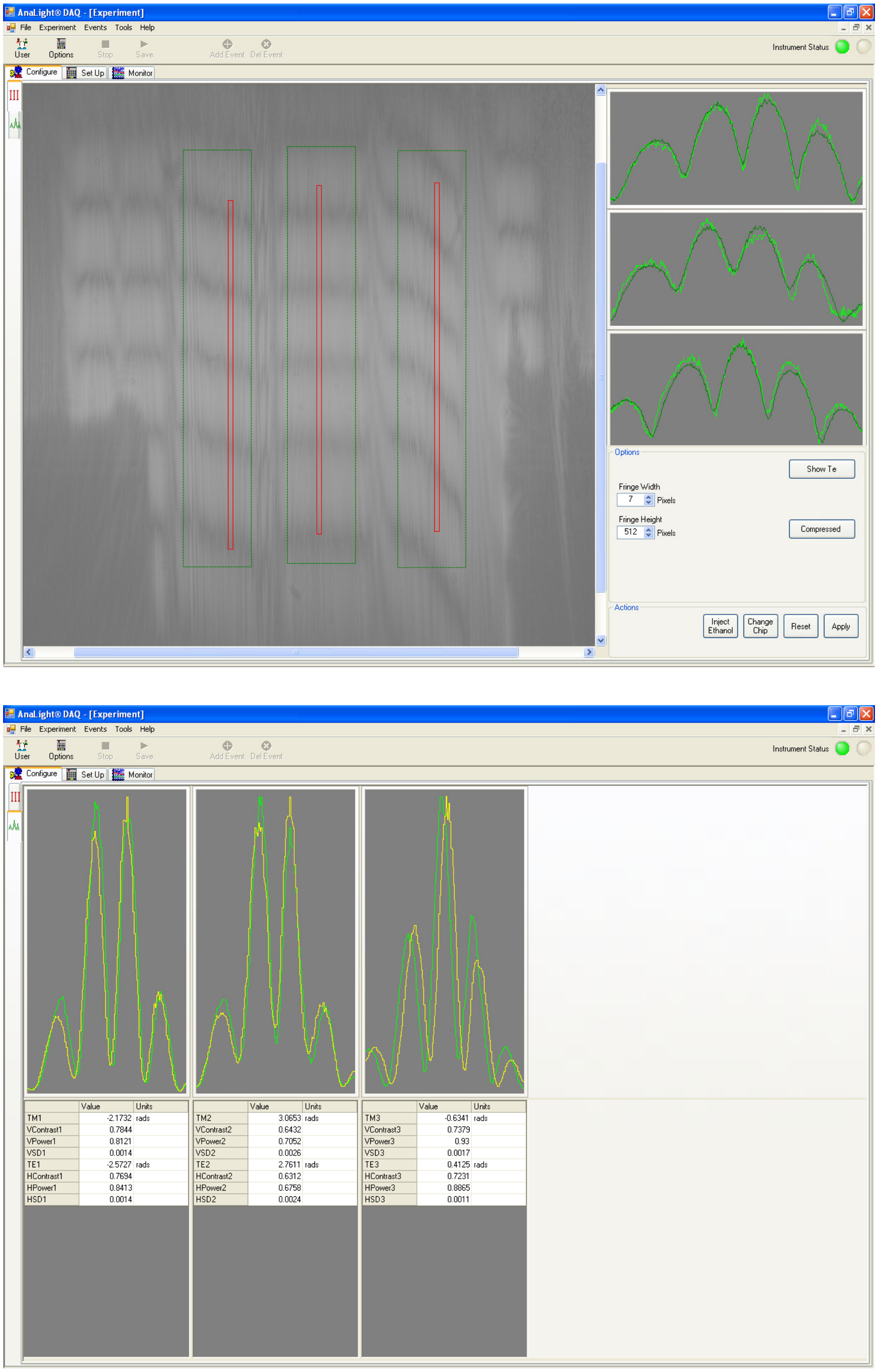

Fringe Width 7 Pixels

Fringe Height 512 Pixels

	Value	Units
TM1	-2.1732	rads
VContrast1	0.7844	
VPower1	0.8121	
VSD1	0.0014	
TE1	-2.5727	rads
HContrast1	0.7694	
HPower1	0.8413	
HSD1	0.0014	

	Value	Units
TM2	3.0653	rads
VContrast2	0.6432	
VPower2	0.7052	
VSD2	0.0026	
TE2	2.7611	rads
HContrast2	0.6312	
HPower2	0.6758	
HSD2	0.0024	

	Value	Units
TM3	-0.6341	rads
VContrast3	0.7379	
VPower3	0.93	
VSD3	0.0017	
TE3	0.4125	rads
HContrast3	0.7231	
HPower3	0.8865	
HSD3	0.0011	

Figure 3.9 – Screenshots from AnaLight DAQ software showing the 3 red windows (up) from which are calculated 3 fringe patterns with their parameters (down).

3.4. Tools for data analysis

3.4.1. Slab software

The Slab program is a 1D mode solver allowing the user to define a unidimensional structure by its optogeometrical parameters (thicknesses and RIs). For instance, it is possible to find the phase changes $\Delta\phi_E$ and $\Delta\phi_M$ which occur when a given isotropic adsorbed layer is deposited onto a defined AnaChip structure (the ideal one shown **Figure 2.4** in our case). Indeed, for each polarization the Slab program gives us the effective indexes of the sensing waveguide (upper waveguide) with and without an adlayer on it ($N_{adlayer}$ and N_{air}), that gives straightforwardly the phase changes from the following formula [32]:

$$\Delta\phi = k_o \cdot l \cdot \Delta N = k_o \cdot l \cdot (N_{adlayer} - N_{air}) \tag{3.1}$$

where k_0 is the free-space wave vector, and l is the length of the exposed region (see **Figure 2.4**).

In the case of an anisotropic modeling, an isotropic RI is fixed for the adlayer as explained in **Section 2.1.1**. At 25 °C and 632.8 nm, the RIs of 5CB are $n_o = 1.53187$ and $n_e = 1.706$ [43], that gives an isotropic index $n_{iso} = 1.59203$ using the following formula [32]:

$$n_{iso} = \sqrt{\frac{n_e^{2} + 2n_o^{2}}{3}} \tag{3.2}$$

Then, for each polarization, the adlayer thickness is manually varied until finding a thickness which corresponds to the experimental effective index (calculated from the experimental phase change with **Equation 3.1**). We therefore get 2 different “virtual” thicknesses t_{TE} and t_{TM}, corresponding to the 2 different experimental phase changes. From that an average “real” thickness $t_{average}$ is calculated with the following formula [32] (note that the same method is applied to find the thickness of an isotropic adlayer knowing its RI, and the 2 different experimental phase changes):

$$t_{average} = \frac{t_{TM} + 2t_{TE}}{3} \tag{3.3}$$

Finally, this average thickness is fixed for the adlayer, and the adlayer RI is now manually varied until finding a RI which corresponds to the experimental effective index. This is performed for each polarization, therefore we get n_{TE}, n_{TM}, and hence the birefringence $\Delta n = n_{TM} - n_{TE}$. The whole process must be performed for each experimental value i.e. for each couple ($\Delta\phi_E$, $\Delta\phi_M$).

3.4.2. Mathcad program

The theory described in **Section 2.3.2** and **Appendix B** has been implemented with Mathcad by Tan, and used by us with our own parameters. From **Equation 2.6 – Section 2.3.2**, it is possible to plot n_{TE} and n_{TM} (horizontal and vertical RIs of the adlayer sensed by TE and TM polarizations) against the orientation angle θ of the molecules within the adlayer (**Figure 3.10**). Note that TM polarization tend to be more sensitive to the re-orientation of molecules within the adlayer since n_{TM} exhibits more amplitude of variation than n_{TE} (since TM evanescent field is greater than TE evanescent field – **Figure 2.6**).

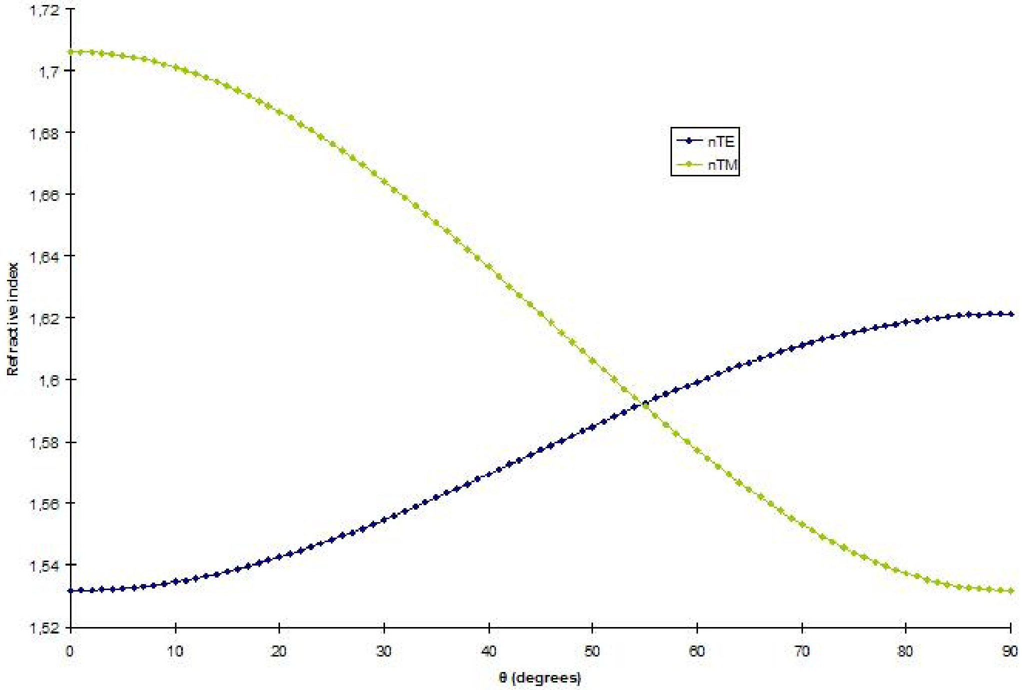

Figure 3.10 – Simulation of the evolution of the adlayer RIs sensed by TE and TM polarizations according to the polar angle.

From this program it is also possible to plot (**Figure 3.11**) the phase change ratio against the polar angle (similar chart to that of **Figure 2.18** which was based on the parameters used by Tan). We added on that chart the birefringence $\Delta n = n_{TM} - n_{TE}$ using values from **Figure 3.10** in order to notice the link which exists between the curves. Note that the birefringence becomes 0 for an average polar angle of 54.7°, the so-called "magic angle" (at that point the layer is isotropic in appearance). A relationship has been found for typical values of the ratio obtained experimentally in order to enable us to get the evolution of the birefringence from the evolution of the ratio obtained experimentally (**Figure 3.12**).

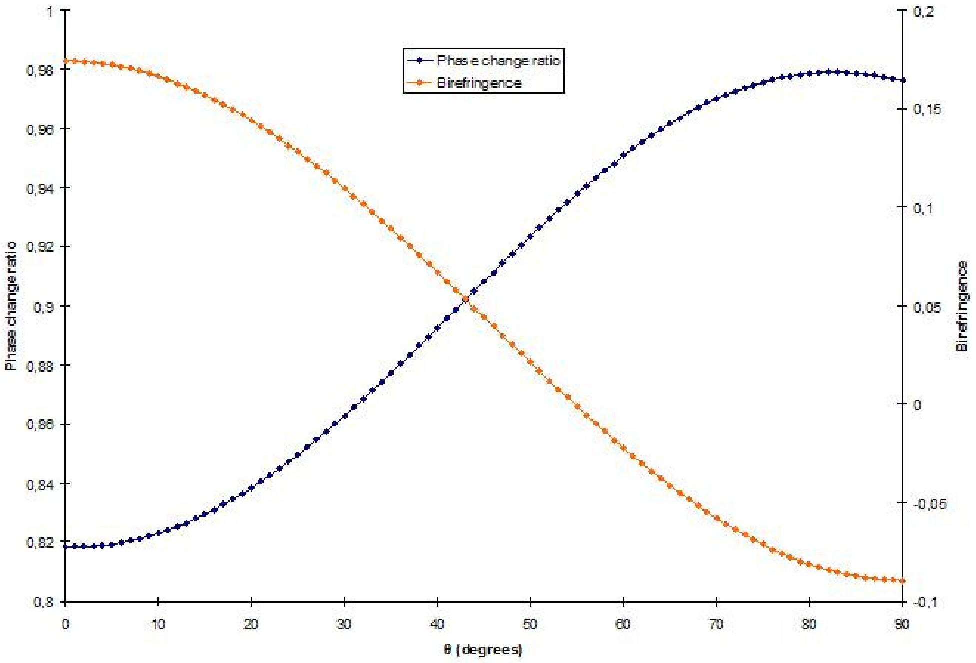

Figure 3.11 – Simulation of the evolution of the phase change ratio according to the polar angle (blue curve), and birefringence determined from **Figure 3.10** for comparison (orange curve).

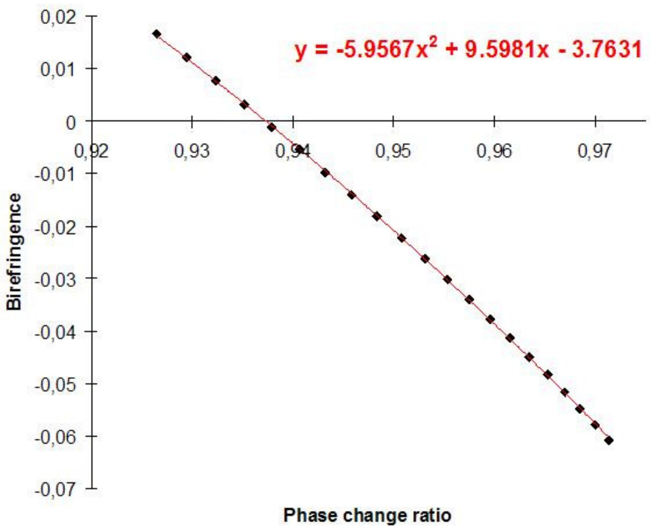

Figure 3.12 – Equation linking simulated phase change ratio and birefringence for a range of typical phase change ratio values obtained experimentally.

Finally, it is worth noting that the Mathcad program uses an alternative way to determine the thickness of a monolayer (different than that described in **Section 3.4.1**). **Figure 3.13** shows the geometrical model (rod-like molecule) which enables the determination of the monolayer thickness according to the polar angle θ. In this work we used a molecule length of 17 Å, and a molecule width of 4 Å for the 5CB molecule [32].

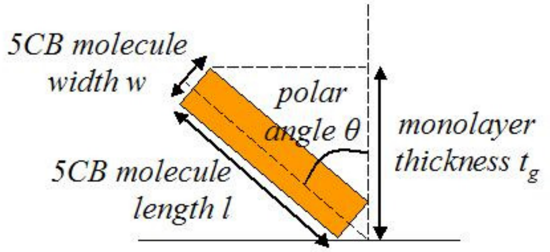

$$t_g = l\cos\theta + w\sin\theta$$

Figure 3.13 – Geometrical model used to calculate the monolayer thickness.

3.4.3. Farfield AnaLight Explorer software

The AnaLight Explorer allows the user to analyse the results acquired with the AnaLight DAQ by calculating the calibrated parameters, applying the linearization to the data, calculating RI, thickness and birefringence of the adlayer, and additional possibilities which are not useful in the present study.

We used the software to calculate the evolution of the layer optical anisotropy (birefringence). As already mentioned we did not calibrate the chip in this work, therefore we had to define a fake calibration and set the upper waveguide optogeometrical parameters to their theoretical values (RI of 1.52 and thickness of 1 μm) to enable any calculations. We assumed the RI of the environment of the chip surface before any deposition to be 1 (nitrogen). We also set the refractive index increment to 0.992 cm^3/g which was deduced from the density of the 5CB molecules we used (1.008 g/ml at 25 °C [44]). This value has been chosen only for strictness as we know from previous tests that it does not play any role in the birefringence calculation for a vapour deposition experiment. Finally, we chose to fix the RI of the adlayer to its isotropic value (calculated in **Section 3.4.1**).

Note that a manual birefringence calculation (with Slab, as explained in **Section 3.4.1**) and an automatic calculation with the AnaLight Explorer have been compared for a 5CB vapour deposition experiment (**Figure 3.14**). We can see that the data points calculated with Slab fit quite well with the curve provided by the software. It is likely that the method of birefringence calculation implemented in the AnaLight Explorer is no more than an automated version of the manual method described in **Section 3.4.1**. Note that the software doesn't display birefringence values for very small phase changes: that is probably because oscillations on the birefringence became too large and not reliable enough.

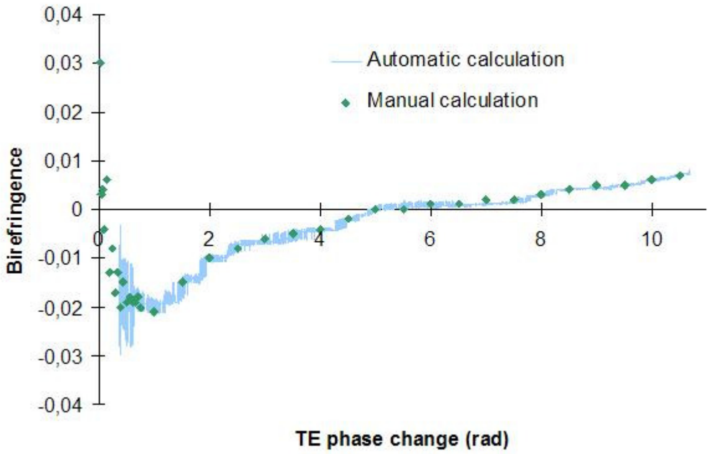

Figure 3.14 – Evidence of the fact that the birefringence calculation performed by the AnaLight Explorer is based on the method described in **Section 3.4.1**.

Chapter 4. Experimental results

4.1. Water layers on hydrophilic silicon oxynitride surfaces

4.1.1. Drying the surface of the chip

The experiment shown in **Figure 4.1** has been performed after the usual preparation protocol described in **Section 3.3.2**. Only the chip temperature and the nitrogen flowrate are controlled in this experiment (the temperature of the oven remains at ambient conditions). The first 15 minutes correspond to the chip temperature stabilization (from the initial temperature, it stabilizes to 25 °C ± 1.5 mK). A nitrogen flow of about 100±5 sccm (standard cubic centimeter per minute) is started afterwards. That causes the phases (TE3 and TM3) to decrease until an equilibrium is reached (~-0.13 rad). At that point, the chip temperature is set to 35 °C, that causes the phase to decrease more. Finally, even though the equilibrium was not reached yet, the chip was cooled down to 25 °C in order to observe the response of the phases. We observe that the phases start to increase again but don't reach their initial level (~-0.13 rad) in a similar duration. Note that channel 2 phases are only affected by changes in temperature, as the upper waveguide surface is not exposed to the environment for this channel.

We can straightforwardly say that the first phase decrease is not due to a thermo-optic effect (colder nitrogen flow cooling down the chip for example) as the channel 2 phases remain completely constant when the nitrogen flow is started. The decrease we observe must be due to a decrease in density or thickness of the adlayer. The literature review performed in **Section 2.2** allows us to propose that some water molecules are progressively removed from the chip surface by the nitrogen flow. In fact, it can also be seen as a progressive decrease of RH (relative humidity) in the system until an equilibrium is reached (since the higher the RH, the more water molecules adsorbed on the surface). At that point, it becomes difficult to decrease the RH more (and remove more adsorbed water molecules) as the setup we use remains quite basic (no vacuum system for instance).

However, it is possible to do so by bringing thermal energy to "help" molecules to desorb. That is why the chip temperature is increased to 35 °C. The result is in total agreement with our expectations as the phases appear to decrease more. Finally, the amount of water molecules adsorbed on the surface at 25 °C before and after the temperature increase is compared: not surprisingly, the phase does not reach its initial level (~-0.13 rad), as the nitrogen flow certainly pushed some desorbed molecules out of the system (it would take more time for those to come back close to the surface and be re-adsorbed). It is interesting to note that TM3 phase looks more sensitive than TE3 phase to the temperature change as it will be observed again in other cases further down (**Section 4.2.2**).

This test shows how it is possible to desorb water molecules from our hydrophilic silicon oxynitride surface using a dry nitrogen flow and controlling the chip temperature. However, some water molecules are certainly still adsorbed on the surface, and some additional procedures would be required to remove them (thermal annealing processes, etc). In the next tests performed in this study, only the nitrogen drying process has been performed (at the same flowrate, about 100±5 sccm) since additional desorption using thermal energy takes at least 2 hours more for each experiment.

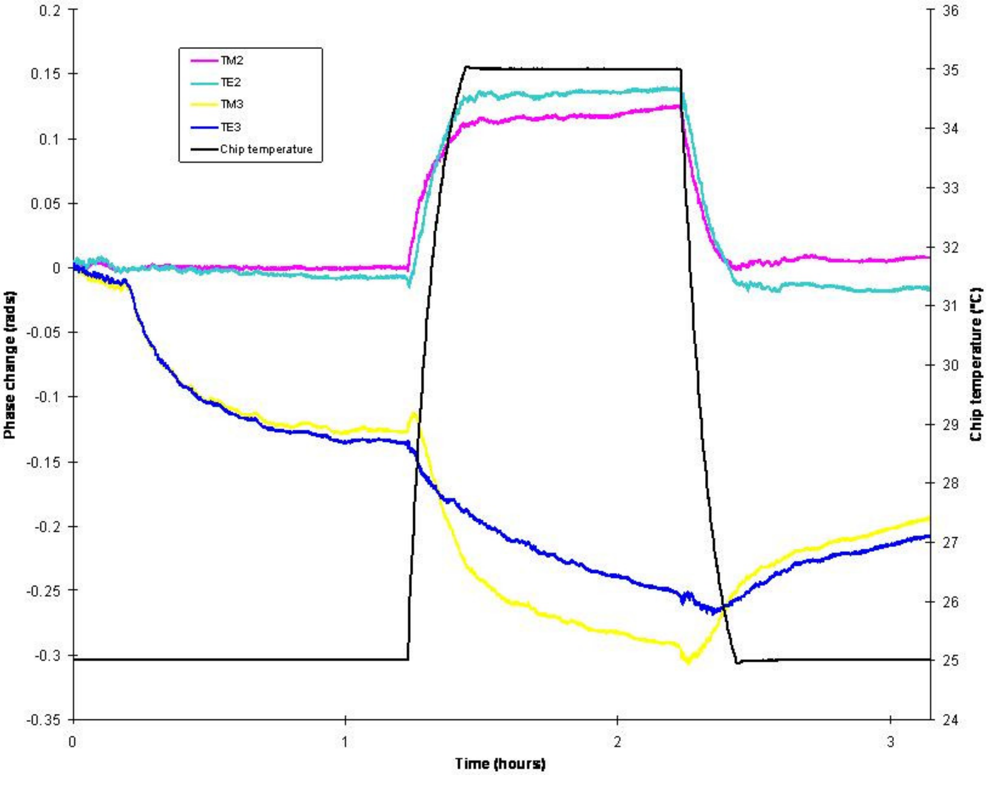

Figure 4.1 – Effect of starting the nitrogen flow and of increasing the chip temperature on the phases.

4.1.2. Re-adsorbing water according to the RH

It has been shown before that water layers naturally formed on hydrophilic surfaces can be desorbed partially using our system. At that point it was interesting to compare the re-adsorption of water molecules in 2 different configurations: for the chip suddenly exposed to ambient RH on the one hand, and for the chip exposed to a high RH environment on the other hand. Ideally, the best would have been to create different levels of RH with the vapour deposition setup (controlling the amount of water inside, the nitrogen flowrate and the oven temperature), but the lack of RH sensor would have required to perform thermodynamical calculations which appeared to be too complex for the system we used (opened to ambient via the manifold outlets, nitrogen flow, etc). That is why it has been decided to study only those 2 extreme cases.

4.1.2.1. First case: ambient RH

In this first test (**Figure 4.2**) the upper part of the vapour deposition setup (copper oven) has been suddenly removed after drying the surface. The chip was therefore exposed to the air through the inlet and outlet holes of the Tufnol manifold. That caused the phase to increase progressively with two clear parts on the chart: an increase during almost 1 hour followed by a slower one which lasted almost 20 hours at the same rate in average. Phase contrasts are quite constant over the whole experiment.

Our expectations for this test were the following: as soon as the dried chip is exposed to ambient air (mainly nitrogen, oxygen and humidity), water molecules should have adsorbed very quickly on the hydrophilic surface, and a constant phase should have been reached after some time (according to the ambient RH). However, the first increase took very long (almost 1 hour), and the phase kept increasing linearly afterwards. The reason for this long adsorption must be that the Tufnol manifold was actually filled with dry nitrogen when the oven has been removed. Therefore, it is likely that the air progressively fell down on the surface (mixing up with pure nitrogen), and lost some of its humidity on the dry walls of the Tufnol manifold. However, we didn’t find any explanation for the fact that the equilibrium has not been reached even after 20 hours. Besides that, no noticeable variations have been observed on the contrast, meaning that the process of adsorbing/desorbing water molecules occurs in a quite homogeneous way.

Apart of that, the chip temperature and the channel 2 phases remain within common values (±1.5 mK and ±15 mrad respectively) meaning that the thermal stability of the chip remains really good during this long term experiment. Note that the acquisition step was changed from 1 second to 5 seconds about 3 hours after the beginning of the experiment in order to decrease the amount of data accumulated overnight.

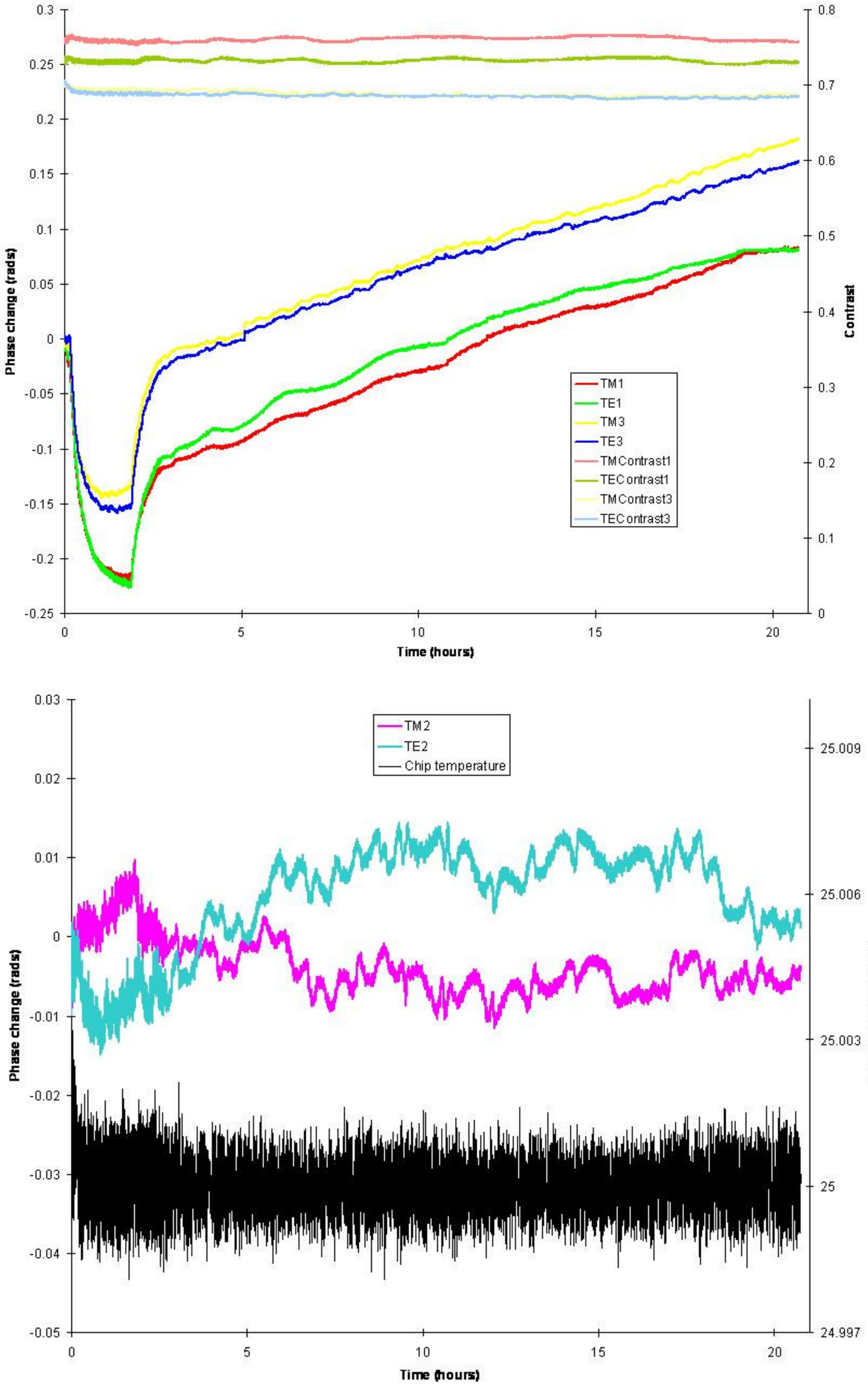

Figure 4.2 – Desorption of water molecules, and re-adsorption for the chip exposed to ambient RH.

4.1.2.2. Second case: high RH

Some preliminary tests showed that it was not possible to dry the chip surface while liquid water was on the ledge (that is not the case for liquid crystals as it will be seen further down). The reason was probably that water molecules are much more volatile than LC molecules, therefore even at ambient temperature the nitrogen flow could not dry the chip surface properly as it was always carrying a certain amount of water molecules toward the surface. Therefore, a different cover (with a pinhole) has been used in order to be able to inject water when required (**Figure 4.4 up**). In that way it was possible to create an environment saturated with water (RH supposed to be close to 100%) only by injecting water on the ledge and heating the oven to a certain temperature just after drying the surface of the chip.

Therefore in this second test (**Figure 4.3**), the nitrogen flow was stopped, liquid water was injected on the ledge, and the oven was heated first to 50 °C and later to 80 °C, just after drying the surface. Phases increase with two different rates (one for each oven temperature) before suddenly starting to increase up to incredibly high values (hundreds of radians, not completely represented on the chart). At that moment all the contrasts dropped.

As shown in **Section 2.2.2**, [27] studied adsorbed water on silicon oxide surface: the adsorption isotherm depicted **Figure 2.13** shows that as P/P_{sat} increases (equivalent to RH), the water layers structure evolves from an ice-like structure to a liquid water structure. It is likely that the same phenomenon happened in this experiment (the constant surface temperature, 25 °C, allows to talk about "isotherm" in our experiment). Indeed, for a given oven temperature, an equilibrium (certain level of RH) is reached after a certain time. For an oven temperature of 50 °C, the water layer was not thick enough (RH not high enough) to reach the dew point, whereas that happened for an oven temperature of 80 °C. This explanation got confirmed observing the chip surface after the experiment (**Figure 4.4 down**): the surface was fully covered by micro-droplets. Their formation made the light to be suddenly scattered, that caused the drops of contrasts. Note that the values reached by the phases after condensation are not believed to have any meaning, since the contrasts are very low. A look on the standard deviation of the phase (automatically calculated by the software) confirms this idea as it goes from ±0.3 mrad before condensation up to ±150 mrad afterwards.

The chip temperature and the channel 2 phases on the second chart show both the condensation of water on the surface and the changes of the oven temperature. Indeed, when the oven temperature increases, the heat diffuses toward the chip causing a tiny increase (less than 2 mK) on the chip temperature curve which is later balanced by the temperature control of the AnaLight Quantum. The two steps, 50 °C and 80 °C, can be viewed on this curve (encircled in green), as well as the opposite phenomenon at the end of the test (when oven is turned back to ambient, it doesn't heat the chip anymore, therefore the chip temperature starts decreasing before the temperature control brings it back to 25 °C). Note that the 15 mK sharp peak in the temperature chart (encircled in red) appears to be an anomaly of the temperature control which happened randomly sometimes during experiments. Besides that, oscillations on channel 2 phases strongly increased as soon as condensation occurred. Channel 2 should not normally be affected by surface phenomena but in that case it is likely that micro-droplets of water stick on the exposed region edges (close to the reference channel) and causes the light to reflect in a different way inside the chip.

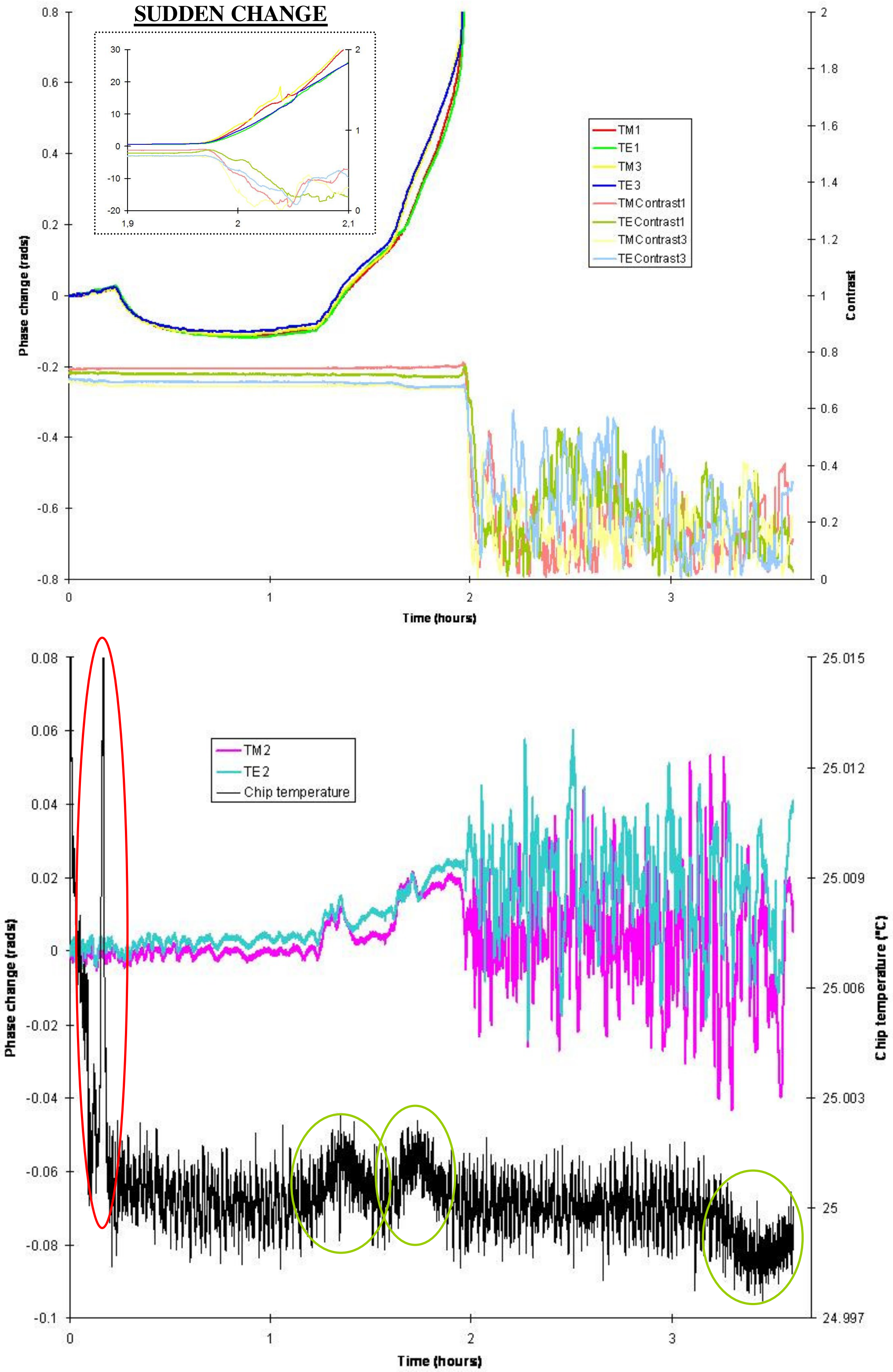

Figure 4.3 – Desorption of water molecules, and re-adsorption for the chip exposed to high RH.

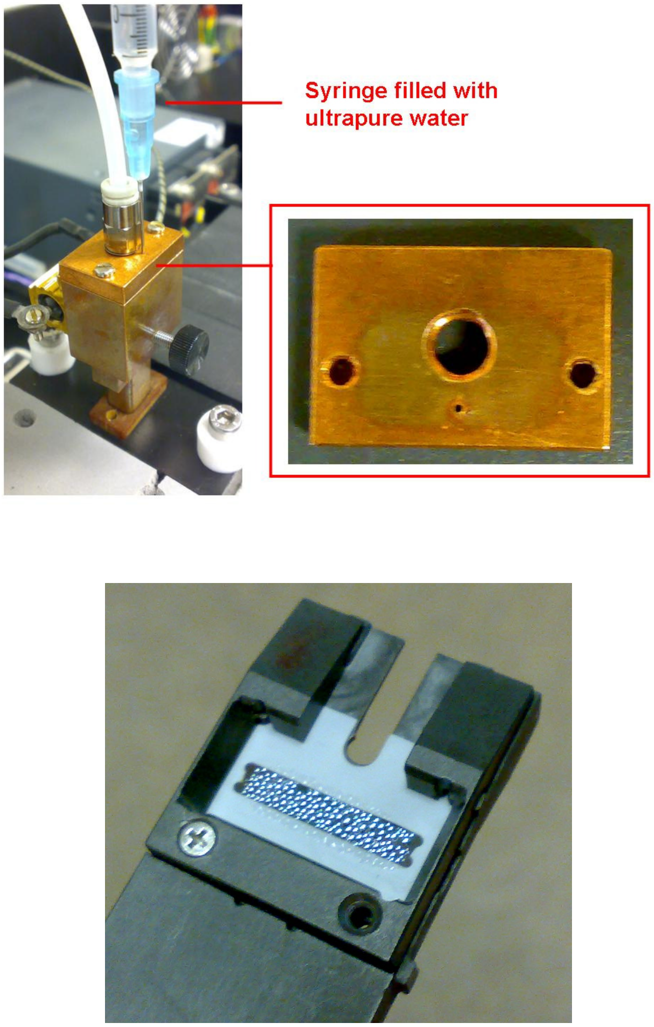

Figure 4.4 – Pictures of this experiment: (up) cover with pinhole in the setup, (down) condensation on the chip (photo taken just after the end of experiment).

4.2. 5CB deposition on hydrophilic silicon oxynitride surfaces

One aim of this study was to find the effect of the water layer naturally present at the chip hydrophilic surface in order to determine whether or not it plays a role during LC deposition. The following tests therefore compare LC deposition onto wet and dry hydrophilic surface. For reliability of results, each experiment has been associated to a reference test, which consists in exactly the same test/protocol but without putting any LC molecules on the oven ledge before starting the experiment.

4.2.1. Liquid crystal tests

Both tests in this section (**Figure 4.5** and **Figure 4.6**) are based on the same experimental steps. After the usual preparation protocol, a couple of LC droplets were injected in the oven before closing it with its cover (normal cover with no pinhole this time, in order to isolate the system as much as possible from outside). The experiment was then started, and temperature stabilization was waited as usual. In the first experiment (**Figure 4.5**), the oven was then turned on to 110 °C, and the nitrogen flow was started at about 100±5 sccm. By contrast, in the second experiment (**Figure 4.6**), the surface was first dried before turning the oven and the nitrogen flow on (the peak on the phases when the nitrogen flow started was due to a sudden blockage of the flowmeter). We observe an increase of phases on both experiments (between about 350 and 550 mrad/min depending on the test, the channel and the polarization) until we stop both the nitrogen flow and the heater (when the contrast starts dropping sharply). At that point, phases start to decrease slowly (between about 30 and 35 mrad/min), except that it accelerates when the chip temperature is increased from 25 °C to 35 °C (between about 100 and 125 mrad/min). At the same tine, contrasts slowly come back to higher values.

Both LC deposition tests show a non-linear increase stage followed by a pretty linear deposition afterwards. This is due to the fact that the oven starts from ambient temperature and reaches temperatures as high as 120 °C in a non-linear way, before stabilizing to 110 °C. As soon as the temperature starts rising, the vapour pressure of 5CB molecules starts to increase in the system, LC molecules are carried by the nitrogen flow toward the surface, and they progressively adsorb due to intermolecular forces (that causes the phases to increase). During the deposition, contrasts usually oscillate because of the static error explained in **Section 2.1.3** (see **Figure 2.9 right** where the contrast oscillates as the phase increases). When the contrast starts dropping, it means that the adlayer becomes less and less homogeneous (surface scattering starts to occur). Some preliminary tests showed that the phase became very unsteady for low contrast values (not reliable anymore), that is why it has been decided to study the deposition only up to the point where contrasts start dropping sharply.

Observing channel 2 chart (for both tests), we clearly see that the hot nitrogen flow has an effect on the surface since channel 2 is not affected by adsorption, and since the chip temperature is maintained to 25 °C at this stage. Therefore we can assume that the same kind of thermo-optic effect also occurs on channels 1 and 3, consequently a part of the phase changes we observe must be due to thermal effects (not only adsorption of LC molecules). Interestingly, we notice in both experiments that channel 2 phase changes are about the same order of magnitude for the chip heated by a hot nitrogen flow from upward (oven temperature of 110 °C) compared to the chip heated to 35 °C by the temperature control system from downward (although the first temperature change is more unsteady and less reproducible than the second one).

After stopping both the nitrogen flow and the heater, the steady state in which a constant amount of 5CB molecules was carried and adsorbed on the surface is suddenly disrupted. Since it takes some time for the oven to cool down to the ambient temperature (almost 20 minutes to reach temperatures below 30 °C), the vapour pressure of 5CB molecules remains quite high just after stopping flow and temperature. However, the most important here is that LC molecules cannot be carried to the surface anymore since the nitrogen flow is stopped, and since hotter gases in the oven should stay above colder gases in the Tufnol manifold (preventing LC molecules to reach the surface). Consequently, it is likely that some LC molecules start straightforwardly to desorb from the chip surface (the phase decreases). As for water layer desorption, it was expected that an increase of the chip temperature would give additional energy to the adsorbed molecules so that they could desorb more easily: that has been confirmed in both experiments as the rate of desorption increased when the chip was heated up to 35 °C in both experiments.

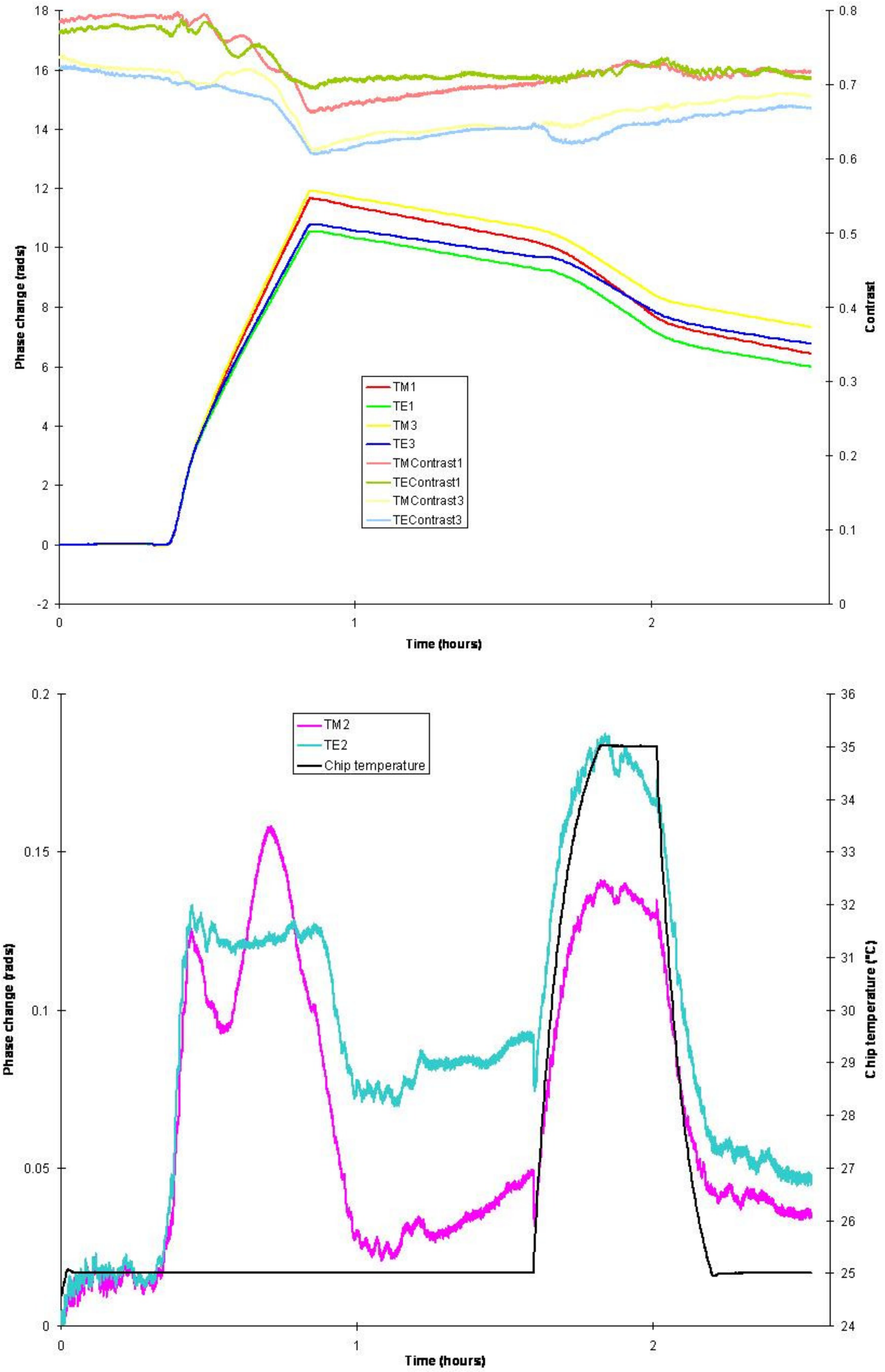

Figure 4.5 – Adsorption and desorption of LC molecules on wet surface (no drying process performed initially).

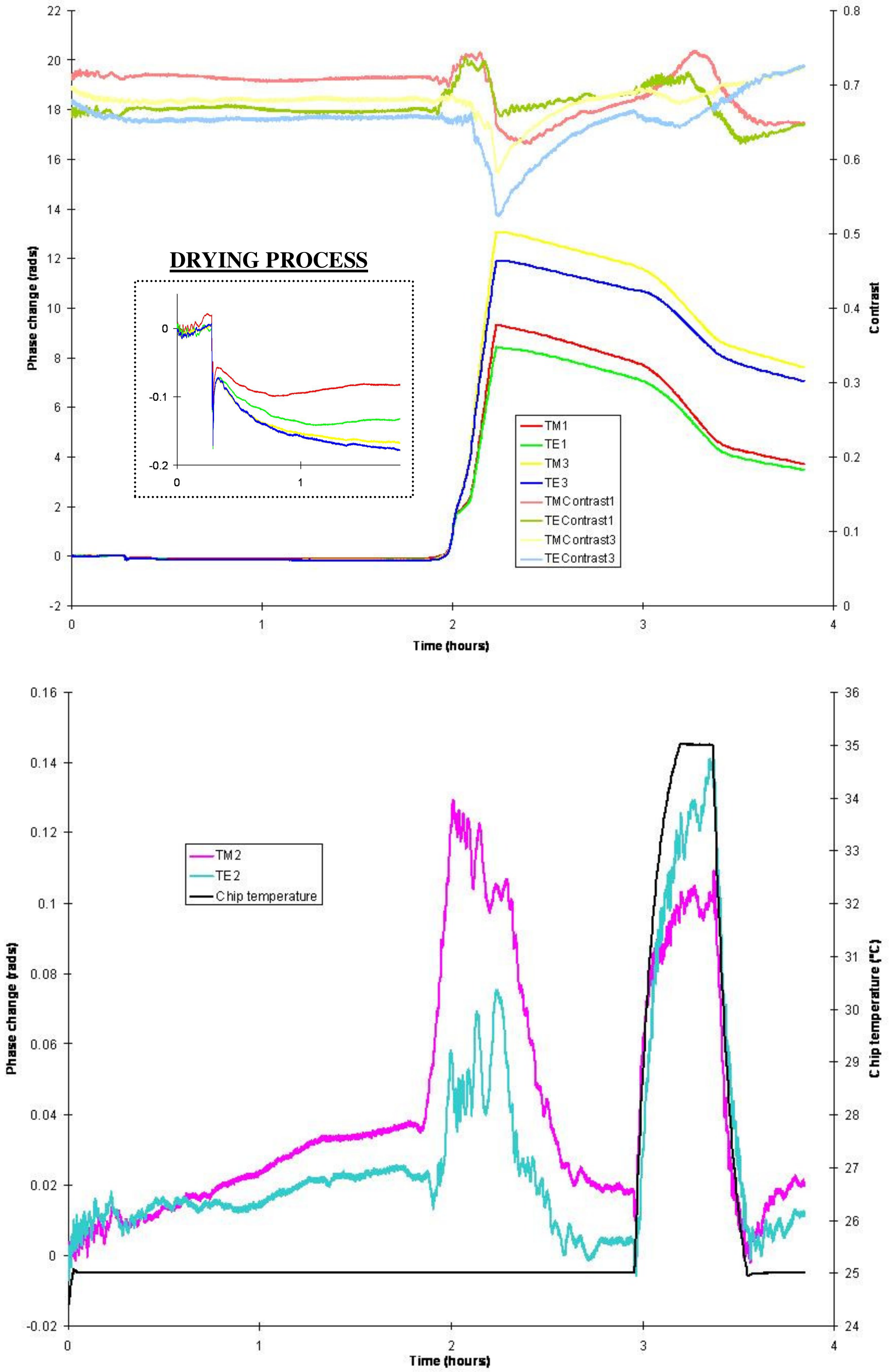

Figure 4.6 – Adsorption and desorption of LC molecules on nitrogen dried surface.

4.2.2. Reference tests

As already mentioned, a lot of care has been taken so that reference tests be really similar to original tests, with the unique difference that no LC molecules were put into the oven before the experiment starts. First of all the usual preparation protocol was performed, and the chip temperature stabilization was waited just after starting the experiment. Then, the oven was turned on to 110 °C, and the nitrogen flow was started at about 100±5 sccm (straightforwardly for test depicted in **Figure 4.7**, and after drying the surface for test depicted on **Figure 4.8**). We observed an increase of phases (between 650 and 800 mrad depending on the test, the channel, and the polarization) until we stop both the flow and the heater (at the same time as when they had been stopped in the original LC experiments). Note that an unexpected ripple happened during the phase increase on the first test (for wet surface). A zoom of the temperature chart shows 2 anomalies on the curve (encircled in red) as well as the effect of the oven temperature changes (encircled in green), similarly to experiment depicted in **Figure 4.3** (water adsorption in high RH environment). The second anomaly must be responsible for the ripple observed during the phase increase. Eventually, after stopping flow and heater, the phases decrease with an acceleration when the chip temperature is increased (much clearer for TM phases than for TE phases). Nothing special should be mentioned about contrasts for those tests.

Basically, we clearly see that even though no LC molecules are present in the oven, there is still a phase increase. This increase is obviously much smaller than that observed during LC deposition (which was between 8.5 and 13.5 rad). A quick analysis of the way the vapour deposition setup is cleaned lead us to assume that water molecules played an important role once again. Indeed, it is likely that LC and methanol molecules are totally removed from the system during the wiping and rinsing processes. The drying process with nitrogen in the clean room, as well as the heating process of the vapour deposition setup, should also remove water molecules from the system. But as we know from the literature review, there are always water molecules remaining on surfaces. Therefore it seems reasonable to assume that at ambient temperature, a certain amount of water molecules are adsorbed on the inner walls of the vapour deposition setup. When the oven temperature increases, a lot of those molecules probably desorb from the wall and the RH increases in the system. The nitrogen flow carries them toward the hydrophilic surface on which they re-adsorb quite easily. Consequently, the phase change obtained during LC deposition could not only be due to LC adsorption and thermal effects, but also to water adsorption. In fact we think that water adsorption is far much less when LC adsorbs, but that will be discussed in the **Section 5.3.1**.

Interestingly, the desorption of molecules after stopping flow and heater occurs in a similar proportion for both LC and reference tests: between 1/3 and half of what adsorbed on the surface desorbs in about 1 hour 45 minutes in total (with a 30 minutes stage at higher chip temperatures). That could mean that the waveguide surface have approximately the same degree of hydrophilicity in both LC and reference tests (that is what we expected by performing each time strictly the same cleaning protocol). Different responses occur according to the polarization when the temperature is increased to 35 °C. Apparently that did not happen for LC deposition, whereas it did happen for water desorption with temperature (**Figure 4.1** – TM phase was clearly much more affected by the temperature increase than TE phase was). Let's observe al the phase changes on channel 2 due to the increase of the temperature (**Figure 4.1** and **Figures 4.5 to 4.8**): each time TE phase increases more than TM phase does, that is consistent with the fact that TE modes are more confined in the chip so should be more sensitive to the chip temperature (see **Figure 2.6** – charts of the TE and TM evanescent fields). Therefore it is likely that TE phase decreases less than TM phase simply because the temperature increase causes TE phase to increase more than TM phase. A comparison between channel 2 and channels 1 and 3 responses when the chip temperature is changed shows clear shape similarities for each test, that confirms what has been just said.

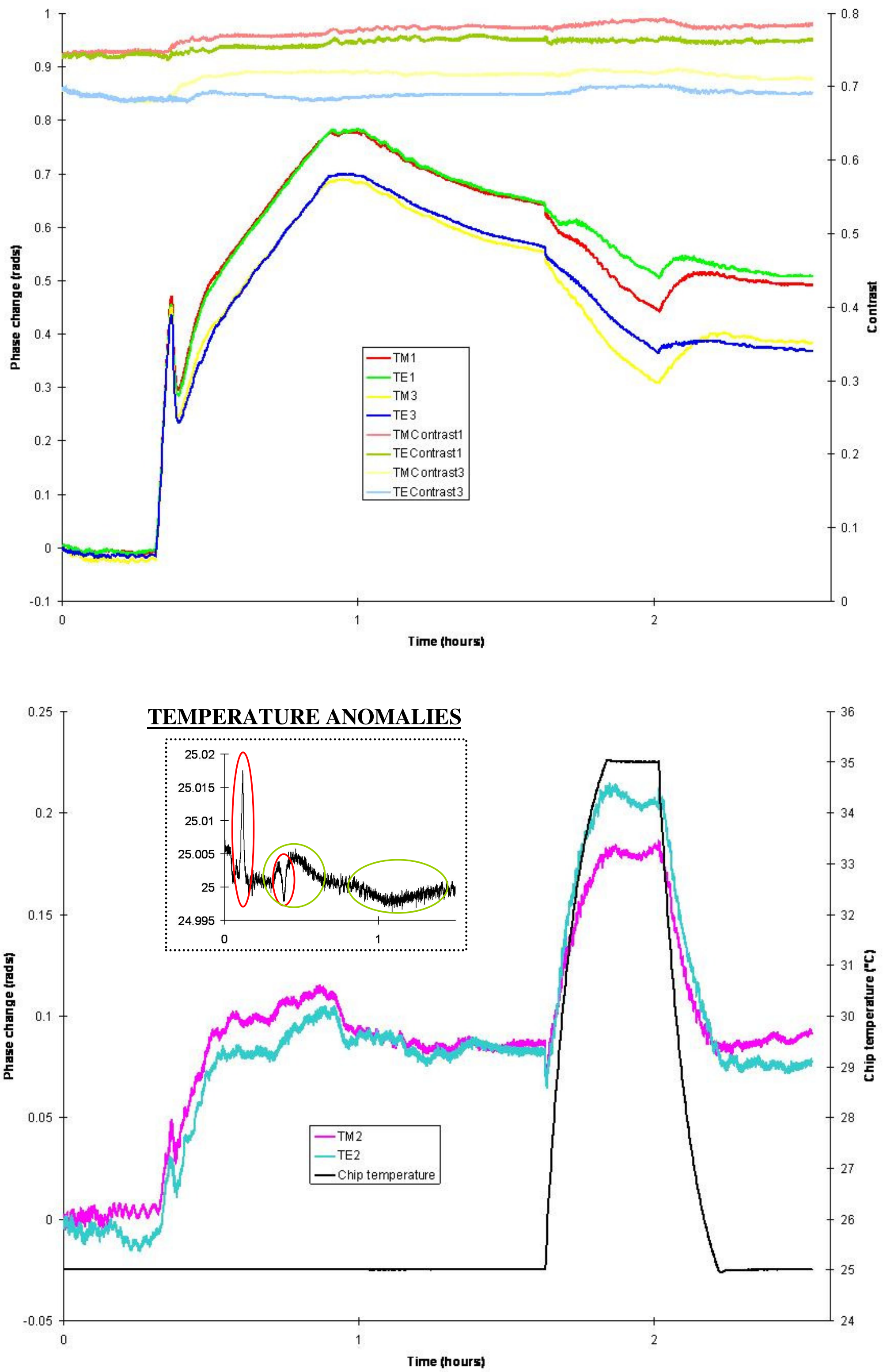

Figure 4.7 – Reference test associated to LC experiment on wet surface.

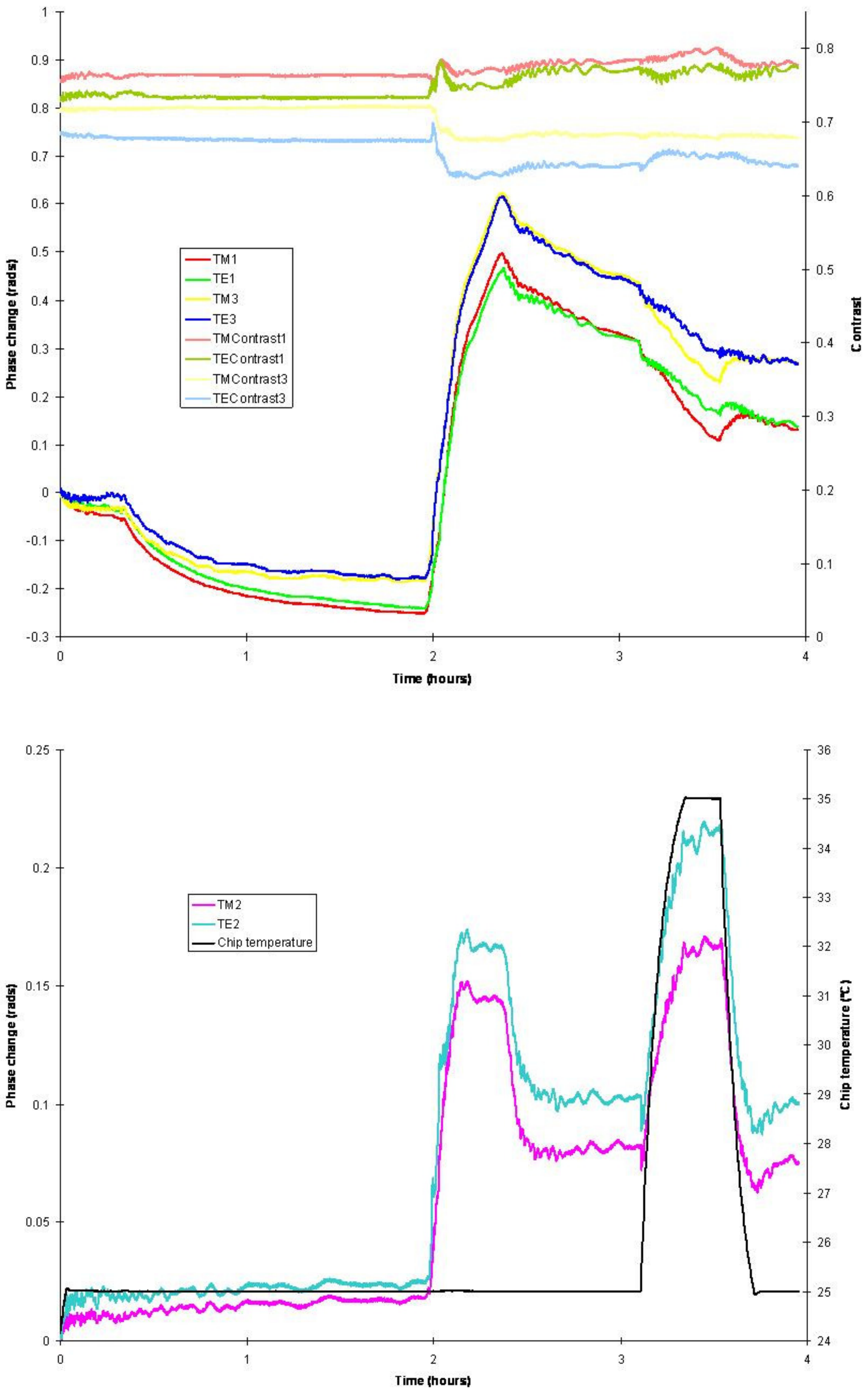

Figure 4.8 – Reference test associated to LC experiment on nitrogen dried surface.

Chapter 5. Analysis and discussion

5.1. Nitrogen drying the chip surface

Let's remember that drying the surface consisted in turning the nitrogen flow on at about 100±5 sccm in the setup (oven at ambient temperature, chip stabilized to 25 °C ± 1.5 mK). **Table 5.1** summarizes the phase changes caused by each drying process shown in **Section 4** for both channels and polarizations. A phase change corresponds to the phase difference between when the nitrogen flow is started and when the next operation is performed (changing the chip temperature, turning on the heater, or removing the oven for instance). The duration between these times varied according to the test.

	Figure 4.1	**Figure 4.2**	**Figure 4.3**	**Figure 4.6**	**Figure 4.8**
Duration	62 min	103 min	60 min	93 min	97 min
ΔΦE1	94 mrad	**210 mrad**	129 mrad	131 mrad	204 mrad
ΔΦM1	81 mrad	**194 mrad**	120 mrad	101 mrad	197 mrad
ΔΦE3	124 mrad	151 mrad	104 mrad	182 mrad	171 mrad
ΔΦM3	113 mrad	127 mrad	107 mrad	170 mrad	151 mrad

Table 5.1 – Duration and phase changes recorded for all drying processes performed in this study (channels 1 and 3 – polarizations TE and TM). Each column corresponds to an experiment depicted on the figure indicated in the first row.

The main observation in those tests is that most of the time the TE phase changes are higher than the TM phase changes (except for **Figure 4.3 channel 3**). A closer look at channel 2 phases for each test shows that the phase difference between TM2 and TE2 slightly increases during the drying process (TM2 staying most of the time above TE2 as it can be noticed on **Figure 5.1** which corresponds to the test described **Section 4.1.1**). Once again we notice that thermo-optic effects play an important role: a difference of temperature between the nitrogen flow and the chip must be mainly responsible for the observed difference between TE and TM curves. Finally channels 1 and 3 are not always affected in the same way by the drying process (neither it is the case for other kind of tests performed in this study). That must be due to shortcomings of both the vapour deposition setup and the AnaLight Quantum: the nitrogen flow might be distributed over the chip in an odd way, or the temperature control system might control the chip temperature better in one side compared to the other for instance.

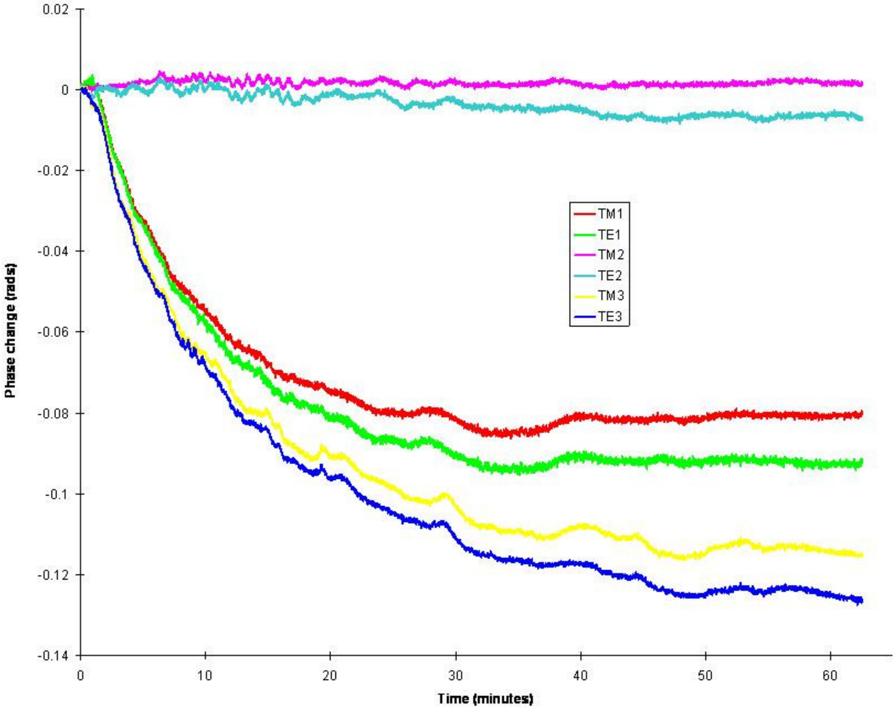

Figure 5.1 – Comparison between channel 2 phase changes and other channels phase changes for the test described in **Section 4.1.1**, showing that some thermo-optic effects take place.

Let's restrict our study to the 3 tests whose drying processes last between 90 min and 105 min (see **Table 5.1**) since a longer drying process gets closer to the equilibrium. Among those tests it is likely that the one depicted in **Figure 4.6** is less reliable as a blockage of the flow happened during the drying process. Therefore, the two remaining tests (**Figure 4.2 and 4.8**) are assumed to be the most representative of a typical drying process using our setup. They are both quite similar, therefore let's analyse one of them (**Figure 4.2 channel 1** for example) with the 1D mode solver Slab.

Assuming that the RH is about 50% in our system before starting drying the surface (we could not measure it, but this is a reasonable value at ambient temperature [25]), the water layers thickness must be about 10 Å (full coverage - several layers) if we base on Asay's work (from **Figure 2.13**). Slab gives us the TE and TM upper effective indexes corresponding to the chip structure with such a layer of water on it (assuming a RI of 1.31 since it is supposed to have an ice-like structure): $N_{TE\_before\_drying}$ = 1.5027400194 and $N_{TM\_before\_drying}$ = 1.5011440398. From that we can get the upper effective indexes corresponding to our experimental TE and TM phase changes (210 and 194 mrad) using another version of **Equation 3.1**:

$$N_{after\_drying} = -\frac{\Delta\varphi}{k_o \cdot l} + N_{before\_drying} \tag{5.1}$$

That is to say, $N_{TE\_after\_drying}$ = 1.5027387168 and $N_{TM\_after\_drying}$ = 1.5011426298.

Applying the method described in **Section 3.4.1** (for each polarization, the thickness is varied until matching the desired effective index) we found t_{TE} = 9 Å and t_{TM} = 9.2 Å. That corresponds to an average thickness of 9.07 Å, meaning that after drying the surface the thickness of the water layer is supposed to have decreased by less than 1 Å. Assuming that a monolayer thickness is about 2.7 Å [27], the drying process must only remove randomly some water molecules from the surface, but apparently not enough to remove a full monolayer. The amount of adsorbed water removed from the surface during our drying process is only about 9.3%. Therefore, we conclude that the drying process is not really effective probably because of the simplicity of our setup and protocol. An improved setup and protocol would be necessary to be able to remove the first 3-4 monolayers of water which are supposed to be strongly bounded with hydroxyl groups.

Since we couldn't calibrate the chip in this study (because some basic parameters about the chip we used were missing), we also performed the same calculation varying optogeometrical parameters of the upper waveguide. We guessed that the irradiation process which made our ultra-flat chip may have modified the upper waveguide thickness mainly (leaving its RI within usual fabrication tolerances, 1.52±0.005). Therefore the upper waveguide thickness has been varied within 1000±100 nm (which is much more than usual fabrication tolerances, 1000±50 nm). Using the same assumptions and calculation method, we found that between 7.3% and 12.3% of the adsorbed water layer is removed (these values correspond to the extreme parameters (1.525, 900 nm) and (1.515, 1100 nm) respectively). Note that other extreme parameters (1.525, 1100 nm) and (1.515, 900 nm) led to 11.3% and 8.3% respectively. Therefore even when extreme values of the upper waveguide optogeometrical parameters are used, the conclusion remains the same: only about 10% of the adsorbed water layers is removed from the surface.

In the case where the drying process is not only performed using the nitrogen flow but also by increasing the chip temperature (**Figure 4.1**), the thermo-optic effect caused by the increase of temperature may make the channel 3 phase decrease less than it should. Indeed, we have concluded before that the evolution of the phase difference between TE and TM on channel 2 was mainly responsible for the differences observed between TE and TM on channel 1 and 3. The average phase changes occurring on channel 2 when the chip temperature changes (average between the change from 25 °C to 35 °C and from 35 °C to 25 °C) has been reported in **Table 5.2**. We find from these values that a typical change of the channel 2 phase when the chip temperature changes between 25 °C and 35 °C is 126 mrad for TE and 98 mrad for TM. Therefore in the case this thermo-optic effect would happen exactly in the same way on channel 3 (that must not be so far from the truth), we could expect a total phase change of 369 mrad for TE and 380 mrad for TM (since the phase changes caused by the whole drying process, nitrogen flow followed by temperature change, are 243 mrad for TE and 282 mrad for TM). This couple of phase changes would lead to an average final thickness of 8.23 Å for water layers, which would still correspond to less than one layer of water removed. Therefore using the chip temperature parameter is still not enough to desorb an appreciable amount of water.

	Figure 4.1	**Figure 4.5**	**Figure 4.6**	**Figure 4.7**	**Figure 4.8**
ΔΦE2	150 mrad	100 mrad	130 mrad	130 mrad	120 mrad
ΔΦM2	120 mrad	90 mrad	90 mrad	100 mrad	90 mrad

Table 5.2 – Average channel 2 phase changes caused by changing the chip temperature between 25 °C and 35 °C, for all the concerned tests performed in this study (and for both polarizations).

5.2. Adsorbed water layers

We have seen just before that the nitrogen flow didn't change so much the thickness of adsorbed water layers. If we consider now the re-adsorption of water at ambient RH (**Figure 4.2**), we can see that the phase increases are about the same order of phase decreases of the drying stage. Indeed the re-adsorption of water corresponds again to less than one layer of water overnight. Therefore it has been decided to perform only a qualitative analogy between this test and a reference test on dried surface depicted in **Figure 4.8**.

Those tests have been compared (**Figure 5.2**) as they show similar phase changes during the drying process. Let's remember that at the end of the reference test (about 4 hours), the oven is still in place with chip temperature stabilized to 25 °C, oven temperature come back to ambient temperature, and nitrogen flow off (the chip is opened to the ambient air via the 2 Tufnol manifold outlets only). At that moment on the water test, the oven was removed from the top of the manifold, therefore the chip was opened to the ambient air via both the inlet and outlets of the manifold. In that way, the reference and water test are not really comparable, but this issue is overcome if we just suppose that the re-adsorbed water layer would only take longer to build up if the oven had not been removed from the top. Observing both tests, it looks like that channel 1 curve on the reference test would converge with channel 1 curve on the water test if we waited long enough (same thing for channel 3). That would be reasonable since both tests are supposed to reach an equilibrium which corresponds to a certain amount of water molecules adsorbed on the chip surface (at ambient RH). This qualitative reasoning can be considered as another argument to be able to say that phase increases observed in reference tests are mainly due to water molecules in the system.

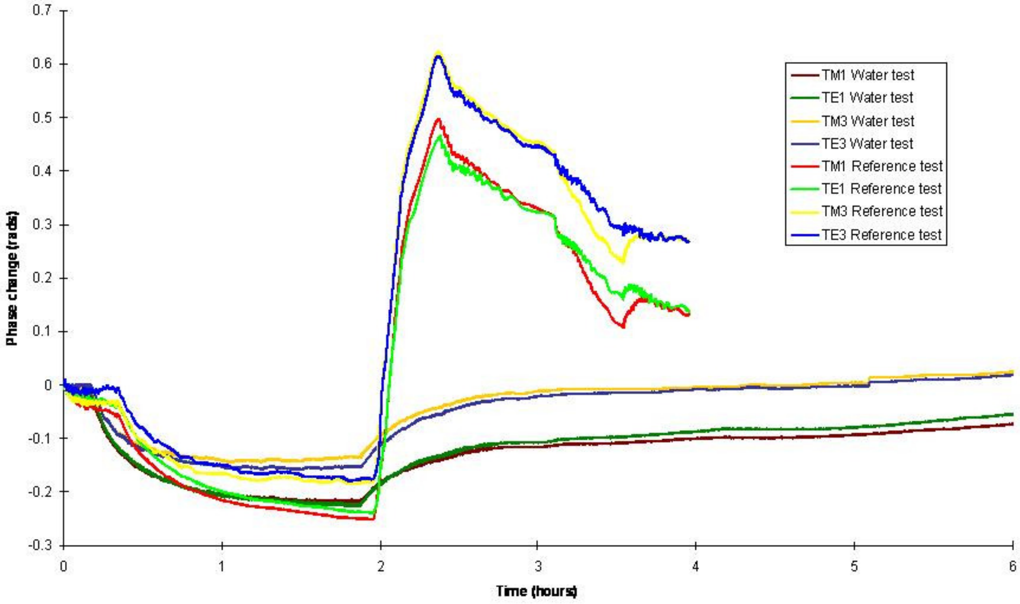

Figure 5.2 – Comparison between the reference test associated to LC experiment on nitrogen dried surface (**Figure 4.8**) and the water test for the chip exposed to ambient RH (**Figure 4.2**).

Figure 5.3 shows the sudden phase increases and contrast drops which occurred on the high RH experiment (due to condensation on the surface – **Figure 4.3**). We observe that the phase starts to increase (event A) before the contrast starts dropping sharply (event B). We used Slab with the following layer modeling based on Asay's work again (**Figure 2.13**): at the point where the drying process starts, a water layers thickness of 10 Å with RI of 1.31 is assumed (ice-like layers completely built), additional adsorbed layers on that are supposed to exhibit a liquid structure (RI of 1.33). **Table 5.3** shows the experimental phase changes at both events A and B for each channel (in reference to the phase where the drying process starts), and the calculated average thickness of liquid water layers built on the ice-like structure. We see that between 1 and 2 layers of liquid water have been adsorbed when the phases start increasing (event A), and about 3 layers have been adsorbed when contrasts start dropping (event B). That shows a growth similar to that found in Asay's work (**Figure 2.13**), and we can suppose that the micro-droplets start to form on the chip just after the transitional region A-B (the contrast starts dropping, meaning that light begins to be scattered at the waveguide surface).

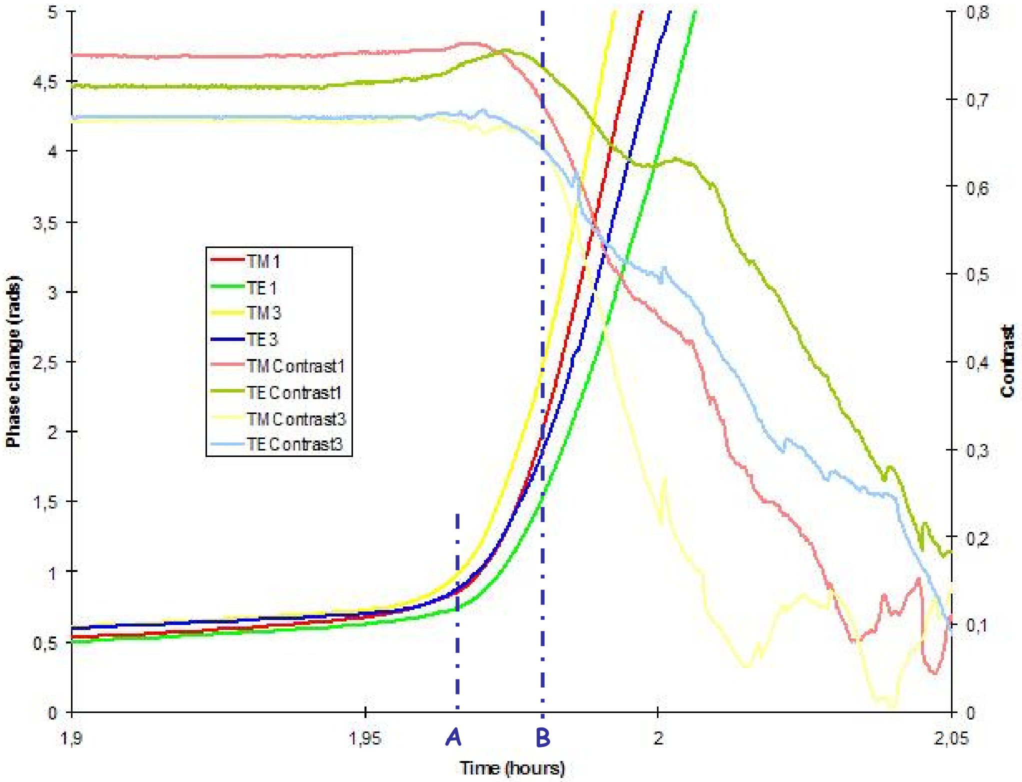

Figure 5.3 – Sudden phases increase (event A) and contrasts drop (event B) observed for the water test in high RH (**Section 4.1.2.2**).

	Sudden phases increase (A)			**Contrasts drop (B)**		
	ΔΦM	**ΔΦE**	**$t_{average}$**	**ΔΦM**	**ΔΦE**	**$t_{average}$**
Chan. 1	853 mrad	725 mrad	3.4 Å	1982 mrad	1501 mrad	7.27 Å
Chan. 3	1021 mrad	859 mrad	4 Å	2446 mrad	1833 mrad	8.93 Å

Table 5.3 – Values of experimental phase changes (in reference to the phase where the drying process started) and calculated average liquid water layer thicknesses, for each event and each channel.

5.3. Vapour deposition of 5CB molecules

5.3.1. Dry versus wet surface

As explained in **Section 2.3.3**, the phase change ratio method developed by Tan allows us to investigate the self-organization of LC molecules during the deposition. We studied channel 3 phase changes for each test (dry and wet surface, **Figure 5.4**), the start point being when the heater was set to 110 °C (the flow was already on for the dry test, whereas it had to be turned on for the wet test), and the end point being when both the heater and the flow were turned off. The ratio between TE and TM phase changes has been plotted against the TE phase change which is representative of the amount of molecules deposited, and TE and TM contrasts have been integrated into the chart as they are an indication of the homogeneity of the layer deposited.

A first look shows that both tests exhibit the same shape except for small phase changes (below 1.2 rad). Indeed, below 1.2 rad the ratio of the dry surface test tend to increase from low values up to 1 whereas the ratio of the wet surface test tend to do the opposite (decreasing from higher values down to 1). After that point, both ratios tend to decrease following the same shape (which will be detailed in **Section 5.3.2**). We can't give too much credit to the difference observed for small phase changes as Tan's model is not applicable for dilute layers which is assumed to be the case below 1.2 rad [32]. Therefore, we can say that there are no major differences between deposition on wet and dry surface. We notice that the homogeneity looks better preserved for the dry surface test as its contrast starts dropping after a bigger amount of molecules adsorbed on the surface (about 10.5 rad compared to about 8.5 rad for the wet surface test). However, it is probably not related to the dryness of the surface, especially because the initial values of contrasts are quite different according to the test.

We found previously that only a little amount of water molecules are desorbed during the drying process (about 10% of adsorbed water), that is in good agreement with the fact there are no big differences between tests on dry and on wet surface. However, it would be interesting to investigate properly the effect of water on the deposition as it has been reported that the water layer formed on a surface can screen the real surface potential (ability to attract molecules) of a sample [19]. Such a study would require a much more complicated setup allowing the surface to remain as much free of water molecules as possible. However we can still propose that the water layer naturally present on the surface might not affect the deposition of LC on the hydrophilic surface too much. The reason is that the dipole moment of LC (~6 D for nCB [31]) is much higher than that of water molecules (1.85 D), therefore LC molecules adsorbing on the surface might displace some water molecules which are eventually blown out of the system by the nitrogen flow. With this assumption we can also propose that the water causing phase changes during the reference tests doesn't disturb LC deposition so much, simply because interactions might occur mainly between hydrophilic surface and LC molecules.

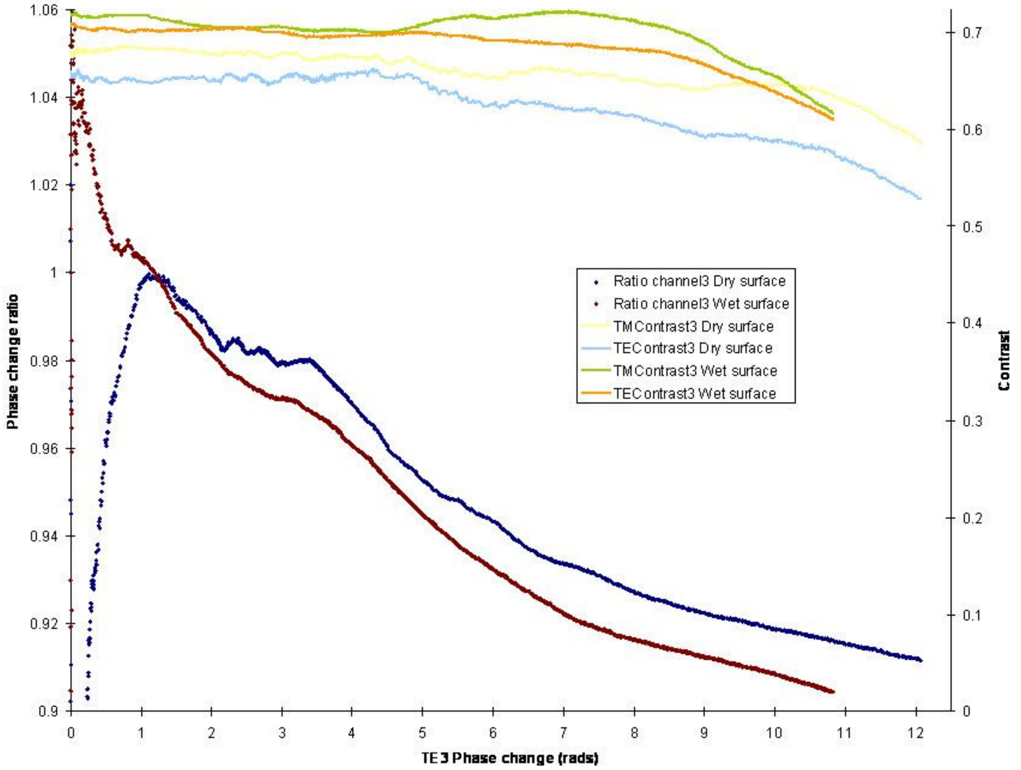

Figure 5.4 – Phase change ratios for LC deposition on dry and wet surface, with associated TE and TM contrasts.

5.3.2. Self-organization of 5CB molecules

We chose to analyse the LC deposition performed after drying the surface using the phase change ratio method from Tan's model. **Figure 5.5** represents both channel 3 and channel 2 phase change ratios ($\Delta\Phi_{E3}/\Delta\Phi_{M3}$ and $\Delta\Phi_{E2}/\Delta\Phi_{M2}$ respectively) against $\Delta\Phi_{E3}$. Channel 3 ratio exhibits a similar shape as that observed in Tan's study (**Section 2.3.3**). Basically, the ratio increases up to a maximum around 1.2 rad, and decreases afterwards. The important thing to notice is that the decrease is quite sharp at the beginning (with an oscillating step between 2.1 and 3.6 rad though) and slows down at the end. This oscillating step is assumed to be an anomaly, as it is also observed on channel 2 curve where it clearly disrupts the apparent periodicity of the curve. It is likely that this anomaly arises from a thermal effect on the chip which must be due to the non-linear evolution of the oven temperature before it reaches 110 °C. Consequently, we can draw two sets of asymptotes on the channel 3 ratio depending on whether we ignore the supposed anomaly or not (red asymptotes or green asymptotes respectively). Note that we haven't plotted the error of the ratio calculated from the following formula since it is too small ($\sim\pm10^{-4}$):

$$dr = \left.\frac{\partial r}{\partial \Delta\varphi_E}\right|_{\Delta\varphi_M} d\Delta\varphi_E + \left.\frac{\partial r}{\partial \Delta\varphi_M}\right|_{\Delta\varphi_E} d\Delta\varphi_M = \frac{d\Delta\varphi_E - r\cdot d\Delta\varphi_M}{\Delta\varphi_M} \tag{5.2}$$

where $d\Delta\varphi_E$ and $d\Delta\varphi_M$ are the TE and TM standard deviations of the TE and TM phases calculated by the software.

As already mentioned, we cannot rely on the first part of the chart as the layer deposited must not be dense enough so that the model can apply (it is already assumed that bulk RIs are applicable to a dense ultra-thin adlayer, but that can't be assumed for a dilute ultra-thin adlayer). The model is assumed to be reliable from the point where the ratio starts to decrease, (1.2 rad, 0.999). However, at that point the model is still not applicable as no ratio value of the polar angle θ corresponds to this ratio value (**Figure 3.11**). That is due to the fact that the reality of our experiment is much more complex than the model we used. Moreover the input parameters we used were maybe too far from the reality (particularly optogeometrical parameters of the chip which could be very different from the theoretical ones). In any case, it is likely that such a high ratio still corresponds to angles close to 90°, meaning that the molecules probably lay on the surface first before progressively standing up when the layer densifies (as briefly described in **Section 2.3.3**).

Contrary to Tan's result (**Figure 2.19**), we don't see a clear point where the ratio becomes constant (meaning that the first monolayer is deposited, and keeps stable), we just observe that the decrease slows down. The process of molecules standing up slows down probably because some molecules are starting to form a second layer which weighs on the first layer. We can still estimate the properties of a "virtual" monolayer in our experiment by looking at where the asymptotes cross. This will be done only for the red asymptotes (real curve), as it would cause some issues to evaluate the TE and TM phase changes at the point where the green asymptotes cross. The virtual monolayer can be considered to be completed when 6.1 rad of 5CB molecules are deposited on the surface. At that point the ratio on the curve is 0.942, which corresponds on **Figure 3.11** to a polar angle of 56.5°. The TE and TM phase changes associated to this data point (6.1 rad and 6.48 rad) allow us to calculate an average thickness for this layer using method described in **Section 3.4.1** and assuming that no water layers are on the chip surface before LC deposition, as if they already had been displaced by LC molecules. We found 1.44 nm, which is quite close to the value found with the geometrical model, 1.27nm (see **Section 3.4.2**, **Figure 3.13**).

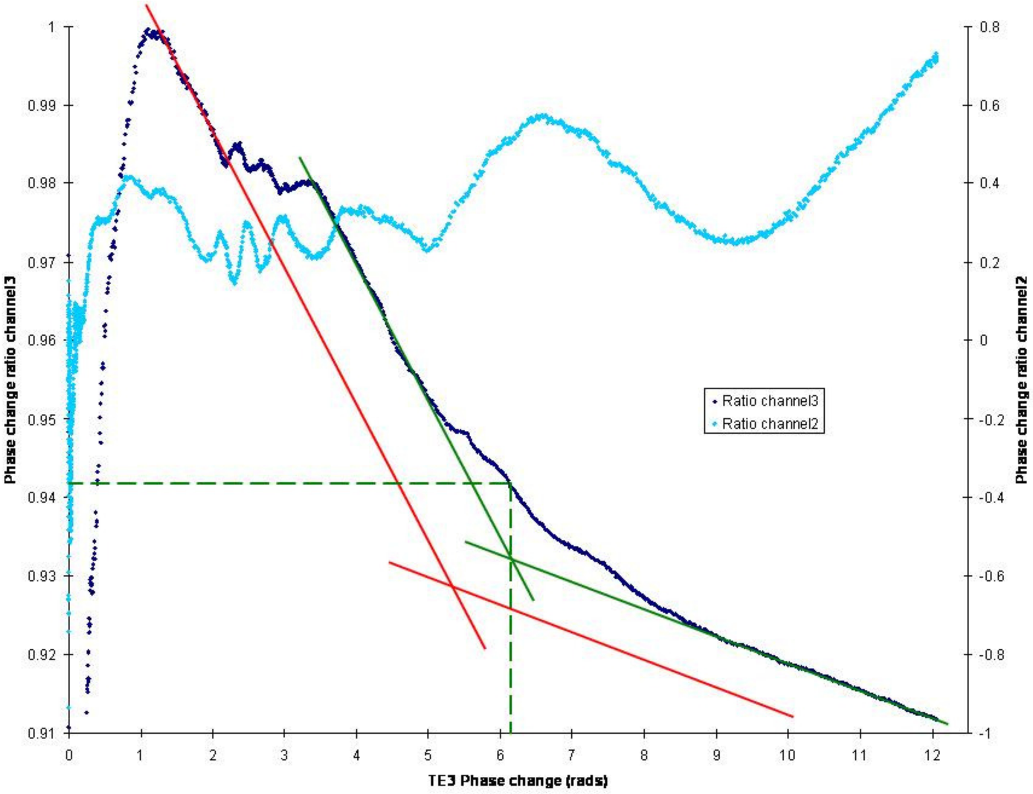

Figure 5.5 – Phase change ratios for both channel 2 and 3 of LC deposition on dry surface, with sets of asymptotes allowing quantitative data to be determined.

As a conclusion, we used the previous study [14] to guess what happened in our experiments. However, the ratio evolution in that previous study was clearly more accurate, assuming that the result shown in the publication could be obtained with a good reproducibility. This observation is quite surprising since the setup we used was supposed to be more reliable: measured nitrogen flow compared to airflow roughly controlled with a valve, system not opened to the environment (except via outlets), manifold allowing more homogeneous deposition, etc. Therefore, the differences might arise from the measurement setup itself. We notice that thermo-optic effects are quite important in our study. It is therefore likely that the old setup had a much better temperature control capable of balancing the external thermal perturbations very effectively, even though it was less precise (±10 mK written in the paper [32], ±4 mK observed in the old result in fact) than our setup (±1.5 mK). That would not be surprising since the temperature control of the AnaLight Quantum had several technical problems at the beginning of the study. In any case, the conclusions we reached are in good agreement with the previous study in terms of polar angle and thickness of the virtual monolayer deposited.

5.4. Desorption of 5CB molecules

We plotted the birefringence against time for LC desorption with both tools described in **Section 3.4** (Tan's Mathcad program and Farfield AnaLight Explorer software). **Figure 5.6** corresponds to channel 3 of LC deposition on dry surface from the point where both the heater and the flow have been stopped until the end of the experiment. We can see that the birefringence decreases slowly, except when the temperature is increased to 35 °C. At that point the curve exhibits a shape which can be split into two different effects (as drawn on the schematic of **Figure 5.7**): an acceleration of the decreasing behaviour of the birefringence on the one hand, and a step toward lower birefringence values on the other hand. Note that the birefringence calculated with the AnaLight Explorer software has a similar shape to that of the birefringence calculated with Tan's Mathcad program, but surprisingly compressed over a smaller range of values.

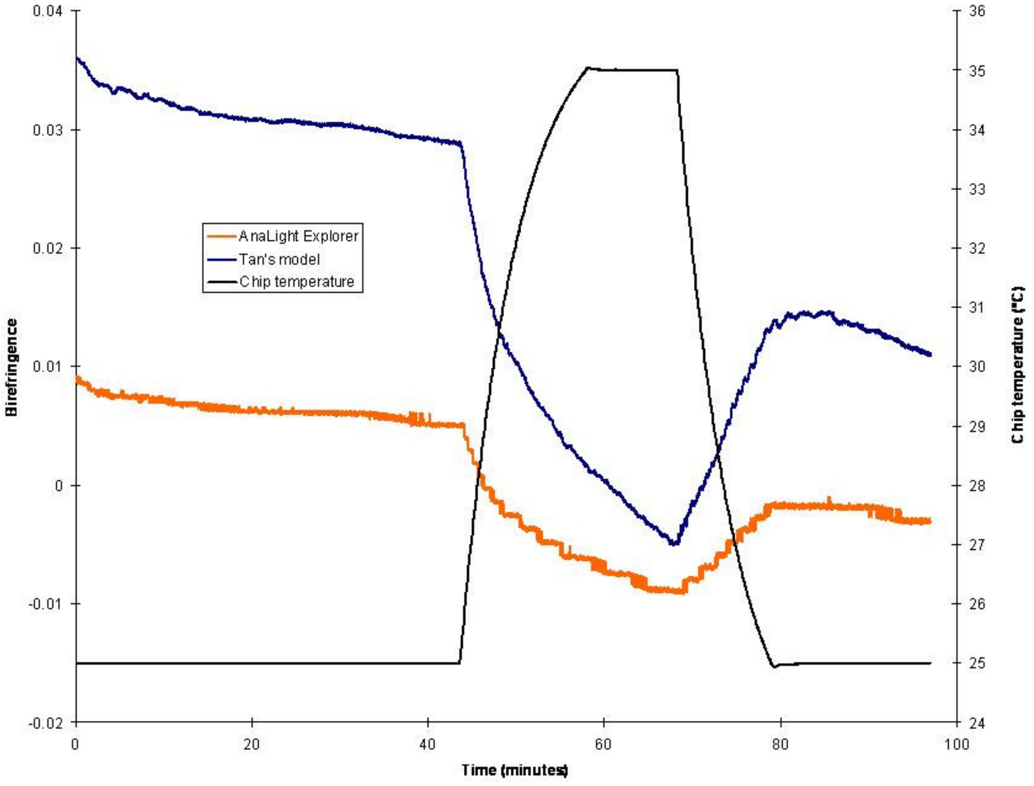

Figure 5.6 – Desorption of LC molecules exhibiting a special behaviour when the chip temperature is increased (calculation with 2 different methods).

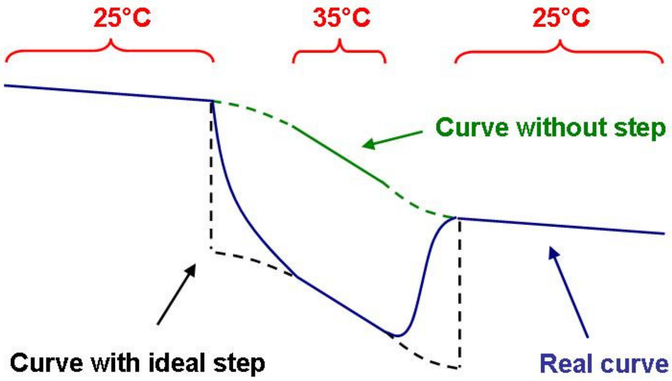

Figure 5.7 – Model for the birefringence evolution when the chip temperature changes between 25 °C and 35 °C.

The slow decrease of the birefringence after turning the heater and the flow off shows that the polar angle of the layers does not increase too much (see **Figure 3.11**). It is likely that the structure of the layers remains pretty much the same since molecules slowly desorb from the surface. Increasing the temperature causes an acceleration of this decrease. Indeed, as the temperature increases, more and more LC molecules desorb from the surface, that increases the space available between remaining molecules, so the layer tend to flatten more rapidly (the polar angle θ increases more) via energy minimization. Note that after coming back to 25 °C the rate of flattening is slightly different from initially, but we don't have any explanation for that yet.

However, some issues arise for explaining the step on the birefringence. Coming back to the monolayer model described in **Section 2.3.2**, we can see that the measured birefringence depends not only on the polar angle θ but also on the RIs n_o et n_e (which were supposed constant for calculations shown in **Section 3.4.2**). Let's remember that n_o - n_e is the so-called intrinsic birefringence, that we can define as Δn_0. We know from the literature [45] (**Figure 5.8**) that the intrinsic birefringence of bulk 5CB depends on the temperature: it decreases down to 0 when the temperature reaches 35 °C (clearing point of 5CB, where the mesophase becomes isotropic). From **Equation 2.6 – Section 2.3.2** we find that:

$$\Delta n \equiv \Delta n_0 \cdot (1 - \frac{3}{2}\sin^2\theta) \tag{5.3}$$

Since 5CB molecules anchored on the surface are supposed to be at 35 °C, the intrinsic birefringence Δn_0 should become 0 as well as the measured birefringence Δn, and remain 0 as long as 35 °C is maintained. However, none of the charts exhibit such a behaviour. That must mean that we have not reached the clearing point yet. In fact, it is likely that the clearing point of anchored LC layers on hydrophilic surfaces is much higher than that of LC molecules in their bulk phase since the anchoring effect maintains a certain anisotropy along the layers. Moreover, we think it is not reasonable to rely too much on the birefringence values since the calculations are based on approximated input data (for instance we used the theoretical optogeometrical parameters of our chip) and on assumptions (for instance the RIs used for anchored LC layers were bulk values).

Consequently, we propose that the step of the birefringence does not show the transition liquid crystalline-isotropic phase, but only shows a modification of the intrinsic birefringence which would probably lead to a phase transition of LC molecules if we could reach higher temperatures (but the temperature control can hardly reach 40 °C unfortunately).

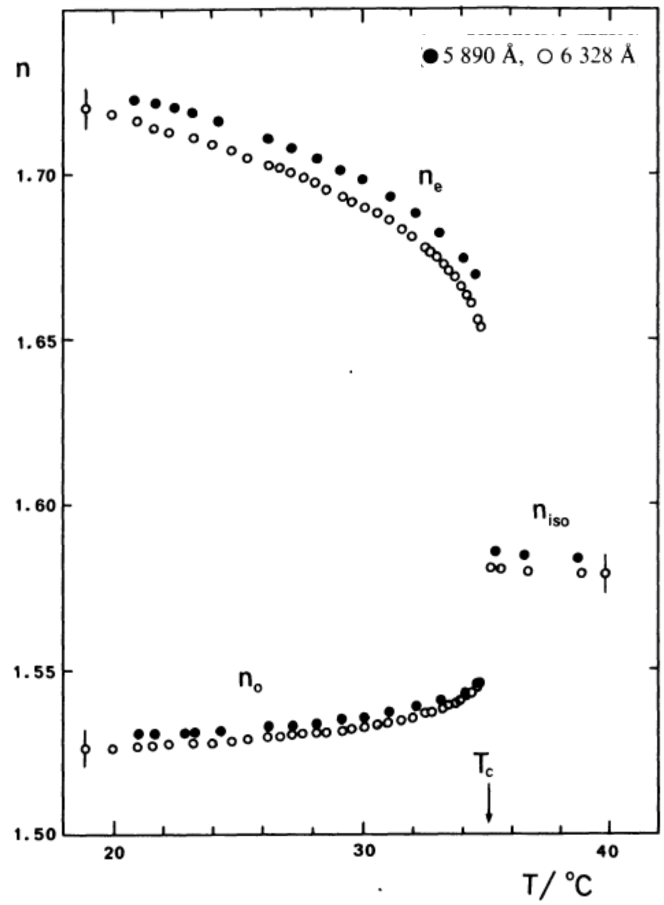

Figure 5.8 – RIs of 5CB as a function of temperature (2 sets according to the wavelength). T_c is the clearing temperature [45].

5.5. About the present study

Setting up a new instrument in order to get new results about self-organization of 5CB monolayers required us to perform a lot of preliminary tests. We focused on improving both the setup and the protocol step by step until reaching an optimal configuration. First of all we performed tests with the old vapour deposition setup adapted to the AnaLight Quantum, that allowed us to design a new vapour deposition setup after finding the supposed weaknesses of the old one. Then we performed many times the same kind of test (varying one experimental parameter after each other) hoping to find some general trends within the results (based on our knowledge of previous results obtained by Tan). Unfortunately we only observed a large range of different results, but that helped us to identify the key parameters which played an important role in the experience. We found for instance that using the ultra-flat chip instead of a normal INEX chip increased the reproducibility of the results, that is why we decided to use only that chip for the results presented in this study (even though that didn't optimize the reliability of the analysis since we didn't have enough data about that chip to calibrate it). We also found out that the most important issue was to perform strictly the same preparation protocol (chip cleaning, and vapour deposition setup cleaning). That is why we decided to perform a batch of tests with a lot of strictness in the preparation protocol, and to base the whole analysis on those results (presented in **Section 4**) using also the experience acquired during the preliminary tests stage.

However, some additional steps would have been required to make this study more reliable. First of all it would have been useful to perform additional cleaning of the chip using an O_2 plasma, that would have ensured contact angles <5° [32]. We could also have performed contact angle measurements in order to make sure that our protocol always gave the same degree of hydrophilicity. Another important step would have been to integrate a RH sensor in our vapour deposition setup in order to measure properly the RH in the system (especially in the vicinity of the chip) since that parameter played an important role in this study. Moreover, it could have been interesting to perform exactly the same batch of experiments but using a normal INEX chip (not the ultra-flat one). In this case we would have had proper fabrication tolerances data, and therefore we could have calibrated it in order to use more reliable input data for our calculations. Finally, ideally it would have been interesting to perform several times each experiment exposed in this study, to make sure that the batch of tests we performed had a good reproducibility. All these ideas have not been performed mainly because of a lack of time.

Even though a lot of care has been taken to perform the experiments, several weaknesses of the setup decreased the reliability of the results. A lot of issues come from the fact that the temperature control system of the AnaLight Quantum is not fast enough to compensate instantaneously the external thermal perturbations. For that reason the hot nitrogen flow on the chip always caused unsteady phase changes on channel 2 (see **Figure 4.5 to 4.8**) and variations of the chip temperature (see **Figure 4.3 and 4.7**). It was hard to decorrelate the thermo-optic effects from the adsorption effects on channels 1 and 3. Since we couldn't control adsorption properly with our setup (reference tests always involved water adsorption for instance) the only way was to observe the reference channel (channel 2) and suppose that the same phase changes applied on the other channels. Note that a special gasket was used to expose the reference channel to its environment since the usual gasket used to cover it. Fortunately for both LC tests and reference tests the thermo-optic effects can be considered as negligible. Indeed the phase changes caused by the hot nitrogen flow on channel 2 were never larger than 14 mrad over the deposition, observing both reference tests and LC tests, that is quite small compared to 650 mrad and 8.5 rad (minimum deposited for reference tests and LC tests respectively). Note that another weakness of the temperature control (but less important) was the anomalies on the chip temperature curves which sometimes happened during experiments (see **Figure 4.3 and 4.7**). Finally, we noticed several random behaviours during experiments : evolution of the phases after the beginning of experiment (rarely constant), non–linear increase of the temperature of the oven, different channel 1 and 3 responses, etc.

We will finish this section raising another issue for which we haven't found any solution so far. It has already been mentioned briefly in **Section 5.4** that the birefringence calculated with the AnaLight Explorer software had a similar shape to that of the birefringence calculated with Tan's Mathcad program, but compressed over a smaller range of values. We plotted in **Figure 5.9** the same comparison but for the 5CB deposition we analysed in **Section 5.3.2**, that shows with no surprise that the curves are not superimposed. Note that the orange curve is similar to the curves depicted in **Figure 3.14**. This issue will have to be investigated later as it certainly points out a problem in either the model developed by Tan, or in the method used in Farfield AnaLight Explorer software. In fact the difference might arise from the fact that the AnaLight Explorer software is usually used for lower birefringence layers (like lipid bilayers, ~0.02). Therefore Tan's model might be more adapted for investigating higher birefringence layers (like LC layers, ~0.2).

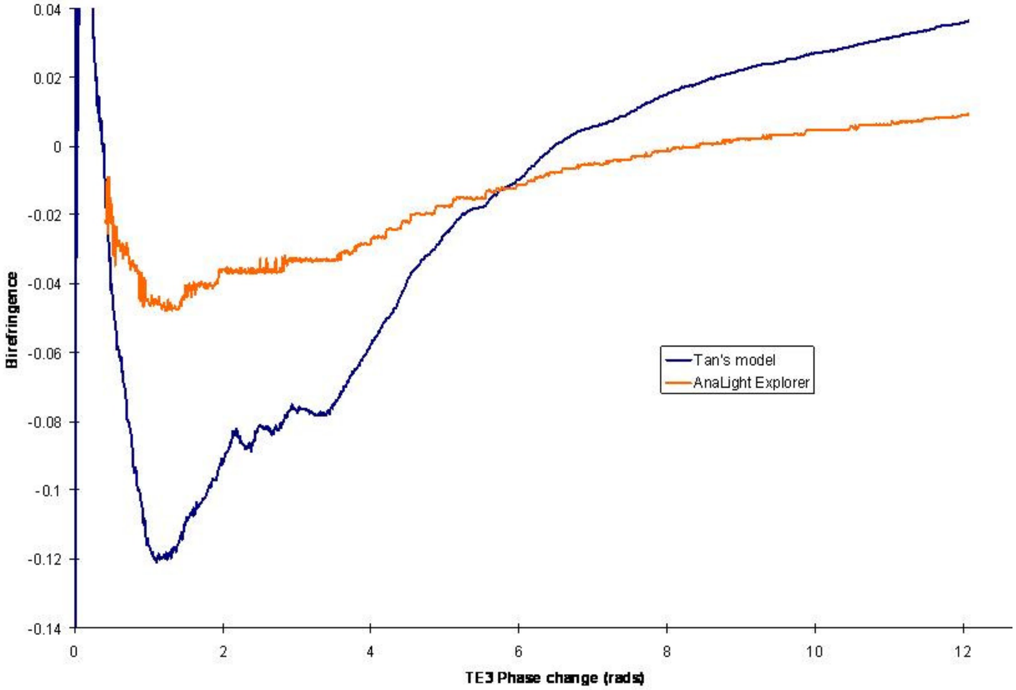

Figure 5.9 – Comparison of the birefringence of the 5CB deposition analysed in Section 5.3.2 with 2 different tools.

Chapter 6. Conclusions and outlook

6.1. Summary

First of all, a new setup with improved protocol has been found in order to get new results about the self-organization of 5CB molecules vapour deposited onto a hydrophilic silicon oxynitride surface. We focused on using a proper system (controlled nitrogen flow, isolated inner environment, and manifold allowing more homogeneous layers to be deposited), as well as a strict protocol (chip cleaning, and preparation protocol). The new results are in good agreement with the previous study in terms of thickness and average molecular orientation of the monolayer (1.44 nm and 56.5° respectively), although they are clearly less accurate (monolayer completion less clear than in the previous study for instance). Our investigation of the desorption of 5CB molecules with temperature shows that even though the clearing temperature was reached (35 °C) no signs of phase transition have been observed.

Besides that, the study of the influence of water layers during deposition of liquid crystals which arose during our investigations didn't give conclusions. Indeed we found that our setup was too simple to remove an amount of water molecules reasonable enough (only about 10% of adsorbed water layers) to be able to perform a comparison with the case where the surface is not dried. This must be due to the fact that the first adsorbed water layers have an ice-like structure strongly hold by the hydrophilic surface, therefore an improved setup with vacuum system as well as other stages in the cleaning protocol of the chip would be required to remove them. Note that our setup nevertheless allowed us to observe condensation of water on the chip surrounded by a high RH environment.

This work was the occasion of getting performance data about the AnaLight Quantum and the new ultra-flat chip prototype for the Farfield group. The main conclusion is that the thermal design of this low-cost instrument is not good enough for our experiments. Indeed, the temperature control has been found not to be fast enough to compensate external thermal perturbations (hot nitrogen flow over the chip for instance). That made the analysis harder in so far as thermo-optic effects were mixed with adsorption effects within the results. About the ultra-flat chip we found that this chip improved the reproducibility of our experiments, although it decreased the reliability of analysis because of the lack of fabrication data.

6.2. Further work

Our investigation showed the importance of adsorbed water layers during vapour deposition of molecules onto a hydrophilic surface. Consequently it would be useful to improve both the setup and the cleaning protocol in order to be able to perform an advanced study about adsorbed water layers. Moreover some interesting comparisons could be performed for any test: hydrophilic surface compared to hydrophobic surface (the hydrophobic surface can be prepared as explained in [37]), or ultra-flat chip compared to normal chip (since water layers depend a lot on the morphology of the surface [2]).

About the self-organization of LC molecules on a hydrophilic silicon oxynitride surface, additional experiments should be performed according to several parameters. The first parameter would be the kind of nCB put in the oven, it could be interesting to compare 5CB, 6CB, 7CB, 8CB,… The second parameter would be the temperature, the AnaLight Quantum should be pushed to 40 °C in order to determine whether or not we can see the liquid crystalline-isotropic transition at that temperature. The last parameter would be the speed of deposition, a comparison between deposition at a very slow flowrate (20 sccm for instance) and at the maximum flowrate (100 sccm) would certainly show interesting results.

In any case, the instrument must be improved for the next studies. The design of a beam expander was a first step (**Appendix C**), a mechanical mounting need now be made and the optical component must be tested on our setup. Also a chiller should be integrated into the instrument in order to dissipate all the heat created by the camera and the laser mainly. Unfortunately, it seems hard to improve the present temperature control, therefore a special attention will have to be paid to thermo-optic effects during experiments in the future (importance of channel 2 measurement).

Bibliography

[1] Freeman, N. J., G. H. Cross (28 May 1998). Int. patent no. 98/22807.

[2] Szori, M., P. Jedlovszky, et al. (2010). "Water adsorption on hydrophilic and hydrophobic self-assembled monolayers as proxies for atmospheric surfaces. A grand canonical Monte Carlo simulation study." Physical Chemistry Chemical Physics 12(18): 4604-4616.

[3] Aroutiounian, V. M., K. S. Martirosyan, et al. (2008). "Use of Porous Silicon for Double- and Triple-Layer Antireflection Coatings in Silicon Photovoltaic Converters." Journal of Contemporary Physics-Armenian Academy of Sciences 43(2): 72-76.

[4] Farfield Scientific Limited. "Basics of optical measurements using waveguides (Dual Polarisation Interferometry Part 1)." Technical Note 007. [www.farfield-group.com/pdfs/TechNote007v2.pdf – document accessed on the 21st of September 2010].

[5] Farfield Scientific Limited. "Basics of interferometry (Dual Polarisation Interferometry Part 2)." Technical Note 016. [www.farfield-group.com/pdfs/TechNote016v2.pdf – document accessed on the 21st of September 2010].

[6] Farfield Scientific Limited. "Basics of dual polarisation measurements (Dual Polarisation Interferometry Part 3)." Technical Note 017. [www.farfield-group.com/pdfs/TechNote017v2.pdf – document accessed on the 21st of September 2010].

[7] Farfield Scientific Limited. "The Maxwell equations (Dual Polarisation Interferometry Part 4)." Technical Note 018. [www.farfield-group.com/pdfs/TechNote018v1.pdf – document accessed on the 21st of September 2010].

[8] Mashaghi, A., M. Swann, et al. (2008). "Optical anisotropy of supported lipid structures probed by waveguide spectroscopy and its application to study of supported lipid bilayer formation kinetics." Analytical Chemistry 80(10): 3666-3676.

[9] Cross, G. H., A. A. Reeves, et al. (2003). "A new quantitative optical biosensor for protein characterisation." Biosensors & Bioelectronics 19(4): 383-390.

[10] Cross, G. H., A. Reeves, et al. (2004). "The metrics of surface adsorbed small molecules on the Young's fringe dual-slab waveguide interferometer." Journal of Physics D-Applied Physics 37(1): 74-80.

[11] Cross G. H., Freeman N. J., and Swann M. J. (2007). "Dual Polarization Interferometry: A Real-Time Optical Technique for Measuring (Bio)molecular Orientation, Structure and Function at the Solid/Liquid Interface." Handbook of Biosensors and Biochips. Wiley-Interscience.

[12] www.cvimellesgriot.com/Products/Documents/Catalog/LGX1_LHX1_LYX1.pdf [document accessed on the 21st of September 2010]. Product 25 LHP 991 (old product number, 05 LHP 991, not used anymore).

[13] Reeves A. (2004). “Theoretical studies of one-dimensional and two-dimensional photonic structures.” PhD Thesis, University of Durham.

[14] Tan, O. (2009). “Optical studies of ordered monomolecular layers: ab initio simulation and experiment.” PhD Thesis. University of Durham.

[15] Farfield Scientific Limited. “Linearisation of detector response on AnaLight instruments.” Technical Note 010. [www.farfield-group.com/pdfs/TechNote010v2.pdf – document accessed on the 21st of September 2010].

[16] Farfield Scientific Limited. “Short description of linearisation of AnaLight detector response.” Technical Note 021. [www.farfield-group.com/pdfs/TechNote021v2.pdf – document accessed on the 21st of September 2010].

[17] Farfield Scientific Limited. “Essential calibration procedures for AnaLight instruments.” Technical Note 001. [www.farfield-group.com/pdfs/TechNote001v2.pdf – document accessed on the 21st of September 2010].

[18] Swann, M. J., L. L. Peel, et al. (2004). "Dual-polarization interferometry: an analytical technique to measure changes in protein structure in real time, to determine the stoichiometry of binding events, and to differentiate between specific and nonspecific interactions." Analytical Biochemistry 329(2): 190-198.

[19] Hong, J., Y. Kim, et al. (2009). "The effect of nitrogen incorporation on surface properties of silicon oxynitride films." Physica Status Solidi-Rapid Research Letters 3(1): 25-27.

[20] Choo, S. J., B. C. Lee, et al. (2009). "Optimization of silicon oxynitrides by plasma-enhanced chemical vapor deposition for an interferometric biosensor." Journal of Micromechanics and Microengineering 19(9). 095007.

[21] Zwang, T. J., W. R. Fletcher, et al. (2010). "Quantification of the Layer of Hydration of a Supported Lipid Bilayer." Langmuir 26(7): 4598-4601.

[22] Papirer E.. (2000). “Adsorption on Silica Surfaces.” Surfactant science series. Volume 90. Marcel Dekker.

[23] Sneh, O. and S. M. George (1995). "Thermal-Stability of Hydroxyl-Groups on a Well-Defined Silica Surface." Journal of Physical Chemistry 99(13): 4639-4647.

[24] www.ramehart.com/contactangle.htm [document accessed on the 21st of September 2010].

[25] Collins, K. E., V. R. de Camargo, et al. (2005). "Physisorbed water layer formation on fully hydroxylated mesoporous silicas." Journal of Colloid and Interface Science 291(2): 353-360.

[26] Brovchenko I., A. Oleinikova. (2008). “Interfacial and confined water.” Elsevier.

[27] Asay, D. B. and S. H. Kim (2005). "Evolution of the adsorbed water layer structure on silicon oxide at room temperature." Journal of Physical Chemistry B 109(35): 16760-16763.

[28] Peng, C. S., S. X. Song, et al. (2006). "Study of hydration layers near a hydrophilic surface in water through AFM imaging." Surface and Interface Analysis 38(5): 975-980.

[29] Zheng, J. M., W. C. Chin, et al. (2006). "Surfaces and interfacial water: Evidence that hydrophilic surfaces have long-range impact." Advances in Colloid and Interface Science 127(1): 19-27.

[30] Vandenbrouck F. (2001). "Films minces de cristaux liquides." PhD Thesis. University of Paris VI.

[31] Olenik, I. D., K. Kocevar, et al. (2003). "Structure and polarity of 8CB films evaporated onto solid substrates." European Physical Journal E 11(2): 169-175.

[32] Tan, O. and G. H. Cross (2009). "Surface anchoring structure of a liquid crystal monolayer studied via dual polarization interferometry." Physical Review E 79(2). 021703.

[33] http://upload.wikimedia.org/wikipedia/commons/thumb/2/25/Nematic3d.png/180px-Nematic3d.png [document accessed on the 21st of September 2010].

[34] www.farfield-group.com/pdfs/AnaLight%20Quantum%20Detail.pdf [document accessed on the 21st of September 2010].

[35] Farfield Group Limited. (October 2007). "AnaLight Bio200 service manual v2.3 – Volume 3."

[36] Farfield Group Limited. (November 2007). "AnaLight Bio200 user manual v4.1 – Volume 1."

[37] Farfield Scientific Limited. "AnaChip cleaning and preparation of a hydrophobic surface." Technical Note 022. [www.farfield-group.com/pdfs/TechNote022v1.pdf – document accessed on the 21st of September 2010].

[38] http://en.wikipedia.org/wiki/Piranha_solution [document accessed on the 21st of September 2010].

[39] www.enma.umd.edu/LAMP/Sop/Piranha_SOP.htm [document accessed on the 21st of September 2010].

[40] www.nanofab.ubc.ca/process-piranha-etch [document accessed on the 21st of September 2010].

[41] Asay, D. B., A. L. Barnette, et al. (2009). "Effects of Surface Chemistry on Structure and Thermodynamics of Water Layers at Solid-Vapor Interfaces." Journal of Physical Chemistry C 113(6): 2128-2133.

[42] Ashley, K. M., J. C. Meredith, et al. (2003). "Combinatorial investigation of dewetting: polystyrene thin films on gradient hydrophilic surfaces." Polymer 44(3): 769-772.

[43] http://refractiveindex.info/ [document accessed on the 21st of September 2010].

[44] www.sigmaaldrich.com [document accessed on the 21st of September 2010]. Product 328510.

[45] Horn, R. G. (1978). "Refractive-Indexes and Order Parameters of 2 Liquid-Crystals." Journal De Physique 39(1): 105-109.

[46] www.winlens.de/fileadmin/user_upload/Dateien/Technical_papers/Optolines_bmx_englisch.pdf [document accessed on the 21st of September 2010].

[47] www.cvimellesgriot.com/Products/Documents/Catalog/RCC-C.pdf [document accessed on the 21st of September 2010].

[48] www.cvimellesgriot.com/Products/Documents/Catalog/SCX-C.pdf [document accessed on the 21st of September 2010].

Appendix A: Temporal phase measurement [14]

Based on the experimentally recorded fringe intensity by the CCD camera at each pixel (1024*1024), an analytical algorithm is used to determine both the phase and contrast of fringes. Let's first explain the temporal phase measurement method which enables phase and contrast determination from N intensity values considering the following fringe pattern (simple case):

$$I = I_1 + I_2 + 2\sqrt{I_1 I_2}\cos(\alpha + \phi) \tag{A.1}$$

where α is the spatial phase difference that can be known detecting position of the pixel, ϕ is the initial phase difference before any deposition, I_1 and I_2 are component beams intensities (here they can be simply seen as constants for the plane wave case, but this is not the case with our device since the wavefront is strongly modulated).

This can be rewritten as following:

$$I = I_0\left[1 + \gamma\cos(\alpha + \phi)\right] \tag{A.2}$$

with, $I_0 = I_1 + I_2$, and, $\gamma = \dfrac{2\sqrt{I_1 I_2}}{I_1 + I_2}$ (fringe contrast) (A.3)

For the N recorded intensity measurement, the intensity recorded at each pixel can be formulated as:

$$I_i = a_0 + a_1 \cos\alpha_i + a_2 \sin\alpha_i \tag{A.4}$$

where,

$$\begin{aligned} a_0 &= I_0 \\ a_1 &= I_0\gamma\cos\phi \\ a_2 &= -I_0\gamma\sin\phi \end{aligned} \tag{A.5}$$

The solution of a_0, a_1 and a_2 coefficients can be obtained from a least square matrix manipulation:

$$\begin{pmatrix} a_0 \\ a_1 \\ a_2 \end{pmatrix} = \begin{pmatrix} N & \sum \cos \alpha_i & \sum \sin \alpha_i \\ \sum \cos \alpha_i & \sum \cos^2 \alpha_i & \sum \cos \alpha_i \sin \alpha_i \\ \sum \sin \alpha_i & \sum \cos \alpha_i \sin \alpha_i & \sum \sin^2 \alpha_i \end{pmatrix}^{-1} \begin{pmatrix} \sum I_i \\ \sum I_i \cos \alpha_i \\ \sum I_i \sin \alpha_i \end{pmatrix} \tag{A.6}$$

The phase ϕ and contrast γ are therefore:

$$\phi = \arctan\left(-\frac{a_2}{a_1}\right) \quad \text{and} \quad \gamma = \frac{\sqrt{a_1{}^2 + a_2{}^2}}{a_0} \tag{A.7}$$

In general, the interference fringe with large diffraction envelope function is not suitable to use the temporal phase measurement straightforwardly to extract the phase information, since the algorithm requires a standard cosine interference pattern. In order to calculate the phase from a strongly modulated fringe pattern, a method can be to reduce it to standard cosine fringes (with different mathematical methods), and then to compute the phase from the temporal phase algorithm described above.

Appendix B: Phase change ratio [14]

Tan found a simple way for linking properties of the adlayer and experimental data using some assumptions. From **Equation 2.3 - Section 2.1.2.2** we get:

$$\phi_E = C_E + k_0 \int_0^l N_E(x)\,dx \quad \text{and} \quad \phi_M = C_M + k_0 \int_0^l N_M(x)\,dx \tag{B.1}$$

where k_0 is the free-space wave vector, C_E and C_M are constants comprising all the terms not affected by the deposition process on the surface, and $N_E(x)$ and $N_M(x)$ are respectively TE and TM effective indexes of upper guiding mode in the exposed region.

A layer-by-layer growth of liquid crystal molecules is not expected. Therefore, the problem that the sensing waveguide effective index is variable along the propagation direction x would be hard to resolve except if a linearity hypothesis is introduced (validity of assumption confirmed by the simulations). Let's assume the enlargement of the effective index ($N(x)$ - N^0) is proportional to the grown thickness of the adsorbed layer $d_m(x)$, hence we can write:

$$\begin{aligned} N_E(x) &= a d_m(x) + N_E{}^0 \\ N_M(x) &= b d_m(x) + N_M{}^0 \end{aligned} \tag{B.2}$$

where a and b are the so-called TE and TM perturbation rate to the waveguide effective index due to the existence of the adsorbed layers.

Therefore, from **Equations B.1 and B.2**, we get:

$$\begin{aligned} \phi_E &= C_E + k_0 N_E{}^0 l + k_0 a \int_0^l d_m(x)\,dx = \phi_E{}^0 + k_0 a \int_0^l d_m(x)\,dx \\ \phi_M &= C_M + k_0 N_M{}^0 l + k_0 b \int_0^l d_m(x)\,dx = \phi_M{}^0 + k_0 b \int_0^l d_m(x)\,dx \end{aligned} \tag{B.3}$$

where $\phi_E{}^0 \equiv C_E + k_0 N_E{}^0 l$ and $\phi_M{}^0 \equiv C_M + k_0 N_M{}^0 l$ are defined as the initial TE and TM phases before deposition.

From that,

$$\frac{\phi_E - \phi_E{}^0}{\phi_M - \phi_M{}^0} \equiv \frac{\Delta\phi_E}{\Delta\phi_M} = \frac{a}{b} \tag{B.4}$$

where the TE phase change $\Delta\phi_E$ and TM phase change $\Delta\phi_M$ can be experimentally measured by the shift of the modal interference fringes.

Tan implemented a numerical method to get that ratio plotted with the average polar angle θ. Let's consider the following structure (**Figure B.1**) which shows the upper layers of the chip where the upper mode travels. The adlayer thickness d_m is now independent of position x since the structure is defined as an elementary length dx for which $d_m(x)$ is constant.

Using a multilayer transfer matrix method it is then possible to get TE and TM mode effective indexes for a range of adlayer thicknesses d_m fixing the adlayer RIs $n_{x,z}$ and n_y (i.e. fixing the polar angle θ because of **Equation 2.6 – Section 2.3.2**). For one polar angle, **Equation B.2** shows that it is possible to get a and b values performing a linear regression of the two sets of data (a and b are respectively the slopes of TE and TM linear regressions). Therefore since it is possible to plot a and b as a function of the polar angle, it is also possible to plot the ratio with the angle because of **Equation B.4**.

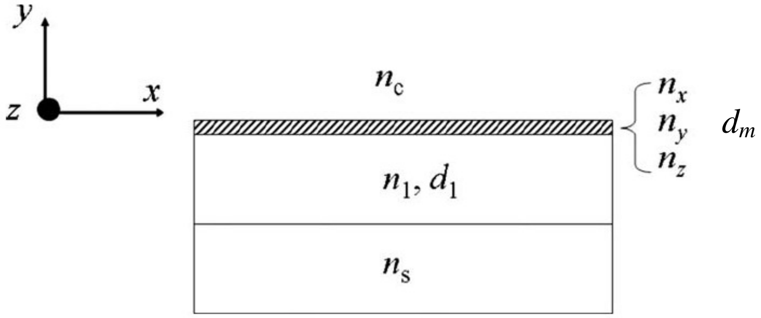

Figure B.1 – Structure defined in order to use the transfer matrix method knowing that n_s, n_1, d_1, and n_c are known, d_m is a variable, and n_x, n_y, and n_z can be calculated for a given polar angle [32].

Appendix C: Asymmetrical beam expander design

After investigating different options (single lens, commercial beam expanders), it has been decided to design a simple asymmetrical beam expander using 2 lenses (convex and concave) in a Galilean configuration (**Figure C.1 left**). By contrast the Keplerian configuration uses 2 concave lenses (**Figure C.1 right**). The main advantages of our configuration are that the space required is reduced, and it is easier to set and maintain the alignment.

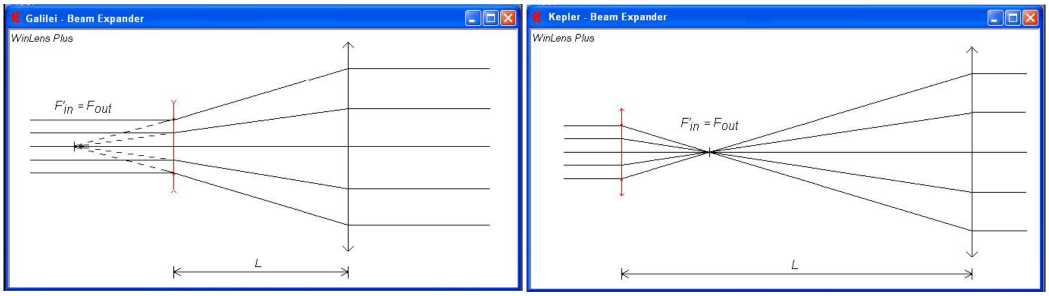

Figure C.1 – Beam expanders in a Galilean configuration (left) and in a Keplerian configuration (right) [46].

We designed the asymmetrical beam expander using the software WinLens3D Basic. The beam expander has been designed so that it could fit in the space available in the AnaLight Quantum in terms of external size of the lenses, and of spacing between the 2 lenses (leaving enough space for mountings). Lenses have been bought from CVI Melles Griot as we found there the best price-quality ratio for our application. The lenses are cylindrical as we want to expand the beam in only one direction.

Figure C.2 shows the final design of the beam expander using the lenses bought from CVI Melles Griot. The smaller lens is plano-concave and rectangular (RCC-12.7-4.8-3.1-C-633-0 [47]), and the bigger one, plano-convex and square (SCX-15.0-20.3-C-633-0 [48]). Both are anti-reflection coated (R < 0.25%) for 633 nm on both faces for an angle of incidence of 0° as we want to avoid reflections within the optical setup (since that increases the static error). They are made with standard grade glass Schott BK7 and they have been chosen with a very good surface quality (20-10 scratch and dig). With that configuration the beam expander ratio in the horizontal direction is 6.67. That means the beam waist is increased from 650 µm to 4.34 mm, and its divergence is decreased from

1.24 mrad to 0.19 mrad. The emerging Gaussian beam has a waist wide enough to illuminate properly the 3 channels of the chip and not too wide at the same time to prevent its tails from being too close to the inner walls of the optical setup. The optimal separation between the 2 lenses is 33 mm (found using the software). This design is now ready to be implemented.

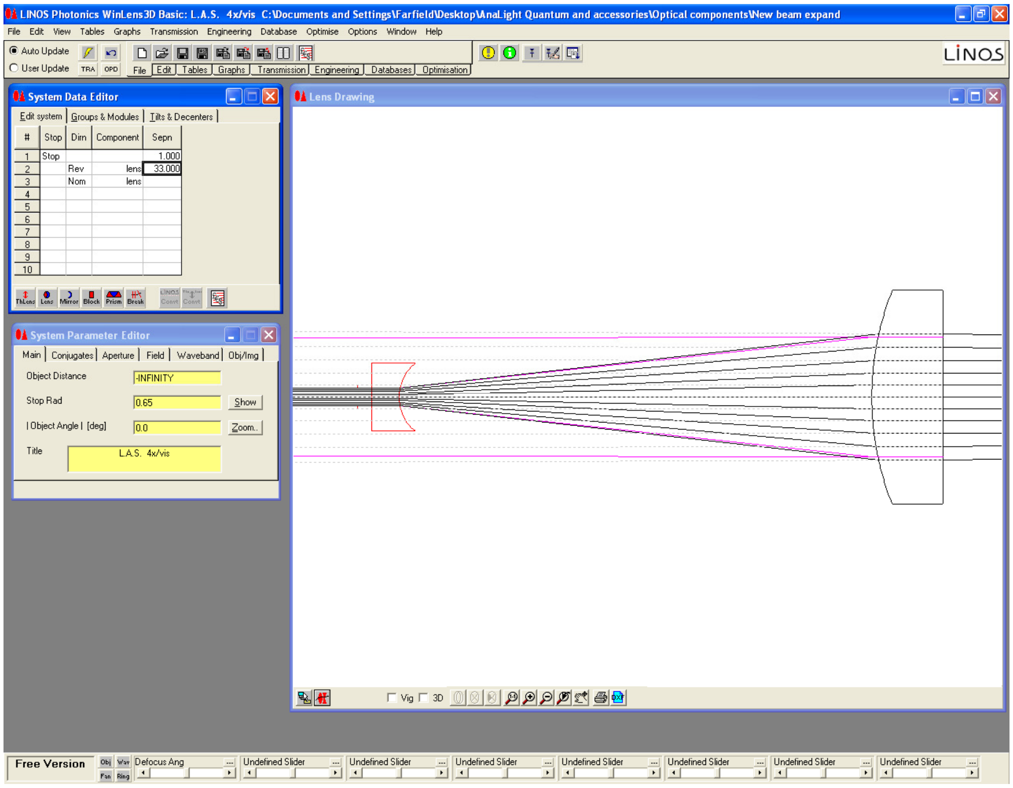

LINOS Photonics WinLens3D Basic: L.A.S. 4x/vis C:\Documents and Settings\Farfield\Desktop\AnaLight Quantum and accessories\Optical components\New beam expand

● Auto Update
○ User Update

System Data Editor

Edit system | Groups & Modules | Tilts & Decenters

#	Stop	Dim	Component	Sepn
1	Stop			1.000
2		Rev	lens	33.000
3		Nom	lens	
4				
5				
6				
7				
8				
9				
10				

System Parameter Editor

Main | Conjugates | Aperture | Field | Waveband | Obj/Img

Object Distance: -INFINITY

Stop Rad: 0.65 Show

| Object Angle | [deg]: 0.0 Zoom..

Title: L.A.S. 4x/vis

Figure C.2 – Screenshot of the asymmetrical beam expander designed with WinLens3D.